

2015 NSF/REU

**RESEARCH EXPERIENCE  
FOR UNDERGRADUATES  
IN PHYSICS**



**STUDENT RESEARCH PAPERS**

VOLUME 26



**UNIVERSITY OF  
NOTRE DAME**  
College of Science

**REU DIRECTOR  
UMESH GARG, PH.D.**

**REU Student Research Papers – Summer 2015**  
**University of Notre Dame – Department of Physics**

<b>Student</b>	<b>Research Title</b>	<b>Page No.</b>
Virginia Bailey Loyola University Chicago	Radiation and Shielding Effectiveness at CASPAR	1
Dillon Bak University of Notre Dame	STM Data Simulation	11
Carlos Buxó-Vázquez Universidad de Puerto Rico & John Charters University of Notre Dame	Working with FPGA Emulation Code for the CMS Upgrade	21
Gabriel Calderón-Ortiz Universidad de Puerto Rico	Cross-Section and Angle Distribution Determination of $^{65}\text{Cu}(\alpha, p)^{68}\text{Zn}$	33
Kimberly Cushman SUNY College at Oneonta	Investigating TwinSol Gas Cell Windows	43
Robert Cameron Dennis Wabash College	Project GRAND: Data Acquisition and Correction Methods	53
Victor Garcia University of Texas at El Paso	Improving the Low-Energy Electron Beam for Electron-Molecular Interaction	63
Alec Hamaker Hanover College	Experimental investigation of RF carpet repelling force	73
Siyu He Xi'an Jiaotong University	Properties of Carbon-Enhanced Metal-Poor Stars: On the Bi-modality of Carbon Abundances	83
Taylor Hoyt University of Texas at Austin	Time-resolved Spectroscopy of J1321: a Mysterious Polar with Strong Absorption Features	93
Daniel Jones Missouri State University	Comparison of Optical Models for 400 MeV alpha scattering with $^{90}\text{Zr}$ and $^{92}\text{Mo}$	102
Changhao Li Xi'an Jiaotong University	Resolution and Stability Analysis of the ATF2 Straightness Monitor	113
Brendan Murphy Arizona State University	Testing the predictive power of statistical model calculations of the (a,g) reaction cross-sections for the $p$ -process	123

Alison Peisker Northern Illinois University	Physics List Comparisons for the Deep Underground Neutrino Experiment	133
Cesar Perez Florida International University	Measuring Magnetic and electrical properties of ferromagnetic semiconductors	143
Shangran Qiu Xi'an Jiaotong University	Statistical Mechanics of Extreme Values in Equilibrium and Non-equilibrium	153
Alissa Runyon Linfield College	Atmospheric Dispersion Corrector for the iLOCATER Spectrograph	163
Jaclyn Schmitt Clemson University	COSY Simulations to Guide Commissioning of the St. George Recoil Mass Separator	173
Rochelle Silverman Virginia Polytechnic Institute	Numerical Simulations of the Electronic Properties of a Penrose Tiling Quasicrystal	183
Yingchao Zhang Xi'an Jiaotong University	Simulate the $^{17}\text{F}(d,n)^{18}\text{Ne}$ reaction by Distorted Wave Born Approximation (DWBA) method	193

# **Radiation and Shielding Effectiveness at CASPAR**

Virginia Bailey

2015 NSF/REU Program  
Physics Department, University of Notre Dame

ADVISOR: Dr. Daniel Robertson

## **Abstract**

The Compact Accelerator System for Performing Astrophysical Research (CASPAR) is an accelerator system designed to perform nuclear fusion reactions in the astrophysically important energy range. The low energies required for these measurements lead to low cross sections of reaction. Therefore, it is advantageous for the system to be placed in a deep underground laboratory to shield the system from cosmic ray background that would easily drown out signals from the reactions of interest. While putting the accelerator deep underground reduces background radiation from cosmic rays, radiation is present in the experimental cavity due to naturally occurring radioactivity in the rock, as well as beam-induced radiation. Beam-induced radiation must be reduced with various methods of shielding in order to protect both personnel and nearby experiments, also requiring a low background environment. Our project looked at the beam-produced radiation and the effectiveness of the shielding techniques proposed based on Geant4 simulations and calculations using basic physics principles. We found that even in the worst-case scenario, radiation levels would be sufficiently blocked by the shielding placed around the accelerator system.

## **Background**

Stellar burning is the source of all elements lighter than iron, except for hydrogen and helium, as well as the source of energy for a star. To better understand the burning processes in stars, nuclear astrophysicists perform nuclear fusion reactions to measure their properties such as the cross section. Reaction cross sections  $\sigma$  depend on properties of the reacting nuclei, such as the energy. Nuclei in a stellar environment can be described by a Maxwell-Boltzmann distribution of energies. The energy of the nuclei must be small

enough that the particles will fuse rather than scatter. However, the energy must also be large enough that the particles can overcome the Coulomb barrier between them due to the charge of the nuclei. Thus it is only for a small range of energies, called the Gamow window, that these nuclear fusion reactions can take place. This Gamow window occurs at relatively low energies, making reactions difficult to reproduce in laboratory settings. Cross sections steeply depend on the energy, causing these low energy reactions to have very low count rates. The signals from these low count reactions are easily blocked by background radiation in the detectors. Instead, reaction cross sections are generally measured at higher energies and the data is extrapolated into the lower energy region. This extrapolation leads to great uncertainty in the astrophysically important energy region. Thus these cross sections must be measured directly for an accurate model of stellar evolution. Reactions in this energy range can only be measured with a significant reduction in background radiation.

## **CASPAR**

The CASPAR experiment is designed to perform reactions in the Gamow energy region with low cross sections. To shield from cosmic rays, the system will be placed 4850 feet underground at the Sanford Underground Research Facility (SURF) in South Dakota. The rock barrier prevents nearly all cosmic radiation from entering the experiment cavern and has a 4300 m.w.e rating. Similar underground experiments such as the LUNA experiment in Gran Sasso, Italy have experienced a thousand-fold reduction in  $\gamma$ -ray background in the energy region above natural radioactivity due to rock shielding alone [1]. However, the system is still subject to natural radiation from radioactive decay in the rock surrounding the system as well as beam-induced radiation. This radiation can be

harmful to humans in the area of the reactions as well as to nearby experiments. Radiation shielding is required to reduce the radiation in the control room and refuge chamber (located to the right and left of the cavity, respectively as seen in figure 1) to an acceptable dose rate for workers and outside the experiment area to below natural background.

### Shielding

Due to beam-induced radiation, the experiment cavern must be shielded from both the control room and exterior walkways to prevent excessive radiation to workers and the public. Also, radiation levels must be reduced to natural background levels to prevent interference with neighboring experiments.

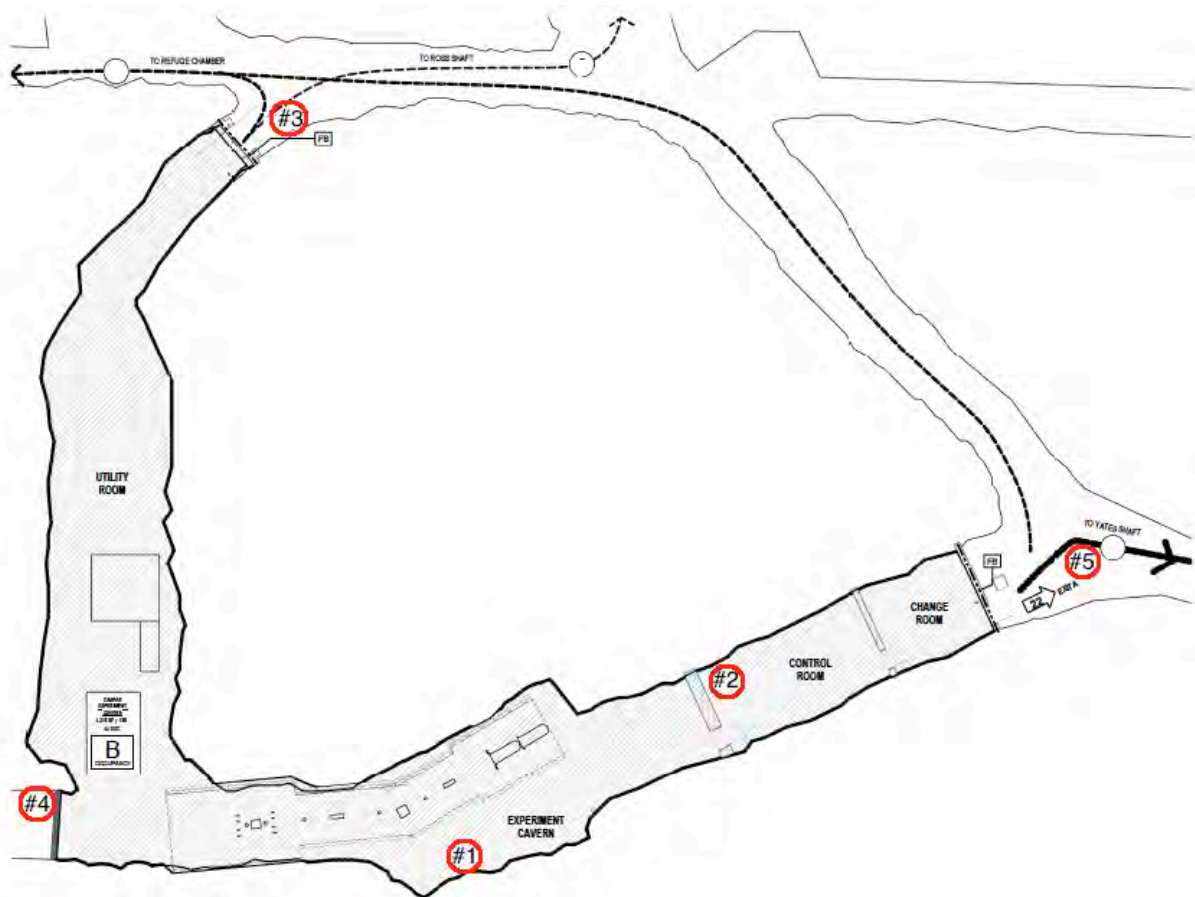


**Figure 1:** Layout of the CASPAR experiment chamber. Each circled number represents a proposed location for a neutron and gamma radiation monitor.

The doors at each monitor are as follows: 2) East Radiation Wall, 3) North Radiation Wall, 4) Steel Door.

The experiment cavern is shielded by two concrete radiation walls at the north and east ends of the cavern. Both walls include a door made of lead and 5% borated polyethylene (Borotron) as well as a serpentine maze for utilities and signal cables to pass through the wall.

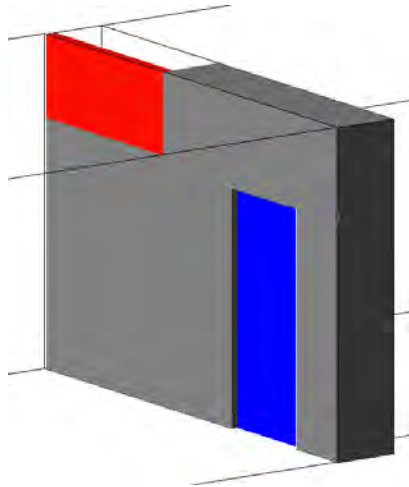


**Figure 2:** Simulation of East radiation wall in Geant4 software. The grey wall is made of concrete, blue is the lead/borotron door, and red is the maze for cords.

The north end of the cavern is further protected due to the 90° turn in the cavern that leads to a significant reduction in radiation. A steel door shields the refuge chamber to the west of the experiment cavern.

## Simulations

A series of simulations were run using Geant4 software to simulate the effects of  $1\text{E}+9$  gamma rays and  $1\text{E}+8$  neutrons produced by the beam at various energies. These simulations were run with gamma rays of 1 MeV and 2.5 MeV energy and neutrons with 5.2 MeV and 2.5 MeV energy being produced at the position of the analyzing magnet in the beam line. Nominally, the main radiation sources are likely to be the accelerator itself, the target station, and interactions along the beamline with auxiliary equipment. Therefore the source of radiation for the simulation was placed at the midpoint along the beam line, at the analyzing magnet. This position, being both close to and in a straight line of sight from the reference detector allowed for the most accurate radiation count.

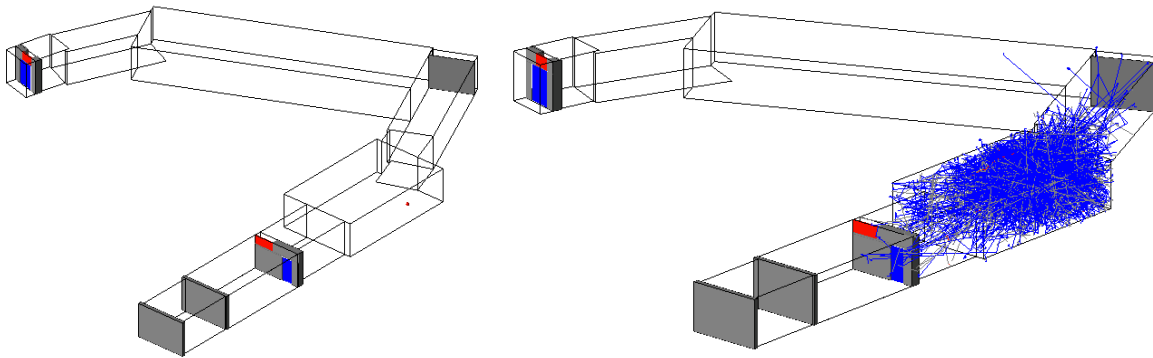


**Figure 3:** Left: Layout of experiment chamber in Geant4 simulation. Right: Simulation of 1000 neutrons created at analyzing magnet including secondaries produced by neutrons reacting in the walls.

The simulations recorded both neutron and gamma levels and their energies, before and after each of the radiation shielding doors, at the reference detector inside the experiment chamber and at a point in the corridor outside of the experiment area. A similar study using the Geant4 software proved the simulations accurate when tested against a MCNP simulation [2].

## Calculations

Using the detector inside the chamber as a reference point, calculations were performed to determine both the abundance of neutrons and gamma rays at each of the doors per second and the radiation dosage to an average human. These calculations were performed only using the distance from the radiation source to the doors, and did not take into account any shielding or other effects that the geometry of the cavern caused. These results were then compared with the simulation values at each door to determine the effectiveness of the shielding as well as to confirm the accuracy of the simulations. First, the radiation dose was calculated at the reference detector based on the simulation results for neutron and gamma count and mean energy at the detector using **Eqtn 1**.

**Eqtn 1:**

$$1 \text{ rad} = \frac{100 \text{ ergs absorbed energy}}{1 \text{ gm of absorber}}$$

The calculation was based on the assumption of a person with a surface area of 1 m<sup>2</sup> and mass of 49.25 kg. This is smaller than the average human, but the dose rates can easily be scaled to reflect a more realistic person. The worst-case scenario was assumed, where the person absorbed the entire radiation flux presented. This radiation dose at the reference detector was then used to calculate the doses at the two radiation walls, the steel door, and a detector in the corridor to the east of the change room using **Eqtn 2**.

**Eqtn 2:**

$$I_2 = I_1 \left( \frac{d_1^2}{d_2^2} \right)$$

$I_1$  represents the radiation intensity at the reference detector in mR/hr,  $I_2$  is the radiation intensity at the wall or detector of interest, and  $d_1$  and  $d_2$  are the distances of the reference detector and detector of interest from the radiation source, respectively. The radiation

dose was assumed to be per second, corresponding to  $1 \times 10^8$  neutrons and  $1 \times 10^9$  gamma rays being produced per second. This is again a worst-case scenario, as actual radiation production is anticipated to be several orders of magnitude less than this.

Dose rates were also calculated using the neutron and gamma counts before and after each door with the same assumptions for the person. These results were then compared to the calculated values at the doors. These results are shown in **Table 1**.

5.2 MeV Neutron					
Door	Dose Rate (millirem/hr)			Percent of Calculated Presented to Door	Percent of Calculated through Door
	Calculated	Simulation	Simulation		
		Ingress	Egress		
Reference Detector	19.78	19.78	N/A	100.00%	N/A
East RW	3.49	3.79	0.52	108.82%	14.83%
North RW	0.38	8.87E-05	9.18E-06	0.02%	0.00%
Steel Door	2.83	4.26	3.83	150.43%	135.02%
Corridor Detector	0.66	N/A	N/A	N/A	N/A

**Table 1a.** Dose rates from  $1 \times 10^8$  5.2 MeV neutrons being produced at the analyzing magnet from calculation and simulated values before and after each door.

1 MeV Gamma					
Door	Dose Rate (millirem/hr)			Percent of Calculated Presented to Door	Percent of Calculated through Door
	Calculated	Simulation	Simulation		
		Ingress	Egress		
Reference Detector	1.30	1.30	N/A	100.00%	N/A
East RW	0.23	0.39	0.04	168.10%	19.13%
North RW	0.03	1.52E-06	7.91E-08	0.01%	0.00%
Steel Door	0.19	0.36	0.30	193.38%	159.53%
Corridor Detector	0.04	N/A	N/A	N/A	N/A

**Table 1b.** Dose rates from  $1 \times 10^9$  1 MeV gamma rays being produced at the analyzing magnet from calculation and simulated values before and after each door.

The calculated dose for the reference detector is taken straight from the amount of radiation that reached that detector in the simulation. Therefore the two numbers are equal and 100% of the calculated value was presented to the door in the simulation. The East radiation wall has a direct line of sight to the analyzing magnet where the radiation is produced causing the calculated and simulation based values for the gamma rays presented at the door to be similar. The simulated value is slightly higher than the calculated value because the calculations did not take into account any scattering of radiation from the walls or secondary products of the radiation produced interacting with the walls. However, even with these higher amounts of radiation presented to the door, the wall successfully blocks most of the radiation from passing through. Similarly, the simulated radiation at the steel doors is higher than the calculated value. However, this door does not attenuate the radiation as well as the East radiation wall, causing the radiation past the door to be greater than the calculated value. The radiation presented to the North radiation wall in the simulation was several orders of magnitude lower than the calculated values. This is due to the sharp turn in the cavity between the accelerator system and the door. Simulations did not count the radiation levels at the corridor detector, but as it is past the East radiation door the dose rate is likely smaller than the calculated value.

## **Conclusion**

The NRC regulates that the public be exposed to a maximum of 2 millirem per hour of radiation [3]. Even in the worst-case scenario and without taking into account shielding

or other cavern geometry, the radiation levels expected at various points surrounding the CASPAR experiment will be less than this maximum dose. Only inside the experiment room, where no personnel will be during the running of experiments, would this limit be reached. Actual radiation levels will likely be many orders of magnitude less as the amount of radiation produced is likely to be much smaller than assumed for these calculations.

## References

- [1] H. Costantini, A. Formicola, G. Imbriani, M. Junker, C. Rolfs, F. Strieder  
Reports on Progress in Physics, 72 (8) (2009), p. 086301
- [2] A. Best, M. Couder, M. Famiano, A. Lemut, M. Wiescher  
Nuclear Instruments and Methods in Physics Research Section A , 727 (2013)
- [3] <http://www.nrc.gov/reading-rm/doc-collections/cfr/part020/part020-1301.html>

# STM Data Simulations

Dillon Bak  
2015 REU Program  
Physics Department, University of Notre Dame  
Gomes Laboratory

Advisor: Prof. Kenjiro Gomes

## **Abstract**

A Scanning Tunneling Microscope (STM) is often used to explore and image the electronic structures and topographies of nearly two-dimensional surfaces. The STM has been used to explore the electronic structure of many crystalline surfaces, and such research is done quite regularly. Meanwhile, there exist materials called quasicrystals that exhibit properties somewhere between crystals, materials that exhibit translational symmetry, and glasses, which are unordered. The types of symmetry and order exhibited by quasicrystals are shared by Penrose tilings. As such, a Penrose tiling provides an interesting structure for study using the STM. Before such a study is conducted however, it is ideal to have an estimation of the results. This allows for any departures from theory to be easily recognized and a benchmark so that a problems during data collection can be identified. As such, simulations of the STM data were made that encompass the expected results given a tight binding model and a scattering model.

## **Introduction**

Atomic manipulation has its origins in the research of IBM in the 1980s. In 1981, Gerd Binnig and Heinrich Rohrer invented the scanning tunneling microscope (STM), an achievement for which they would win the 1986 Noble Prize in Physics. The STM was later used in 1990 by Donald Eigler and Erhard Schweizer to spell out "IBM" by placing xenon atoms on a nickel substrate. This was the first demonstration of atomic manipulation and thus the roots of this project.

The name scanning tunneling microscope suggests quite a lot about its functioning. Nevertheless, a proper overview of the STM would be beneficial.

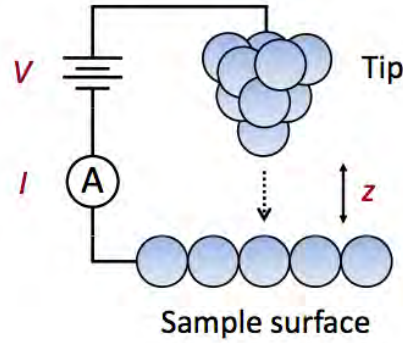


Figure 1 A simplified diagram of the STM.

STMs image surfaces at an atomic level. As such the essential component of the STM is a metallic tip that ideally comes to a point comprised of a single atom. The fine movements of this tip in all three spatial dimensions can then be controlled by piezoelectrics. This movement is the reason for which the microscope is described as scanning. In order for the STM to make measurements a current must be established between the tip and the surface. Tunneling provides the mechanism that allows for the creation of this current and differentiates the STM from other non-optical microscopes. First, a bias voltage is applied between the sample and the tip. Then due to this bias voltage, there is a non-zero probability that electrons from the tip tunnel to the surface through the space that separates the two. The current is defined by the following equation:

$$I = \frac{4\pi e}{\hbar} e^{-2z\sqrt{2m\gamma}/\hbar} \int_{-\infty}^{\infty} \rho_{sample}(\varepsilon + V) \rho_{tip}(\varepsilon) (f(\varepsilon + V) - f(\varepsilon)) d\varepsilon,$$

where  $I$  is the tunneling current,  $\rho$  is the density of states,  $V$  is the bias voltage,  $z$  is the distance between the tip and the sample, and  $\varepsilon$  is the electron energy. There is quite a lot going on in this equation. However, focusing on two terms can provide important information about the tunneling current. First, the exponential term

shows the current's dependence of the spacing between the tip and the sample.

Secondly, the  $\rho_{sample}$  term as one would expect shows that the current depends on the sample's density of states. This means that changes in the electronic structure of the sample will be measured by the STM.

With this in mind, a general description of the STM's operation can be given. The system as described is usually kept surrounded by a cryostat. The cryostat is then filled with a cooling agent. Usually liquid nitrogen, which can cool the system to 77K, or liquid helium, which can cool the system to 4K, is used. These temperatures allow for sufficient noise reduction while conducting experiments. To this end, our lab also uses a vibration isolation table to further reduce noise. The tip is then lowered in small increments until a tunneling current is established. The tip then begins to scan over a small portion of the sample. While it scans the tip's height will be adjusted using the piezoelectric so as to maintain a constant current. A feedback loop is used to monitor the current and decide if tip movement is necessary. Thus, if there are irregularities in the physical structure or the density of states of the surface changes the tip will adjust to reflect these changes. These changes in current and tip height are used as data that is then used in imaging.

### **Atomic Manipulation**

The STM also has another use that is key to our group's work. Atomic manipulation allows for the rearrangement of particular atoms or molecules on a substrate. Normally the tip of the STM is positioned such that it cannot disturb the surface being observed. However, the tip can be brought closer so that it has the

ability to move single atoms or molecules that are resting on the surface. The exact process is as follows. First, the tip is positioned over the atom or molecule, which you wish to reposition. Then the tip is lowered, typically somewhere between 3-4Å, so that the tip is now low enough to interact with atoms on the surface. The tip is then moved laterally to the location to which you want to move the atom or molecule, and the object being manipulated should follow the tip. The movement itself is caused by van der Waal forces acting on the atom as the tip moves away from it. When the desired location is reached, the tip is raised to its original position, and the process may be repeated.

### STM Imaging

Having overviewed the operation of the STM, we can now discuss some of the ways in which the data from the STM might be used.

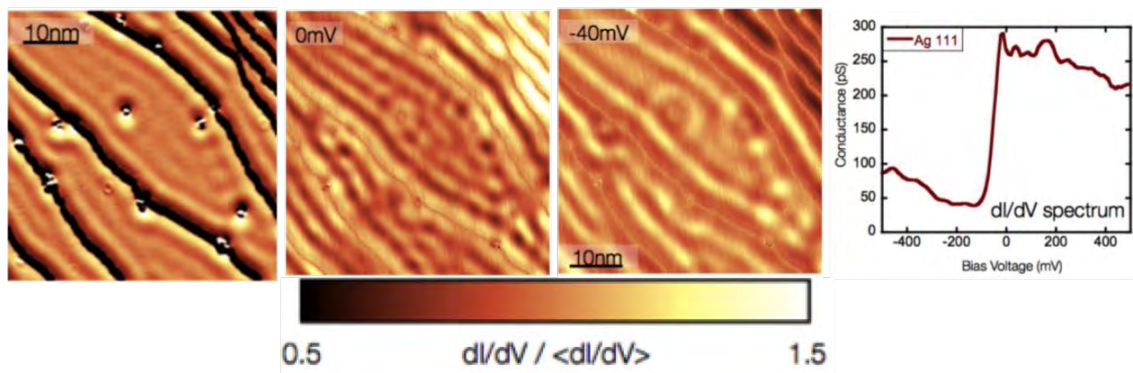


Figure 2 From left to right: A topography, a conduction map at 0mV, a conduction map at -40mV, and a spectrum

Figure 2 above shows three different types of graphical representations of STM data. The first topographies, attempt to give a physical picture of the surface. In the figure

the ridges show where there are changes in the height of the surface. In between the ridges, one also sees wave patterns. These represent changes in the density of states. The second type of image is a conduction map. These show  $\frac{dI}{dV}$  as a function of position in the x-y plane while the biased voltage is kept constant. As such, conduction maps can change in appearance depending on the bias voltage used. This can be seen in the figure. The third type of image is a spectrum. These images show changes in  $\frac{dI}{dV}$  over a range of bias voltages for a single point on the surface.

### Dual Lattice

It has been mentioned that the group aims to eventually use the STM to analyze a Penrose pattern, and that this will be accomplished through atomic manipulation. Yet, there are some details concerning how this will be accomplished that have not yet been discussed.

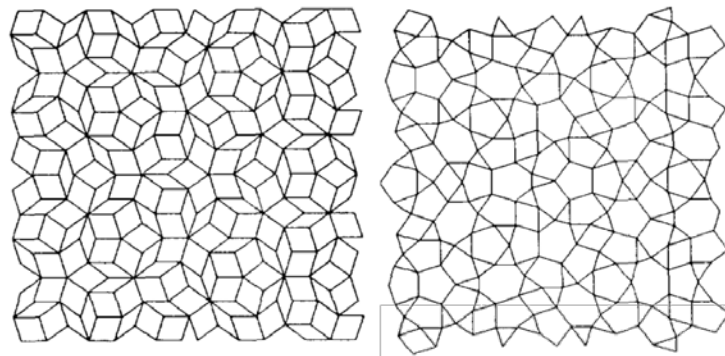


Figure 3 On the left a Penrose tiling and on the right its dual lattice

Figure 3 shows two images, a Penrose tiling and its dual lattice. The dual lattice gives the center points for the tiles of the Penrose. In the dual lattice above, each intersection gives the location of one of these points. The dual lattice is important to

the eventual experiment and to the simulations these centers are used to form our desired pattern. When this experiment is conducted the STM will be used to position CO molecules on a copper surface at the coordinates indicated by the dual lattice of a Penrose tiling. This may seem initially strange, but such an arrangement places an insulator at a certain point and then leaves the surrounding area as a conductor. As such, we have the Penrose tiling in the form of a conducting surface.

### **The Simulation**

So far, most the details covered have examined the working of the STM and what it can produce. However, before the STM is used it is prudent to make simulations. The results of a simulation will provide a prediction of the physical results from the STM. To this end, MATLAB was used to create scattering simulations of a Penrose pattern. The method used supposes that electrons are scattering over arbitrary points on the surface. Schrodinger's equation is then solved using Green's functions. Using the imaginary component of the Green's functions for the system the Local Density of States (LDOS) can be found. More information on this process can be found in chapter 4 of Chris Moon's thesis, "Designing Electron Wave Functions in Assembled Nanostructures."

Figure 4 shows the results of running the scattering simulation under parameters typical of the STM environment. In the conductance map we see examples of fivefold symmetry as well as aperiodicity that are typical of Penrose tilings and certain quasicrystals. The spectrum has a peak that is very close to

being centered at 0 eV. This alone would be insignificant, but it is important when comparing the scattering model to the tight binding simulation.

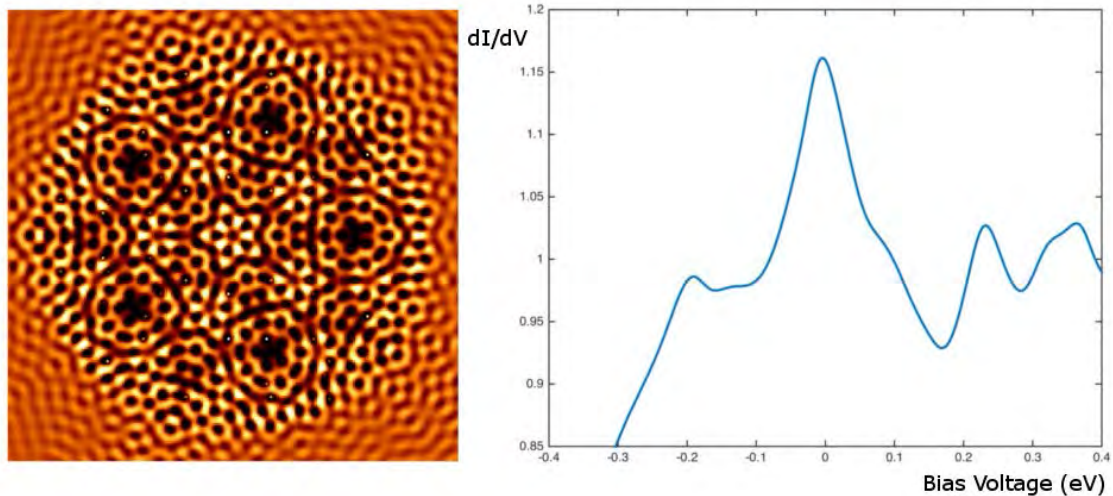


**Figure 4** The results of the scattering simulation under usual operating conditions and a lattice parameter of 16.

The results of the tight binding simulation are shown in Figure 5. The spectrum is of particular interest. Due to the manner in which tight binding calculations are carried out, the peak with the highest density of states is centered at 0 eV. If we want to compare the scattering simulation with the tight binding simulation a correlation must be found between them. One way to begin making this correlation is to find a parameter set that centers the maximum peak of the scattering spectrum at 0 eV as well. To do this a lattice parameter, which defines atomic spacing in the lattice, has been adjusted. In the images for Figure 4 a lattice parameter of 16 was used corresponding to an atomic spacing of 16Å. This value seems to be close to being correct. However, small changes to the lattice parameter can have unexpected effects on the spectrum curve.

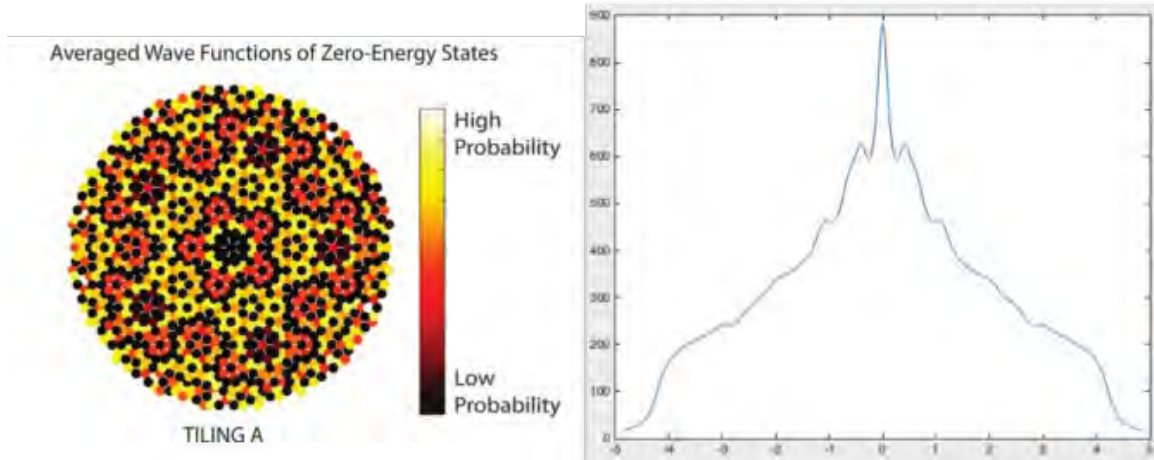


Figure 5 The results of a separate tight binding simulation to which the scattering simulation must be correlated.

## Conclusion

The simulations seem to be running correctly. However, work still needs to be done to properly define the lattice parameter in the scattering simulation. Once this is done we will have a reliable comparison for future data. Additionally, the group should be able to start atomic manipulation shortly. After which, we will be able to run the experiment.

## References

- Chen, C. Julian. *Introduction to Scanning Tunneling Microscopy*. Oxford: Oxford Press, 2008. Print.
- Moon, Chris. "Designing Electron Wave Functions in Assembled Nanostructures". Stanford University, 2009. Electronic.
- Steinhardt, Paul. "What are Quasicrystals?". Lecture Slides.



# **Working with Field-Programmable Gate Array Emulation Code for the Compact Muon Solenoid Upgrade**

Carlos J. Buxó-Vázquez

John Charters

2015 NSF/REU Program

Physics Department, University of Notre Dame

Advisors:

Professor Kevin Lannon

Professor Michael Hildreth

31 July 2015

## **Abstract**

Within the next decade, the Large Hadron Collider (LHC) will be upgraded to the High Luminosity LHC (HL-LHC). The upgrades will increase the number of particles in the accelerator in order to produce more collisions. The Compact Muon Solenoid (CMS) will require an enhanced trigger system to manage all of these interactions and determine which events to save. Primarily, we are trying to apply the tracking detector algorithms with the Level 1 Trigger. Our project relied on event simulations using an FPGA Emulation code developed by a team of physicists. The first part of this research involved evaluating the effectiveness of the algorithm to correctly identify particle tracks, provided samples with or without pileup. For the second section of this research, by comparing the track parameters and stubs of the tracks in different seeding layers we obtained insight into how the algorithm generates the tracks. Then, by converting the track parameters into their floating value equivalent and comparing them to the generated values in the code, we developed an insight of the duplicate selection process.

## **The LHC and HL-LHC**

The Large Hadron Collider (LHC) is a particle accelerator located at the European Organization for Nuclear Research (CERN). With a 27 kilometer circumference, the LHC is the largest and most powerful accelerator in the world. The collider consists of two particle beams travelling in opposite directions at nearly the speed of light, guided by superconducting electromagnets [1]. As of April 2015, the beams collide at unprecedented energies of 13 TeV. The High Luminosity LHC is an ongoing project aimed at increasing the luminosity, a measure of the number of particles per unit area per unit time, to 10 times its current value. The upgrades will improve the accuracy of the accelerator and allow for the detection of rare collisions [2]. The HL-LHC is estimated to be installed around 2025. It will likely lead to physics discoveries beyond the Standard Model.

## **CMS Upgrades**

The Compact Muon Solenoid (CMS) is a detector at the LHC that observes a range of particles in order to help answer the most fundamental questions in physics. Among other components, it consists of both electromagnetic and hadron calorimeters, a superconducting solenoid, and a tracker placed in a series of muon chambers to detect muons [3]; our results use  $\mu^-$  samples. In order to accommodate for the HL-LHC upgrade, CMS will upgrade its trigger systems. We are focused on the Level 1 Trigger, which is employed in dedicated hardware and currently receives information from the calorimeter and muon triggers. The purpose of a trigger is to determine which collisions are the most interesting to analyze (out of around a billion proton collisions per second) and to store only those events (around 100 per second), thus significantly reducing the data processed. Due to higher luminosity and more overlapping collisions, L1 Trigger rates will increase from 100 kHz to 750 kHz. The overarching project is to instrument the tracking

detector with the L1 Trigger, which will be crucial in handling the larger amounts of data. We are in the design and prototyping stage, estimated to end around 2018.

## FPGA Emulation Code

The tracklet project is part of a collaboration between five universities, including Notre Dame. The code that the project shares emulates a field-programmable gate array (FPGA) that will be implemented in the CMS upgrades. FPGA circuits used in the trigger will analyze one event's worth of data in approximately one microsecond. Using a track trigger algorithm, the emulator constructs tracks based on event data from an input text file. The first step in the algorithm is to find pairs of hits in each layer of the detector, known as stubs. The trigger only cares about stubs indicating high-momentum tracks. The second step is to find a tracklet, or a pair of stubs, in two adjacent layers, called seeding layers. Given this tracklet, the final step is to extrapolate the particle's entire path. The L1 Trigger uses a linearized chi-squared fit to compare the path with nearby, consistent stubs. It determines four parameters: transverse momentum  $p_T$ , initial azimuthal angle  $\phi$ , pseudorapidity  $\eta$ , and initial coordinate  $z_0$ . Pseudorapidity is related to polar angle  $\theta$  by:

$$\eta \equiv -\ln \left[ \tan \left( \frac{\theta}{2} \right) \right]$$

In order to measure the algorithm's performance, we created resolution plots, which essentially compare the constructed track parameters with their actual values. We ran the code four times, varying the seeding layer used for track reconstruction. Below are the normalized distributions:

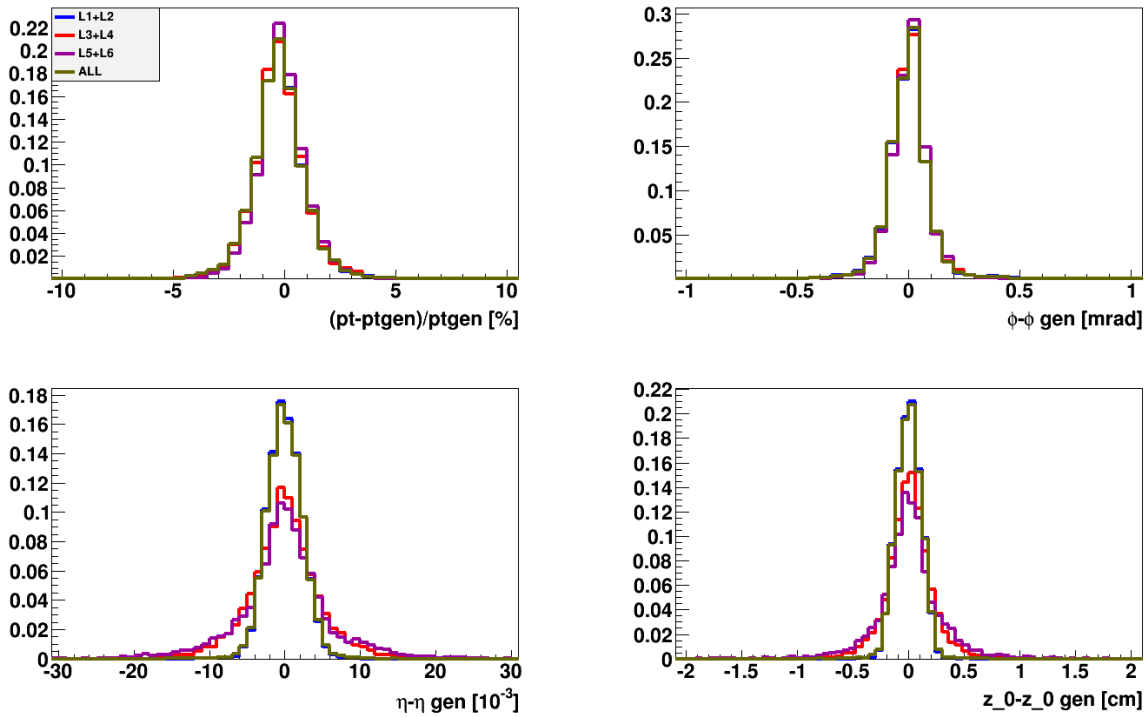


Figure 1: Resolutions by Seeding Layer

The performances of the first and second layers and all layers seeded almost completely match. Notice that the resolution for the outer layers is worse for  $\eta$  and  $z_0$ . Initial attempts to improve these resolutions have been unsuccessful. Interestingly, the root mean square (RMS) for the fifth and sixth seeding layers is slightly smaller than that of all layers for  $p_T$  and  $\phi$ , signifying better results. It is also still unclear as to whether the resolution should depend on seeding layer at all. These questions are still being investigated. Next we plotted corresponding efficiencies for all parameters. We set the restrictions  $|p_T| > 10.0$  and  $|\eta| < 1.0$ . Below are two example plots.

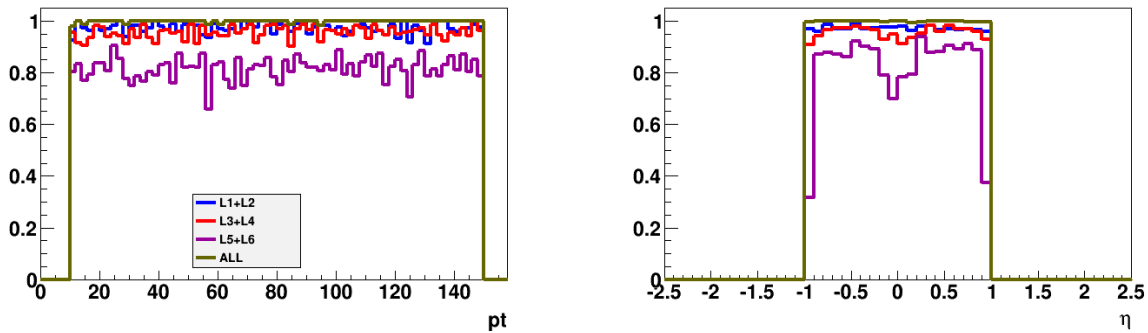


Figure 2: Efficiencies by Seeding Layer

The fifth and sixth layers have worse efficiencies than the other layers do. In general, we observed that the efficiencies are independent of parameter value, besides the fifth and sixth layer dip as  $\eta$  approaches 0. Overall the resolutions and efficiencies display great performance for the emulation code.

### Comparison with Pileup Samples

Our previous studies used text files that represented single muon samples without pileup. Pileup is a term used to indicate that multiple interactions are taking place per event in the same beam collision. Given the expected increase in collisions at higher luminosities, a more realistic sample includes pileup, where for each event the tracker finds thousands of stubs with hundreds of corresponding tracks. The tracking algorithm has more difficulty matching stubs with tracks, and consequently pileup events are harder to analyze. In order to evaluate the tracker's precision with pileup samples, we compared the resolutions with no pileup samples. We turned all seeding layers on for these plots:

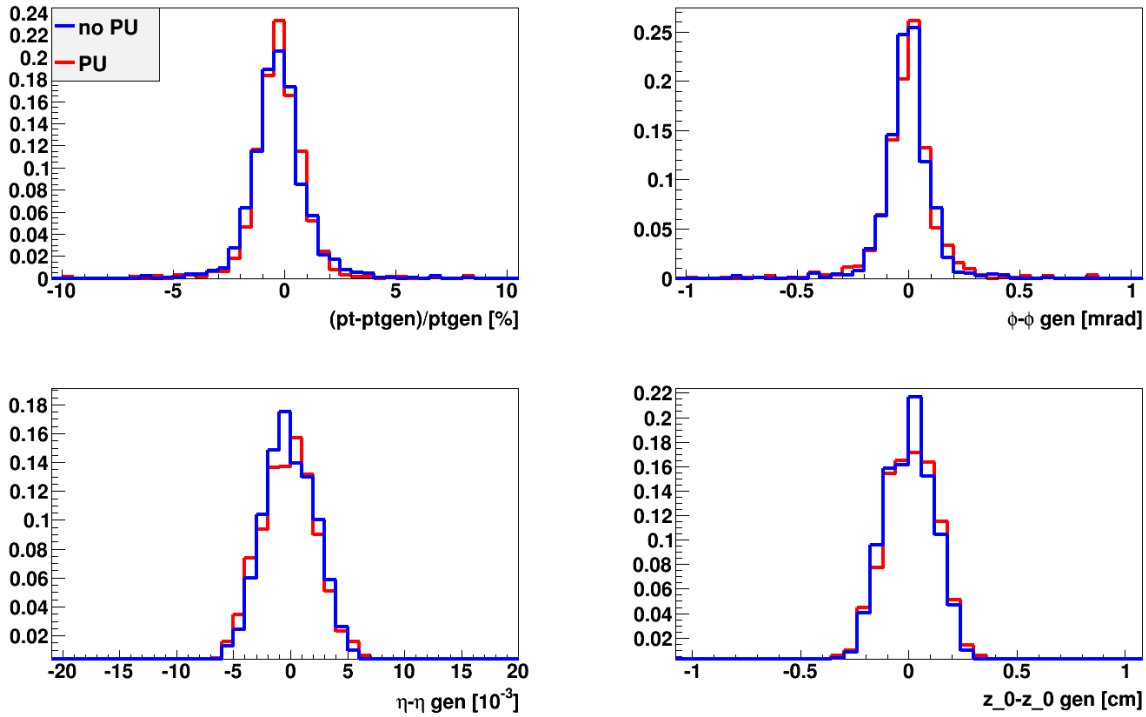


Figure 3: Resolutions for Pileup and No Pileup

The means and RMS's are nearly identical for each parameter, which tells us that the algorithm works equally well for pileup. Additionally, we compared the efficiencies, with the restrictions  $10.0 < |p_T| < 100.0$  and  $|\eta| < 1.0$ . Below are the plots for  $p_T$  and  $\eta$ .

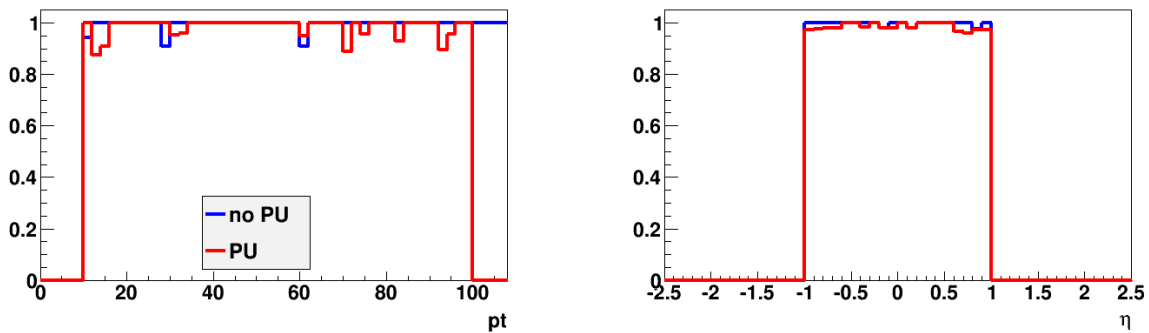


Figure 4: Efficiencies for Pileup and No Pileup

Since more tracks are found with pileup samples, we expected that the pileup efficiencies might actually be greater. In theory, if all possible tracks are found, the algorithm will yield one

hundred percent efficiency, but this includes fake rates in which every false track is constructed. Here the pileup efficiencies are slightly worse, but this is not statistically significant.

### **Track Parameter and Stub Map Study**

The track parameter and stub id study was carried out to create an insight on how the emulation code is generating the emulation tracks for different seeding layer options and how the duplicate selection algorithm for tracks works. This part of the study was done using versions of the code accessed on June 3 and July 20 given that the emulation code was updated between these two dates. The study is focused on the barrel geometry of the CMS detector thus a transverse and eta range of was chosen to cover this region  $|p_T| > 10.0$  and  $|\eta| < 1.0$ . The disk geometry got excluded from this study just to give enough time to see that the barrel geometry emulation was working properly. The study can be carried out easily to this geometry nonetheless.

While studying how the emulation code generates the tracks, the tracks that didn't contain 6 stubs were filtered out since it is unreliable when comparing their stubs to determine if they are indeed the same stubs or not. Tracks from the different seeding layers; L1L2, L3L4 and L5L6 were that met these requirement were chosen for the study. To determine if two tracks are different, the stubs that form the track are compared by verifying the layer they come from and their stub id. If the tracks do not contain the same stubs, they are considered different, otherwise if the tracks do contain the same stubs, the integer value track parameters;  $ir_{inv}$ ,  $iphi0$ ,  $it$  and  $iz0$  are compared between the two tracks. If only one these parameters is different between the two tracks, they are considered different.

We expected that while comparing the tracks for different seeding layers, we would obtain a high number of tracks with the same track parameters and stubs and also a high number of tracks with different parameters and stubs, for both versions of the codes. This turns out not to be the

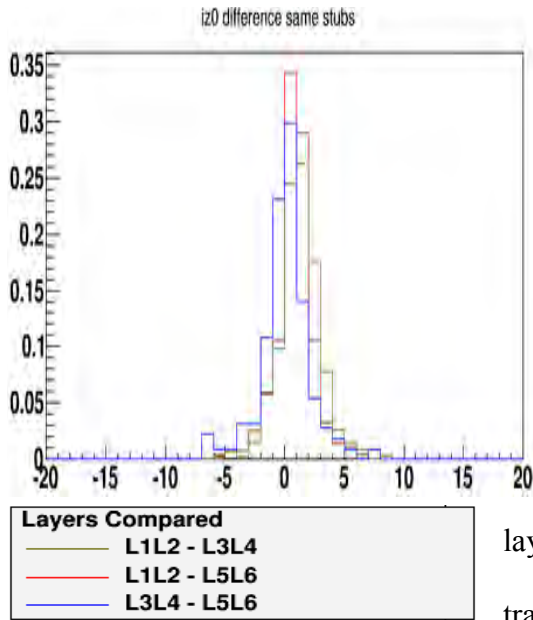


Figure 5: Track parameter  $iz_0$  difference for tracks in different layers

case since for both versions of the code, the amount of tracks that contained the same track parameters and stubs is negligible and that most of the tracks classify as tracks with different parameters and same stubs, and also tracks with different parameters and stubs. This information was verified by plotting the difference of integer valued track parameters for tracks in different layers, and classifying them as tracks with same stubs and tracks with different stubs. As seen in Figure 5 for the version of the code accessed in June 3, if the number of

tracks with same track parameters and stubs were to be higher, we would be observing peaks in the bin containing 0 of the histograms for tracks with the same stub. Nonetheless, we observe something similar to a Gaussian shape, meaning that the track parameters are not equal between tracks in different seeding layers if they contain the same stubs.

For the version of the code accessed on July 20, the difference plots for  $z_0$  and it showed a similar result to the ones obtained from the previous version of the code, but for the  $irinv$  and  $iphi_0$  difference plots, these did not show the same behavior as their counterparts from the previous code, as seen in Figure 6. From these results we can conclude that for the old code, the process of track generation for the different layers is a process independent of the stubs that the track contain. For the new code it can be said that for  $iz_0$  and its values, the process is the same as the previous version of the code, although the behavior of the  $irinv$  and  $iphi_0$  values could be due to a bug in the emulation code. This is also backed up with the information obtained from the efficiency stub done with the new code.

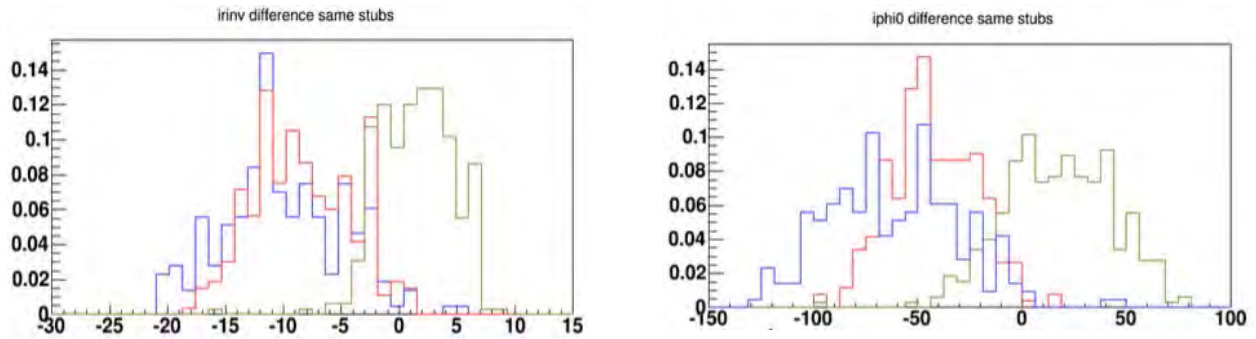


Figure 6: Track parameters irinv and iphi0 difference July 20

## Duplicate Selection Algorithm Study

When running the emulation, the algorithm reconstructs tracks from the available stubs and generated values. The reconstruction algorithm recreates the tracks that are most likely to contain a set of stubs. There is a possibility that the algorithm reconstructs the same track when using different seeding layers, thus recreating the track with a subset of the available stubs. When more than one track is recreated from the same set of stubs, the duplicate selection algorithm must choose one of the tracks as non-duplicate and delete the rest of the tracks marked as duplicates. To create the insight on how the algorithm for track duplicate selection was working, the integer valued track parameters were converted into their floating point equivalent using the conversion factors in the code. The irinv was mapped into the transverse momentum of the track, iphi0 was mapped to phi0, it was mapped to eta, and iz0 was mapped to z0. These values were then compared to the generated values that the emulation code creates for the emulation. The tracks were classified as duplicate and non-duplicate for this part of the study. What we found by comparing the track parameters with the generated values is that the parameters for the non-duplicate tracks agreed more with the generated value compared to the duplicate track parameters, but not by much as seen in Figure 7. Looking on the emulation code, it seems that the duplicate selection process depends on the amount of stub ids the track has on its stub map. A track is not considered to be

duplicate if it contains the most stub ids compared to the other tracks. If all the tracks contain the same amount of stub ids, then the duplicate selection chooses the first track available making this a random process.

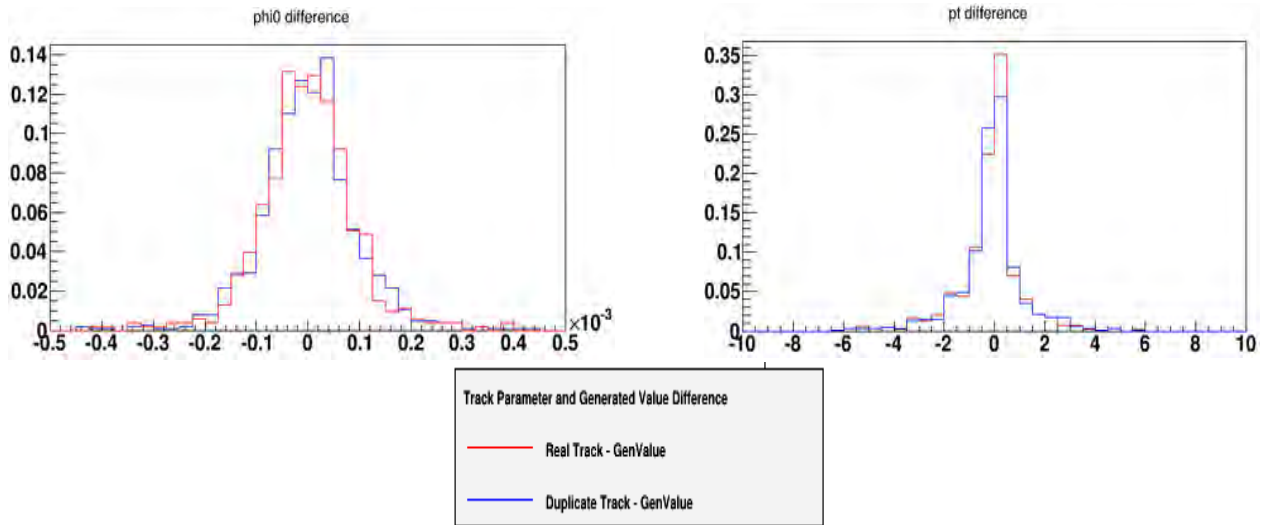


Figure 7: Track parameter difference with generated values for code version June 3

## Conclusion and Further Work

The main studies on the algorithm’s performance have shown that the FPGA Emulation code can successfully construct the path of a particle over the course of thousands of events. While there is some dependence on the layers used to seed, the results are overall favorable. Outer layer seeds tend to be less efficient and precise as one varies  $\eta$  and  $z_0$ . We attempted to resolve the issue by making small changes to the code; this task proved futile, but it helped the code writers better understand alternative methods we could try in the future. We might also return to more in-depth pileup studies for further comparisons. The track generation for different seeding layers for the emulation is a process that’s independent of the stubs contained in the track meaning that the emulation code is working correctly when creating events for the emulation. Although the study was carried out only for the barrel geometry of the CMS, the study can be implemented to the disk geometry without difficulty for future studies. It would be also helpful to understand why the irinv

and iphi0 plots show the behavior obtained for the new code, and if this is indeed a bug in the emulation code, to fix it. The studies done with the duplicate selection algorithm with the old code show good results, although the agreement of generated values with the non-duplicate values is better than the duplicate values not by much. From this particular study it can be concluded that knowing the original seeding layer for the non-duplicate track is an important piece of information which can be used to determine which seeding layers are more efficient for the emulation. This study was done with the new code but due to the results obtained from the irinv and iphi0 plots, it should be redone once the source of the problem has been found.

### **Acknowledgments**

We would like to give thanks to our advisors, Professor Lannon and Professor Hildreth, for providing us with this research experience and the knowledge we have received from them. We would also like to thank the CMS group whom we have been working with and been updating them with our current work for providing us with questions and ideas to keep doing our research. Finally we would like to thank Professor Garg for letting us be part of the Notre Dame 2015 Physics REU and for taking care of all the students from the REU.

### **References**

- [1] “The Large Hadron Collider.” *CERN*, n.d. Web. 28 July 2015.
- [2] “The High Luminosity Large Hadron Collider.” *CERN*, n.d. Web. 28 July 2015.
- [3] “Detector Overview.” *CMS*, 23 Nov. 2011. Web. 28 July 2015.

# **Cross-Section and Angular Distribution**

## **Determination of $^{65}\text{Cu}(\alpha, p)^{68}\text{Zn}$**

Gabriel Calderón-Ortiz

2015 NSF/REU Program  
Physics Department, University of Notre Dame

Advisors: J. deBoer, E. Stech

## **Abstract:**

The formation of elements in stars has been studied for many years and is well known for many nuclei. Nonetheless there are proton rich nuclei whose origins remain not well understood. To this end, in this work we measure the total cross section and angle distribution for the  $^{65}\text{Cu}(\alpha, p)^{68}\text{Zn}$  reaction. We used the FN Tandem Van de Graaff accelerator at the University of Notre Dame to generate an alpha beam with energies between 7.5 to 11.0 MeV. A self-supported copper target with thickness  $632 \mu\text{g}/\text{cm}^2$  was placed at the center of the chamber under a vacuum of better than  $2.9 \mu\text{Torr}$ . Silicon Photodiode Detectors were used to detect the protons scattered from the reaction at 13 different angles, with two detectors at the same angle to monitor the beam alignment. Eight detectors were covered with Tantalum foil and five with Aluminum foil, the thicknesses of the foils were varied for forward and backward angles and the material as well. The foils were implemented in order to prevent the alpha scattered particles from reaching the detectors. The target was exposed for 8 hours, for each energy, in increments of 0.5 MeV. Once we obtained the data the total cross section was calculated by the differential cross section data to an expansion of Legendre polynomials. Hauser Feshbach calculations were made to compare how close our data points match with theory.

## **Introduction:**

It is known that the elements of the periodic table up to Iron are created in burning stars due to the energy generated as product of the reaction. The formation of elements more heavy than Iron is not yet fully understood. There are several processes of nucleosynthesis that explain how these elements and their isotopes are formed. Examples of some of them are the s- and r-processes. These theories use the neutron capture as the manner of formation of the heavy elements.

The s-process refers to a slow neutron capture process where the nucleus increases its mass and it can transform to the next element when one of the neutrons decay to a proton. This process occurs at low neutron flux and moderate temperatures. There is evidence that this process occurs in giant red stars where some isotopes heavier than Iron had been found in the spectral lines.

The r-process on the other hand refers to the rapid neutron capture. It only occurs in high neutron flux environments due to the necessity of some isotopes with short half-lives to be able to capture free neutrons and eventually decay to a proton. This process is thought to occur in supernovae.

Nonetheless the s- and r- processes are limited to explain the formation of nuclei and isotopes that are found on the neutron rich and the valley of stability of the charts of nuclei. For some of the proton rich portion of the chart there is no theory that explains the formation of such nuclei. In this work we want to determine the total cross-section of the  $^{65}\text{Cu}(\alpha, p)^{68}\text{Zn}$  and fitting to the Hauser-Feshbach calculations that describes it at the energies under study.[1] This kind of parameters are highly important for the astrophysics since it is very helpful to determine which processes are more likely to occur in the stars.[2]

### **Experimental Details:**

The FN Tandem Van de Graaff accelerator at the University of Notre Dame was used to produce the alpha beam. The Tandem accelerator used an external Helium Ion Source (H.I.S.) to generate such beam. There the helium was converted into a negative ion that was accelerated attracted to the center of the accelerator (terminal) with a high positive voltage. A thin foil of carbon of  $3\mu\text{g}/\text{cm}^2$  is found at the terminal, which strips the electrons from the negative ion beam, resulting in a positively charged beam that continues accelerating through the rest of the

accelerator repelled by the high positive voltage at the terminal. The alpha beam generated in this accelerator had an incident energy between 7.5 – 11 MeV range in increments of 0.5 MeV. The lowest beam energy reported a beam current of 160.0 nA, while 177.0 nA was registered at the higher energy. The running time was 8 hours for each energy. The chamber where the target and detectors were placed has a diameter of 1.5 meters. The target was a highly enriched with  $^{65}\text{Cu}$  (99%) with a thickness of  $632 \mu\text{g}/\text{cm}^2$ .

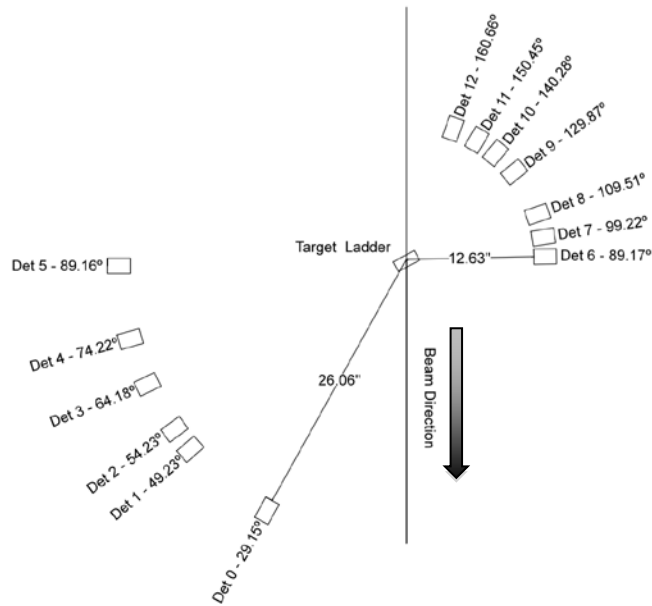


Figure 1: Detector positions inside scattering chamber. Det. 0, 1, 3, 5, 6, 9,10 and 12 had Tantalum foils; Det. 2, 4, 7, 8 and 11 had Aluminum foils.

Silicon Photodiode Detectors (S3590) with an active area of 9 x 9 mm were used to detect the charged particles produced at the target. The detectors were placed around the target at 13 different angles as show in figure 1. The detectors at  $\sim 90^\circ$  were placed to monitor the beam alignment. Tantalum foils of 1.50 mils and 1 mil thick were placed in front of eight detectors, four forward and four backward angles respectively, in order to stop the alpha scattering particles. Stopping such particles would provide a much cleaner spectrum, which makes it easier to detect the scattering protons, which have a probability of hitting the target several orders of

magnitude less. For the rest of the detector 3.15 mils of aluminum foil were placed to compare for possible contribution of background from the secondary reaction  $^{27}\text{Al}(\alpha,p)$ . The thicknesses of the foil were determined from the kinematics calculations shown in figure 2. Even though the energy of the protons is not highly dependent of the angle a significant decrease can be appreciated in the calculations. Since the forward angles receive higher energy protons the thickness of those foils were a few mils higher. The detectors were biased with 50V in reverse mode in order to increase the depletion region, area where the charged particle can be detected by electron-hole pair release. The detectors registered a leakage current of  $0.08 \mu\text{A}$  and  $0.13 \mu\text{A}$  for the backward and forward angles respectively. These magnitudes of currents were very stable through the whole experiment.

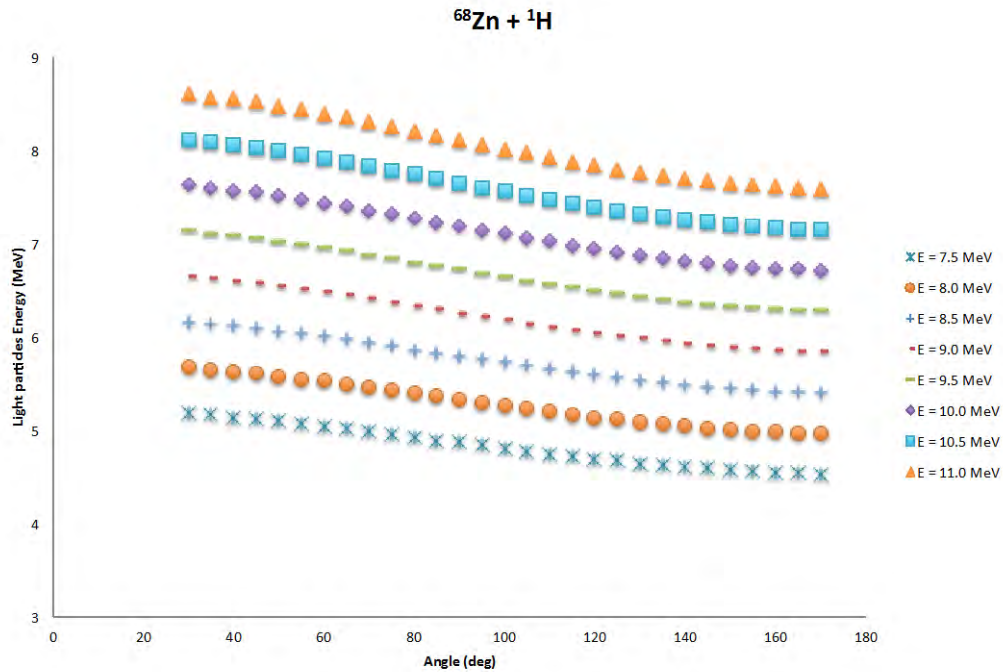


Figure 2: Kinematics calculations used to determine the thicknesses of the foils that were placed in front of the detectors.

## Results:

Differential cross-section was determined for each energy after the exposure of the  $^{65}\text{Cu}$  target to the beam. Each detector recorded a spectrum like the one shown in figure 3. With this data we were able to quantify how many protons were stopped in the detectors and how much energy those protons had. In the figure 3 we can easily define two peaks, which correspond to the protons of the ground and first excited state of the final state nuclei  $^{68}\text{Zn}$ . As the proton energy decreases in the spectrum, the peaks corresponding to more excited states of the nuclei become closer due to the small gaps between the states.

For each spectrum the two well defined peaks were integrated and a rough background correction and geometric corrections were performed. We obtained the differential cross-section for the first two groups of protons and each energy as shown in figure 4. A fourth order Legendre polynomial sum was implemented to fit the data.

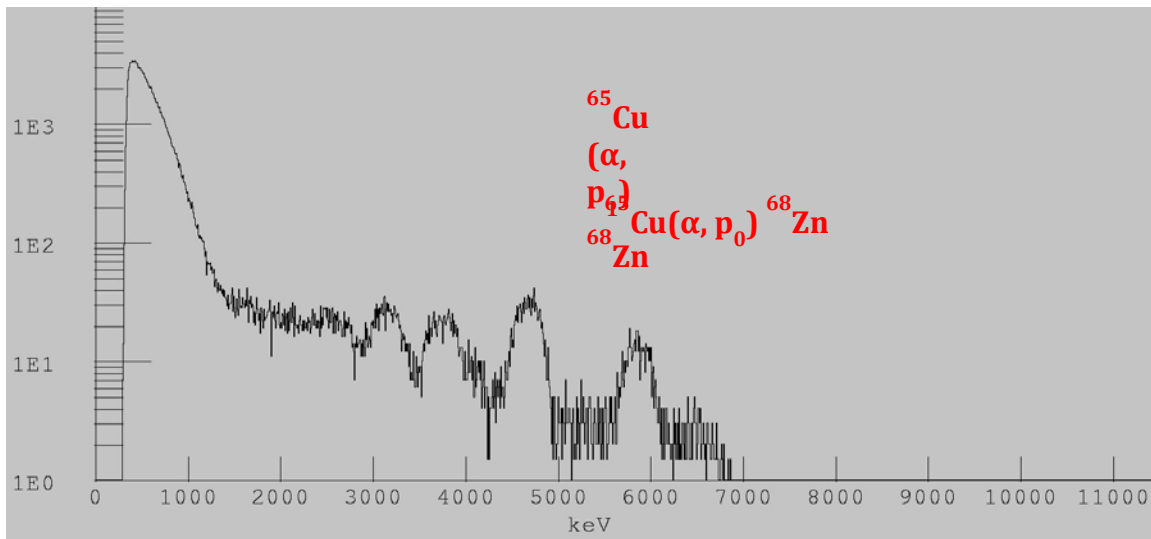


Figure 3: Spectrum for angle  $89.17^\circ$  from an  $\alpha$  beam of 10.0 MeV.

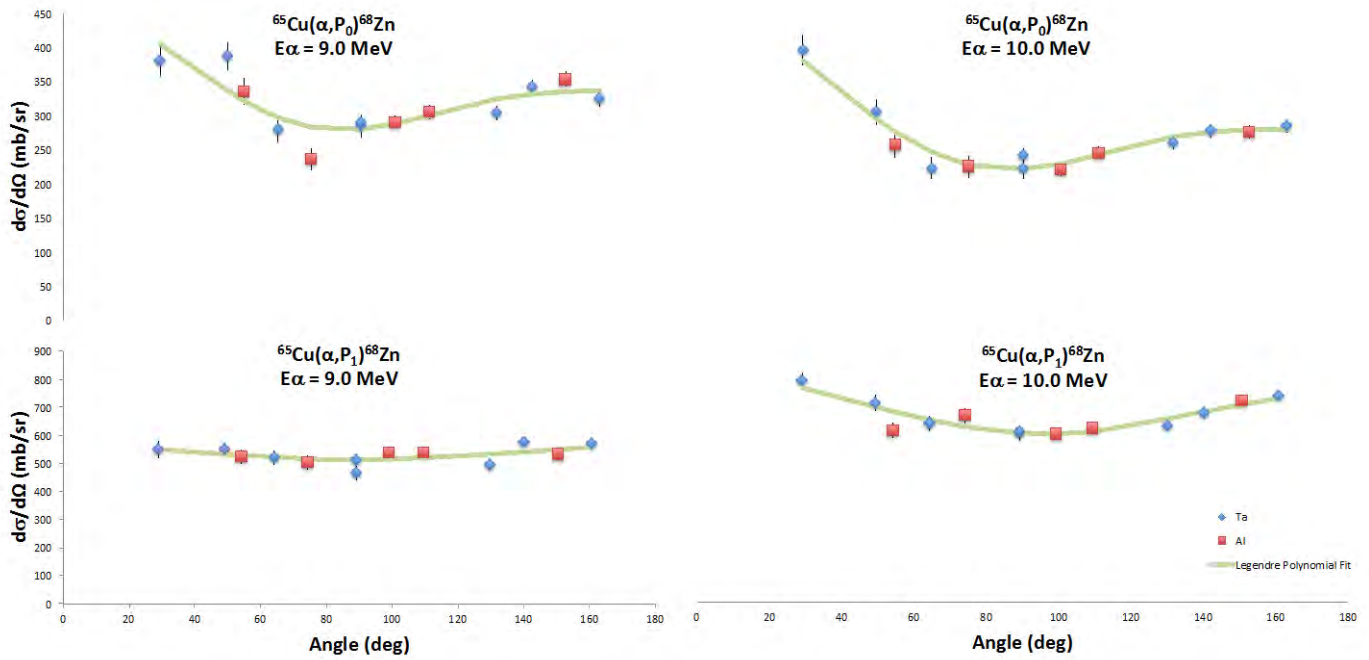


Figure 4: Differential cross-section for ground and first excited state protons. The solid lines correspond to the Legendre Polynomial fit.

The total integrated cross-section was obtained using the approximation of differential yield given by:

$$dY \approx N_b N_t \varepsilon \left( \frac{d\sigma}{d\Omega} \right) d\Omega \quad (1)$$

where  $N_b$  is the number of beam particles,  $N_t$  is the number of target particles,  $\varepsilon$  is the intrinsic efficiency of the detector and  $d\Omega$  is the solid angle. From equation (1) we can extract the differential cross-section and integrate to obtain the angle integrated cross-section as shown in figure 5. Hauser Feshbach calculations were made using the software Sapphire to compare our data with the theory, also plotted in figure 5.

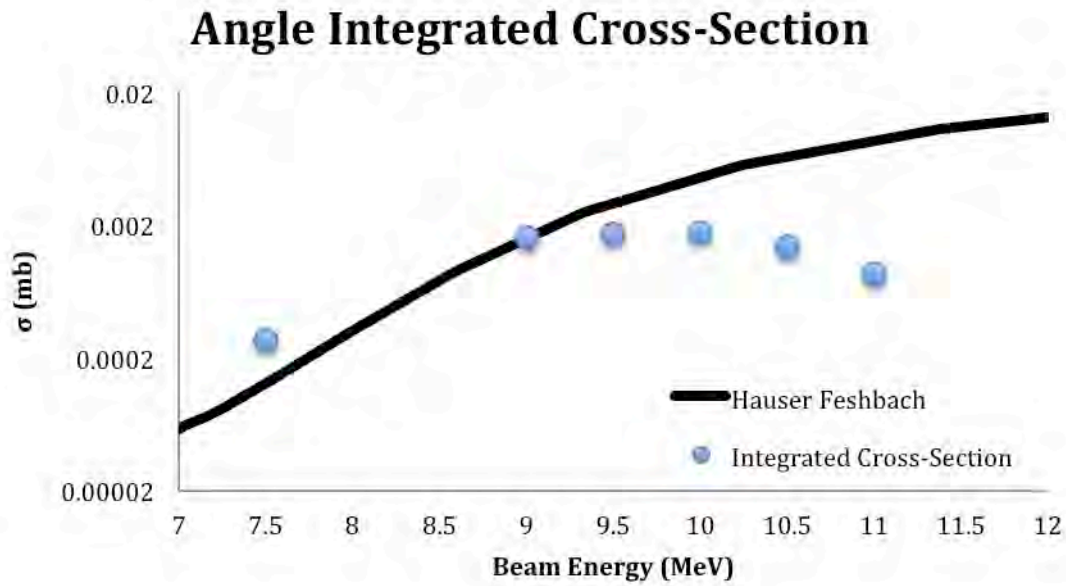


Figure 5: Angle integrated cross-section as function of beam energy.

The Thermonuclear reaction rate was calculated as well giving by:

$$N_A(\sigma v)_{01} = \frac{3.7318 \times 10^{20}}{T_9^{3/2}} \sqrt{\frac{M_0 + M_1}{M_0 M_1}} \int_0^{\infty} E \sigma(E) e^{-11.605 \frac{E}{T_9}} dE \quad (\text{cm}^3 \text{mol}^{-1} \text{s}^{-1}) \quad (2)$$

where the energy is given in the center of mass frame and the temperature in orders of Giga Kelvin[3]. Since the data points are close enough we can simplify equation (2) and get a good approximation given by:

$$N_A(\sigma v)_{01} = \frac{3.7318 \times 10^{20}}{T_9^{3/2}} \sqrt{\frac{M_0 + M_1}{M_0 M_1}} \sum E \sigma(E) e^{-11.605 \frac{E}{T_9}} \Delta E \quad (\text{cm}^3 \text{mol}^{-1} \text{s}^{-1}) \quad (3)$$

Using The Hauser Feshbach results we were able to calculate the reaction rate as shown in figure 6. Where we can see that it increases proportional to the temperature.

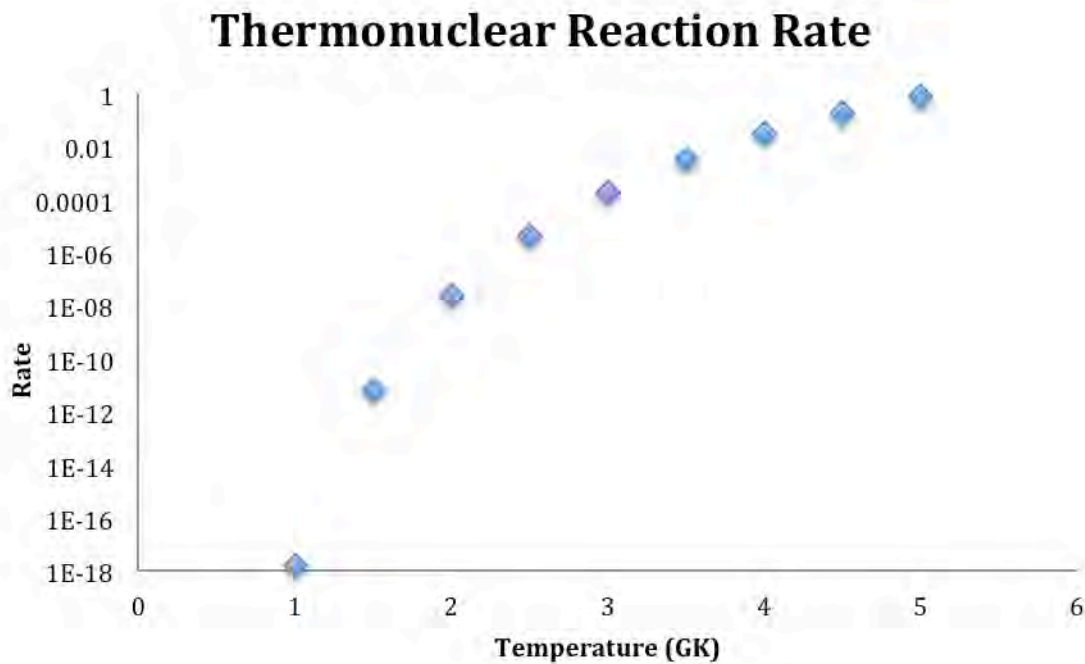


Figure 6: Thermonuclear reaction rate as function of temperature.

### Analysis and Discussion:

The integrated cross-section reported in this work as shown in figure 5 revealed to be fairly close to the theory by Hauser Feshbach at low energies, but as the beam energy increases the reported data and the theory present a discrepancy. Various uncertainties can contribute to this phenomenon. In figure 3 is shown a raw spectrum where we can distinguish  $P_0$  and  $P_1$ , which were the two protons energies studies in this work. This could represent a big factor that should be taken into account because at higher energies the higher states become more relevant to the angle-integrated cross-section. Other factor that should be taken into account is the fact that the background was not completely blocked by the foils neither Tantalum nor Aluminum as shown in figure 3. In fact there was no significant difference between the two types of foils. It is possible that secondary reactions had played a role in our measurements creating different discrepancies. The differential cross-section was not very consistence in terms of symmetry, but

most of them reported symmetry near  $90^\circ$ . This could be related to the background subtraction performed in the data analysis or some secondary reactions with the foils that were not taken into account.

## **Conclusion:**

The preliminary analysis for the first two groups of protons of the  $^{65}\text{Cu}(\alpha, p)^{68}\text{Zn}$  reaction performed in this work reported values close to the Hauser Feshbach theory for low energies. Discrepancies at high energies were reported. A detailed background subtraction and analyzing less pronounced proton peaks would improve our results making them closer to the theory. Secondary reactions studies can improve our preliminary analysis, since these reactions can contribute in a great manner to our uncertainties.

## **References:**

- [1] Islam, M., Boyd, R., & Corn, P. (1989). The  $^{63}\text{Cu}(\alpha, p)^{66}\text{Zn}$  Cross Section and the Corresponding Thermonuclear Reaction Rate. *Nuclear Physics, A504*, 367-373.
- [2] Palumbo, A., W. Tan, and J. Goïres. "Systematic Study of the  $\alpha$ -optical Potential via Elastic Scattering near the  $Z = 50$  Region for P-process Nuclei." *PHYSICAL REVIEW C* 85.035808 (2012): 11. Print.
- [3] Iliadis C., 2007, Nuclear Physics of Stars. Nuclear Physics of Stars, by Christian Iliadis. ISBN 978-3-527-40602-9. Published by Wiley-VCH Verlag, Weinheim, Germany, 2007.
- [4] DeBoer, R., D. Bardayan, and J. Goïres. "Low Energy Scattering Cross Section Ratios of  $^{14}\text{N}(\text{P}, \text{P})^{14}\text{N}$ ." *PHYSICAL REVIEW C* 91.045804 (2015): 10. Print.

# Effects of Cell Windows on TwinSol Beams

Kimmy Cushman

2015 NSF/ REU Program

Physics Department, University of Notre Dame

Advisor: Tan Ahn

## Abstract

*In order to study reactions with unstable nuclei, radioactive-ion beams must be used. One method for producing radioactive beams is the TwinSol experimental setup at the University of Notre Dame. At TwinSol, stable and unstable isotope beams bombard a gas target, where one atmosphere of gas must be confined from the surrounding vacuum. Thin foil windows are used to contain the gas in the cell. In order to optimize the quality of secondary beams from TwinSol, it is necessary to understand and minimize the effects of energy loss and straggling in the windows. We have investigated five different materials to test the strength and durability under typical TwinSol beam conditions. Preliminary results indicate that two of the materials are potential candidates for future TwinSol experiments. We have calculated the beam scattering, stopping powers and equilibrium foil window temperatures, which will help in determining the metrics needed to compare outcomes in future experiments. This work is the beginning of a process to improve the TwinSol design so that secondary beams produced with heavier ions such as Oxygen, Fluorine, and Neon can be pursued.*

## 1 Introduction

**W**hile chemical reactions give insight to molecules and electronic structure, nuclear reactions must be studied in order to better understand the structure of the nucleus. If the nucleus is organized in a specific way such as alpha clusters, we can search for these by measuring nuclear reaction cross sections. One method to probe structure is the bombardment of light nuclei with a heavy, radioactive nuclei, such as the reaction  $^{14}\text{O}(\alpha, p)^{17}\text{F}$ , a transition reaction which is a characteristic breakout reaction of the CNO cycle in astrophysical environments [1]. However, in the lab, we must replicate the reaction using inverse kinematics because  $^{14}\text{O}$  is unstable and cannot be used as a target. Therefore, it is useful to use radioactive nuclear beams because they allow for the study of reactions with unstable species. In an inverse kinematic reaction, the heavy primary beam directs the products in the forward direction, so that they may be detected more easily.

At the University of Notre Dame, two superconducting solenoid magnets make up the TwinSol design. The two magnets of up to 6 tesla each focus the path of the nuclear species to the detector, so the secondary beam of interest can be filtered from all reaction products. With the use of TwinSol, we are able to produce the reactions, and analyze the products of reactions with exotic nuclei. In typical TwinSol experiments, primary beam species include partially, or completely ionized Lithium, Boron, Carbon, Nitrogen, and Oxygen beams, which are accelerated by the FN-tandem accelerator to energies ranging from 30 to 80 MeV. The two most utilized target species in TwinSol experiments are  $^2\text{H}$  and  $^3\text{He}$ .

With the advantages of light nuclei target comes the disadvantage that the target is a gas. A gas target increases the complexity of the experiment because it must be isolated from vacuum. In order to overcome this problem, target windows must be used, such that the beam passes through the window, is allowed to react

with the target gas, and the secondary beam may pass through the window on the other side of the cell. This investigation will focus on the effect of the cell windows on TwinSol experiments.

## 2 Methods

The gas window used in previous TwinSol experiments were 5  $\mu\text{m}$  Titanium foils. One of the most important properties of gas cell window is that is essentially invisible to the beam, because we are interested in the reactions with the gas, and not the foil itself. To approach this optimization, a very thin foil may be used. The strength of a foil is determined by its thickness, so a foil can only be as thin as its strength against vacuum allows. However, in order to produce a practical amount of reaction products, one atmosphere of gas is typically contained within the cell, and such a pressure gradient leads to stress on the windows. Therefore, the window material has to be relatively strong, making Titanium a good option as a gas cell window because of its high tensile strength.

Another key feature of the optimal window material is that it has a low density, because similar to the thickness, less material reduces the amount of unwanted reactions with the window. Any material which is subject to a nuclear beam has a unique stopping power,  $dE/dx$  which is proportional to  $Z^2$ , so a low  $Z$  material will absorb less energy from the beam. Similarly, a low density material will yield lower energy straggling. When the beam passes through the window, it loses energy due to the electric and nuclear forces experienced between the beam and the material. Thus, it is decelerated as it is kicked in various directions along its path through the foil, increasing the spread in energy of the beam. We would like to diminish effects of stopping power and reduce energy straggling in the beam in order to increase the resolution of the beam and thus reduce the error of the calculated cross sections of reactions. By selecting a window of low density and thickness, the effects of stopping power and straggling of the primary and secondary beams are greatly reduced.

Another factor to consider in selecting a foil is whether it will be able to withstand the heat of the beam. The energy lost by the beam is absorbed by the foil, so it is heated during an experiment. Window materials which are thermally conductive will be able to dissipate the heat of the beam, which is focused to a diameter of a few millimeters. Having a low thermal conductivity, however, can be supplemented by having a high melting or degradation temperature. Both of these properties must be weighted in determining the usability of a window material. Electromagnetic radiation is the only method for heat dissipation on the vacuum side of the window, while the gas side of the window will be able to conduct heat via conduction to the gas. This conduction increases the average kinetic energy of the gas molecules, therefore increasing the pressure of the gas inside the cell. This is key factor because the initial pressure of the gas cell may greatly increase, yielding greater stress on the window.

Therefore, possible window material alternatives are evaluated based on the following properties:

- tensile strength
- mailability, thickness
- density
- thermal conductivity
- melting/degradation temperature
- availability
- cost

In the investigation of window materials, several foils were selected as strong candidates, and considered for the window testing experiment.

Another aspect of the investigation was the theoretical portion. Using the SRIM (The Stopping and Ranges of Ions in Matter) program [2], stopping powers of each of the candidate windows were calculated for each of the typical TwinSol beams. The stopping powers were used to calculate the power and energy implanted in each of the windows. Also, each of the materials dissipates the heat uniquely, so given a beam current, equilibrium temperature is reached. If this temperature is within the range of usability for the material, this current would be suitable for use in a TwinSol experiment. For each material, the maximum current load was calculated using the VTL (Virtual Target Lab) program [3]. By calculating the stopping powers of each beam and foil combination, it was possible to evaluate the data collected in order to compare to the theoretic results obtained by VTL.

### 3 Experimental Design

With the selection of a short list of foils based on their theoretical properties, it was necessary to test them in real experimental conditions. Along with the testing of alternative foils, this investigation was also meant to test the new gas cell chamber design(Figure 1b). The new design implements four separate gas cells inside the chamber, so that when a window fails during a TwinSol experiment, the vertical drive attached to the cell columns can engage to place a new cell in the beam line. This design allows TwinSol experiments to run for a longer period of time with shorter interruptions, rather than having to vent the cell chamber and replace the window each time it fails. Because of this, the multiple cell design also reduces radiation exposure during experiments. Another feature of the new cell handling system is that the vertical drive will also be used in one test to oscillate the location of the beam on the foil, in order to distribute the heat of the beam across more of the window's surface area.

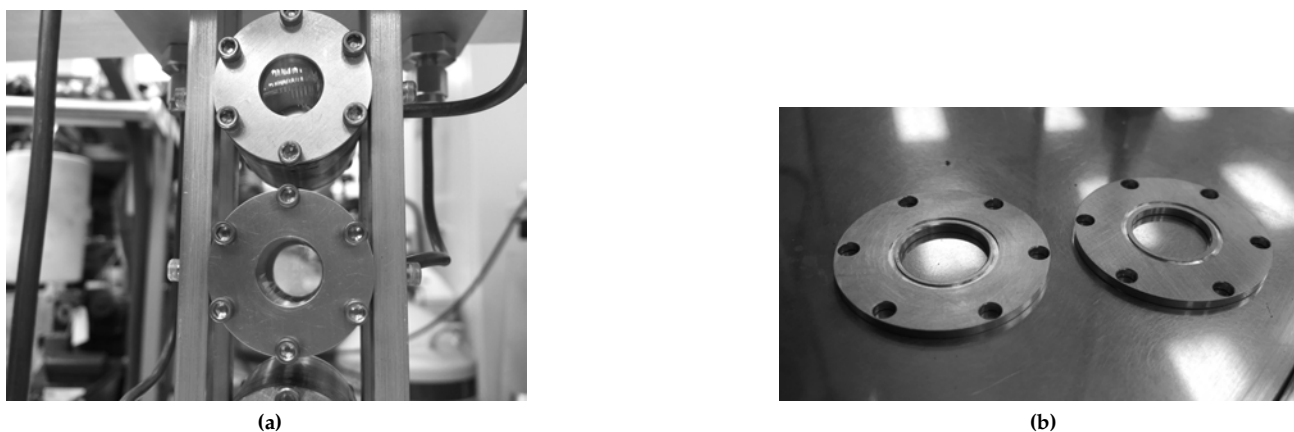


**Figure 1:** a) Picture of the gas cell design, where four cells are aligned vertically, for efficient adjustment to a new cell when a window fails. b) Gas cell windows frames detached from the cell. The windows can be attached to the frames for easy mounting.

The first step of the experimental portion of the investigation was to integrate the new gas cell design into functional use, and to find the best method for mounting the foils to the gas cells. The most direct method for mounting the windows is to place them on the cell over the O-ring, and screw in the window frame on top of the window to hold it in place. However, this method requires the cells to be in a horizontal position, and because the chamber is cumbersome and difficult to place on its side, so the process was inefficient. We also tested the use of vacuum epoxy to adhere the window to the frame. When testing this method, the fact that the windows were attached to the frame made mounting very easy because the window and frame could be mounted vertically. However, after several trials of vacuum testing, the cells continuously leaked, due to ripples and bubbles in the epoxy. The best method for mounting the windows was applying a very thin layer of vacuum grease to the frame, and then setting the window in place. The grease allowed the window to adhere to the frame so that it could be easily mounted vertically, yet it was not a physical barrier from the seal of the O-ring as the epoxy was.

The central experiment of this investigation was the vacuum and beam test, which were meant to mimic typical TwinSol conditions. The following materials with the given properties were tested:

Material	Thickness $\mu\text{m}$	Tensile Strength MPa	Density $\text{mg}/\text{cm}^3$	Thermal Cond. W/mk	Melting/Degradation Temperature $^{\circ}\text{C}$
Titanium	5	246-370	4.50	21	1668
Molybdenum	2.5	550-650	10.8	138	2623
Aramid [4]	4 and 12	392-490	1.5	n/a	300-350
Aluminized Mylar	24	Mylar 196 Aluminum 40-50	1.39 2.70	<1 237	254 660

The Titanium was used in the experiment to align the beam and act as the control group. The material of Molybdenum was chosen because of its high tensile strength, conductivity, and melting point. However, its relatively high density was a drawback to this material, so a very thin window was required. Although the Aramid material has low thermal durability, its tensile strength allowed for a thin window to be utilized. A low

density material yields less beam energy loss, and therefore less heating of the material itself. The Mylar was chosen to test the capability of the vertical drive for oscillation and its effectiveness in increasing the lifetime of the windows. Therefore, one test was conducted on the Mylar as a control with no oscillations, and one was tested with oscillations, using the same beam and vacuum conditions.

In the experiment, a 5+ charge state Carbon beam was accelerated to 42.5 MeV by the FN-tandem accelerator.  $^4\text{He}$  gas filled the cells to approximately atmospheric pressure. For every given test, the parameters to be considered include:

- beam species
- charge state
- beam energy
- beam current
- pressure inside the cells
- time exposed to current
- continuity of beam current/interruptions
- size and shape of beam spot
- beam alignment with cell
- percent transmission

In order to properly compare the durability and performance of each material, only the beam current and time should be adjusted. The pressure inside the gas cells is to be monitored by a digital pressure gauge, and recorded throughout the experiment. The procedure for each test is to begin at a low current of 50 nA for tuning, and then increase the current until the window breaks or significantly leaks. The failure point is easily noted because the pressure gauge will show a marked decrease in pressure, until all of the gas is evacuated by the vacuums.

## 4 Results

### 4.1 Vacuum and Beam Experiment

The ideal procedure for testing each window material is to run the same beam current on each and increase the current with consistent frequency until each of the windows failed. However, this method is unrealistic given the many parameters which must be controlled and the time constraints of the experiment, so the tests must be compared with caution. Nevertheless, the results of the experiment were very useful in providing the first metrics against which to compare theoretical results. Table 1 displays the integrated current exposed to each set of windows before it failed. Data from the Aramid and Molybdenum tests is shown in Figure 2, plotting beam current and gas cell pressure against time. A similar graph of the data from the Mylar tests compares results of a stable cell versus an oscillating cell.

Window Material	Integrated Current pA · hr
5 $\mu\text{m}$ Titanium	1.27
5 $\mu\text{m}$ Titanium*	4500
2.5 $\mu\text{m}$ Molybdenum <sup>†</sup>	723
4 $\mu\text{m}$ Aramid	35.0
12 $\mu\text{m}$ Aramid	273
24 $\mu\text{m}$ Mylar no osc.	16.7
24 $\mu\text{m}$ Mylar w osc.	16.4

**Table 1:** Titanium window used to align the beam and received the smallest integrated current. Integrated current on Titanium\* is the best performance of Titanium windows in previous TwinSol experiments. The Molybdenum windows received the highest integrated current by a large factor, without failure<sup>†</sup>. The integrated current of the Aramid and Mylar windows is the total current reached before failure.

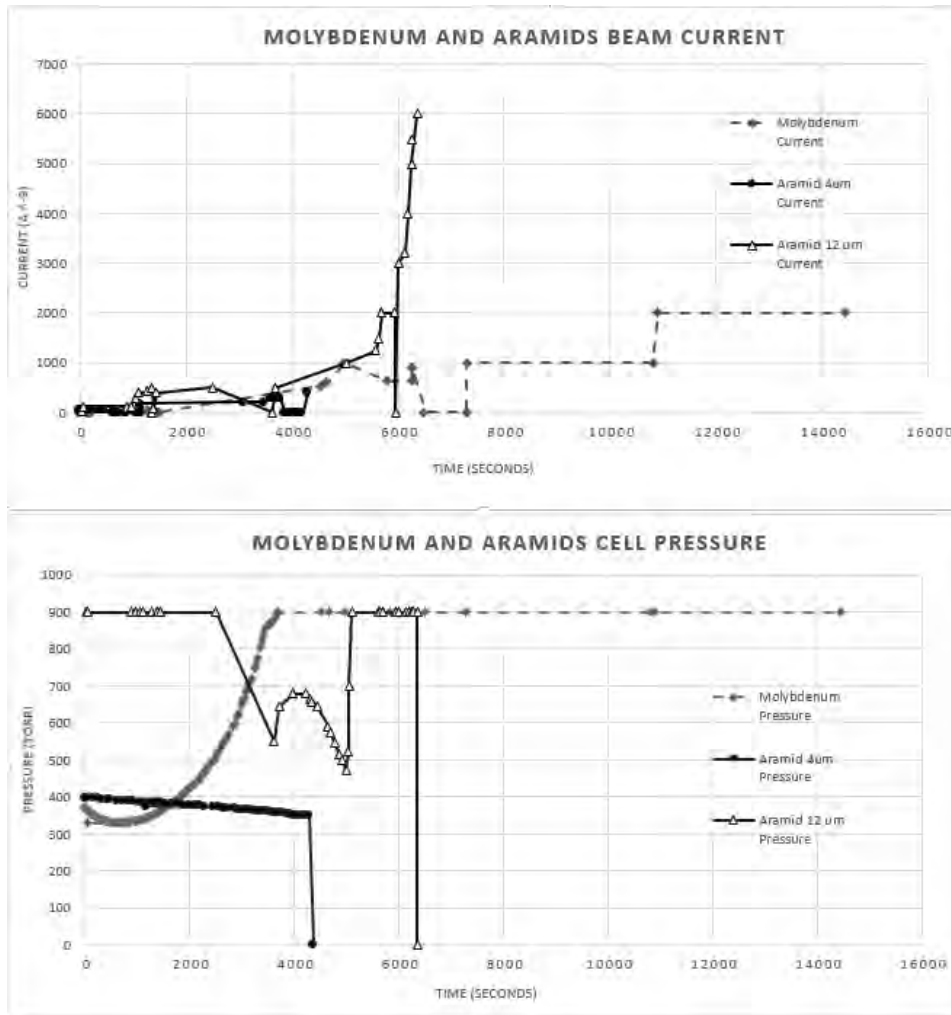


**Figure 2:** Beam current and gas cell pressure plotted vs time. Note that both of the aramid windows failed and released pressure to vacuum, while the Molybdenum window remained at the threshold pressure of 900 torr.

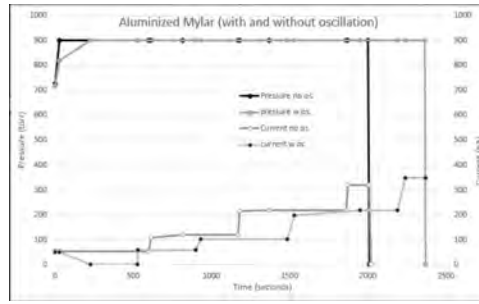


**Figure 3:** The Mylar window with no oscillation received slightly more current, but the interval of increase remained approximately every ten minutes for both. See Table 1 for integrated comparison. Also note that both of the cells reached the threshold pressure shortly after the start of each test.

## 4.2 Theoretical Results

Using SRIM stopping power tables, energy loss was calculated for each of the window materials given initial beam conditions. Figure 4 contrasts the fractional energy loss of a range of Carbon beam energies in Titanium and Aramid windows against the thickness of the material. Where the gradient is black, indicating a fractional loss of 1, all of the beam energy is lost because at low beam energies and high window thicknesses, the beam does not have enough energy to escape the window, so it acts as a beam stop. Even when the thickness of Aramid is double that of Titanium, the energy loss in Aramid is less.

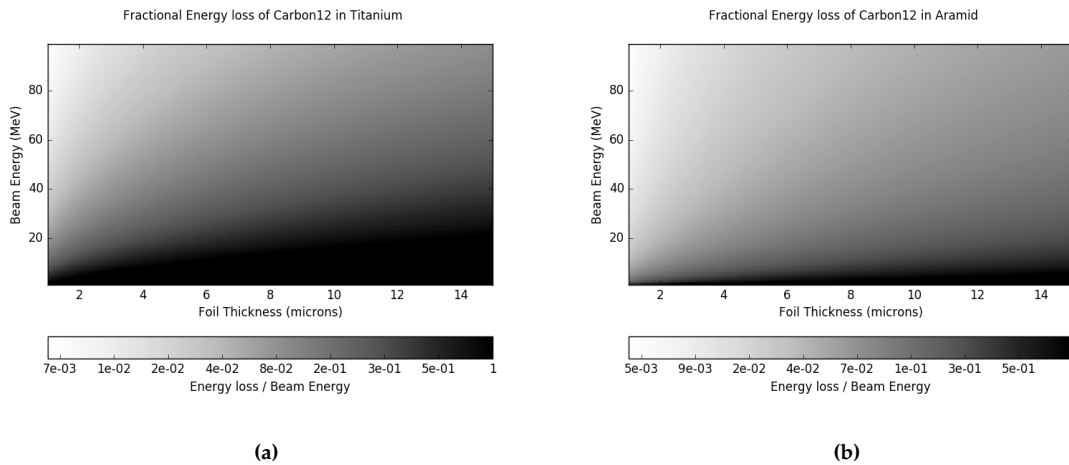


**Figure 4:** Contrast the fraction of beam energy loss in Titanium (a) versus the less dense Aramid (b).

## 5 Discussion and Future Research

Preliminary results of this investigation indicate that Molybdenum and Aramid may be suitable alternatives to Titanium for TwinSol gas cell windows. If Molybdenum is to be used, a very thin foil, such as the  $2.5 \mu\text{m}$ , should be used because Molybdenum is a high  $Z$  element, compared to Titanium (42 vs. 22). The density of Molybdenum is  $10.8 \text{ g/cm}^3$ , while that of Titanium is  $4.5 \text{ g/cm}^3$ . Although this increases its stopping power,

Molybdenum has a much higher melting point and thermal conductivity, so it may be advantageous in having a long lifetime of use in experiments. An alternative with opposite characteristics was found to be the Aramid foils. Having a low density of  $1.5 \text{ g/cm}^3$ , this material has a low stopping power, which is optimal for maintaining the resolution of primary and secondary TwinSol beams. However, it may not have a long lifetime of use under high beam currents. Therefore, the specificity of each TwinSol experiment may determine which window material may be ideal.

## 5.1 Experimental Complications

In the vacuum and beam experiment, each window material was not tested under the same conditions. The valve used to control the input of Helium to the cells was not well controlled, so the initial pressures varied from 370 torr to over 900 torr. Another issue that arose during the experiment was that the digital pressure monitor had a maximum reading of 900 torr, therefore, pressures above this threshold were uncertain. A related problem was that after filling the cells equipped with the  $12 \mu\text{m}$  aramid windows, the gas pressure increased with no exposure to beam or a gas source. The reason for this error may have been that the valve between the gas source and the cell was leaking.

Similarly, the gas cells did leak slightly, at a rate of 0.5-2 torr per second. The leaking introduced an uncertainty about the effect of the gas heating to pressure increase. For example, the Molybdenum sample was leaking significantly, from 372 torr at the beginning of the run to a minimum of 330 torr after 10 minutes. After this point, the gas pressure inside the cell increased to over the threshold of the pressure gauge.

Another factor which induced error to the experiment was the sparking of the accelerator. After each spark, the beam required retuning, so the windows were allowed to cool down, thus inducing the thermal stress of cooling and reheating to the windows.

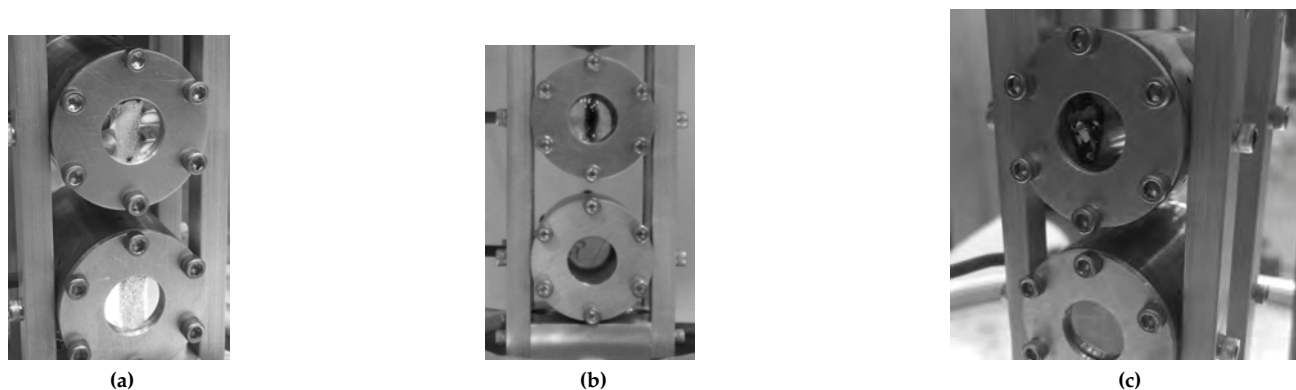


**Figure 5:** *a) The top window received no oscillation, while the lower window oscillated during beam exposure. Note that the beamspot wear on the un-oscillated window is also vertical. b) The burn mark on the  $4 \mu\text{m}$  Aramid (top cell) illustrates the vertical spread of the beam without oscillations. c) The  $12 \mu\text{m}$  Aramid window failure. Rather than a leak, this failure was clearly a burst.*

The shape of the beam spot affected the result of the oscillation test. After inspection of the Mylar window which received no oscillation of the beam, a burn mark on the window appeared as a vertical line (see figure 5a), so the vertical oscillation of the beam on the other Mylar window provided a redundant spread of the beam in the vertical direction. Also, because of the shape of the beam spot, the recorded current at the beam stop decreased as the beam moved to the edges of the window. Therefore, some of the beam was absorbed by the window frame, rather than the window.

## 5.2 Future Work

This investigation was meant to be the beginning of a process to improve the Twinsol design and understand how the gas cell windows affect the primary and secondary beams. From this point, outputs from SRIM and VTL may be used with the accompanying codes for calculations so that more alternatives may be explored. The experimental procedure can be also followed in future tests to compare the material performances. In future experiments of this type, it could be beneficial to implement an infrared heat camera to image the windows and monitor their temperature on line. With this apparatus, theoretical equilibrium pressures from VTL could be compared to experiment.

Although the conditions required for this experiment were considered for TwinSol, understanding the effects of gas cell windows on nuclear beams is not unique to experiments conducted at the University of Notre Dame. For any experiment where a gas target is required, methods for investigating alternative window materials would be beneficial.

## References

- [1] J. Hu et al. "Examination of the role of the  $^{14}\text{O}(\alpha,p)^{17}\text{F}$  reaction rate in type I x-ray bursts." Phys.Rev. C90 (2014) 2, 025803.
- [2] J. Ziegler, SRIM (The Stopping Ranges of Ions in Matter), software available at <http://www.srim.org>
- [3] S. Kasemann, VTL (The Virtual Target Lab), University of Cologne 1996
- [4] Toray Industries, Inc. [http://www.toray.com/products/fibers/fib\\_012.html](http://www.toray.com/products/fibers/fib_012.html)

# **Project GRAND: Data Acquisition and Corrections**

R.C. Dennis

*2015 NSF/REU Program*

*Physics Department, University of Notre Dame*

Advisor: Dr. John Poirier

## ABSTRACT

Project GRAND, a cosmic ray experiment, is located north of the Notre Dame campus. Spanning a 100 by 100 square meter area, this detector has been used to study gamma ray burst events as well as solar phenomenon such as a Forbush decrease. The quality of the data from this and previous years was improved this summer by utilizing a pressure correction and generating accurate time data. A new backup system was also employed to ensure that the data exists on multiple drives.

## I. INTRODUCTION

Project GRAND (Gamma Ray Astrophysics at Notre Dame) is the first of its kind and consists of an array of cosmic ray detectors. Arranged in an 8x8 grid, this 10000 square meter apparatus consists of 64 huts. These huts are able to determine both position and angle of particle entry using devices known as proportional wire chambers (PWCs). This massive array is capable of detecting cosmic rays from solar and extrasolar sources. The peak sensitivity is 56 GeV. Each of these huts is filled with a gas that consists of 80% argon and 20% carbon dioxide. As the PWCs have an area of 1.29 m<sup>2</sup>, the total detection area is 82 m<sup>2</sup>. [5] For more details on the experimental setup, see Table I.

## II. PROPORTIONAL WIRE CHAMBERS

The huts at project GRAND each contain 4 pairs of proportional wire chambers. Each of these chambers consists of 80 parallel wires with an applied voltage of 2600 V. Each pair of chambers has 80 wires that run from north to south and 80 wires that run from east to west. This gives a total of 640 wires per hut. As a charged particle enters the apparatus, there will be a current in the wire that is closest to its trajectory. Using the data from each pair, we are able to determine where in the plane the particle entered the apparatus. Because

Quantity	Symbol	Value
Number of Detectors	N	64 Huts
Recorded Muon Rate Per Detector	$R_\mu$	$37.5 \mu * s^{-1} \text{det}^{-1}$
Total Observed Muon Rate	$N * R_\mu$	2400 $\mu/s$
Instantaneous Data Rate	$R_{\text{readin}}$	600 MHz
Muon Event Fraction	$R_\mu / (R_\mu + R_e)$	$\sim 75\%$
Muon Detection Threshold	$E_{\text{th}}$	0.1 GeV
Single Cell; Width, Height	w,h	14 mm, 10 mm
Vertical Spacing Between Planes	H	200 mm
Total Number of Wires	$N * W$	40960
Single Detector Area	S	1.29 m <sup>2</sup>
Total 64 Detector Area	$N * S$	83 m <sup>2</sup>
Total Area of GRAND	A	10000 m <sup>2</sup>

TABLE I. Vital Statistics for Project GRAND

there is a stack of four pairs of PWCs in each hut, we are also able to determine the angle of entry.

As a charged particle enters the chamber, it will cause an ionization event to occur in the gas. The resulting ions and electrons are then attracted to the wires because of the strong electric field. This attraction leads to a cascade of ionization events which ultimately leads to a current in the wire (See Figure 1).

As we wish to distinguish between electrons and muons, there is a 50 mm steel plate located between the third and fourth pair of chambers which prevents 96% of the electrons from reaching the final pair of chambers. This fact coupled with the fact that there are three times as many muons at ground level allows us to be 99% certain that an event that registers on all 8 chambers in a linear fashion is a muon. Next, the data we collect is placed

in two separate camps. The first camp is single muon events and the second camp is shower events. When events are seen in six nearby huts at nearly the same time, the software deems this a shower event and places the data in a separate file.[3][4]

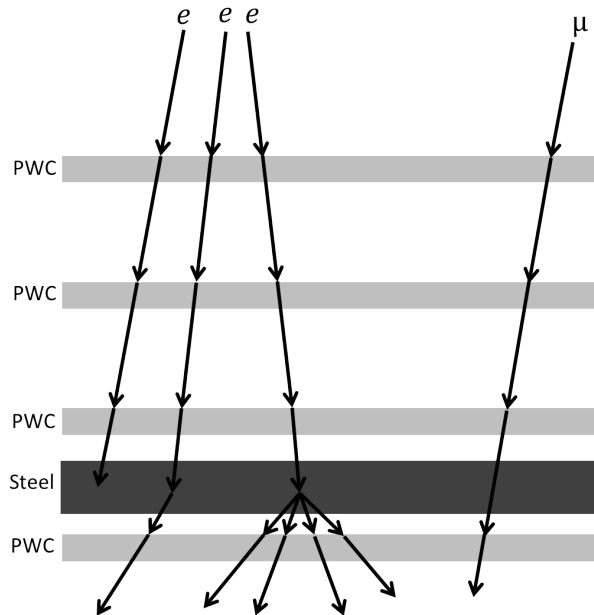


FIG. 1. This demonstrates the trajectories that are likely to occur for electrons and muons. The muons tend to travel straight through the steel, but the electrons are stopped, deflected, or create showers due to the steel. This is exploited for particle identification.

### A. Maintenance

As the huts are negatively affected by both temperature and humidity, each hut is equipped with a dehumidifier and a heater. In the winter months, the huts have a tendency to decrease in effectiveness. By accessing some of the experimental data, the GRAND Data Lab website allows us to track the status of individual huts and indicates the type of problems that arise. In the summer months, we use this data to improve the status of the malfunctioning or inefficient huts.

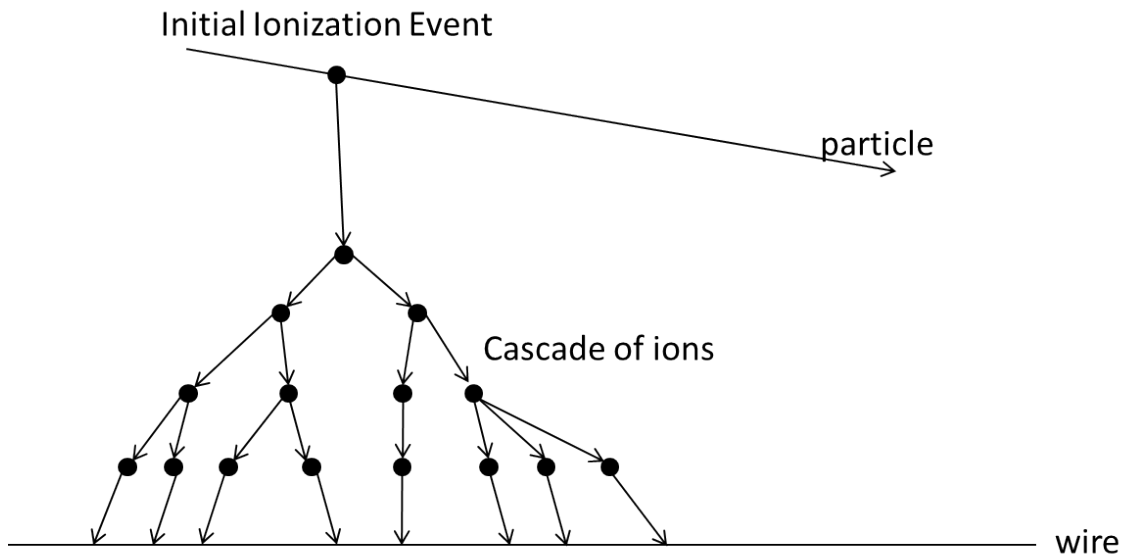


FIG. 2. Ionizing radiation causes an initial ionization event in the argon/carbon dioxide gas and the electric field produced by the wire amplifies this effect to create a current.

### III. APPLICATIONS

Originally used to study gamma ray bursts, project GRAND is also used to study solar effects. After a coronal mass ejection, the resulting magnetic field produced by the sun causes a sharp decrease in the observed cosmic ray intensity as the cosmic rays are swept away from the Earth. This is called a Forbush decrease and data from this project has been used to study this phenomenon.[3][4]

### IV. ALTERING THE TIMESTAMP

Because the Earth is constantly rotating, in order to make sense of our data, we need information about the Earth's orientation. Pairing our data with a timestamp will achieve this goal. In prior years, there were three clocks that provided timestamps for the experiment. The computer that runs the primary program (DAS) names the file with the day of the year as well as the hour and the minute. Each file contains an hour worth of data,

so this computer clock can be used very coarsely. Time information was also collected via WWVB, a time signal radio station, and via a megahertz oscillator. The WWVB source provided the most accurate time data with the precision of a second. The MHz clock—which like the computer clock—drifts in time and is not synchronized. For years, these three clocks all worked adequately, but in 2014 the WWVB clock was disconnected and months later the MHz clock failed as well. For some time, the only point of reference for the data we received was the timestamp given by the filename.

Utilizing past information, we were able to determine how the filenames drift in time and determine time information for each dataset that is accurate to better than a minute. We also looked at how the clocks' amount of drift changes seasonally. Finally, we were able to create a program that determines how the computer's internal clock compares to standard time and we modified the data acquisition program to provide a timestamp for each set of 900 muons.

## V. DATA ACQUISITION

The main program that runs nearly continuously is called DAS (data acquisition system). This program began the summer on edition 33 and ended the summer on edition 43. Quite a few changes were made for the benefit of creating backups for the files and for providing the aforementioned time information.

### A. Backup System

Prior to this summer, the data was backed up twice using very complicated programs. There are three types of files that we are concerned with: single muon event files, shower event files, and dayfiles (a summary of the number of muons detected by each hut in a ten minute interval). Each of these files is backed up in two places. The previous program that automatically backed these up would occasionally create a copy before the file was written

or miss a file altogether. Instead of searching the directory for the files and attempting to determine if they were complete, we altered the DAS program to pass the names of those completed files to a text file that would then be accessed. This new method of creating backup files, though complicated, is much simpler than what was running before and has thus far been successful in performing the intended tasks.

### **B. Time Information**

The main computer (5100) for our experiment does not have a synchronized clock, but we found a method for determining how slow it runs by comparing it to the clock of a synchronized computer. With this information, we decided to alter the DAS program to write the year (4 bytes) and Unix time (number of seconds since 1 January 1970 GMT) (8 bytes) in place of the MHz clock. We attempted to get the MHz clock back online this summer and while we were successful for a short period of time, this remains nonfunctional.

### **C. Reformatting Dayfiles**

Another revision to the DAS program was to reformat the dayfiles. The previous format was not fixed and caused issues when read by GRAND Data Lab or any other program we wrote. By making this a fixed format, inserting unix time, and getting rid of colons and slashes, the dayfiles became much simpler to handle. With this, we also had to write a program to reformat the dayfiles from past years to agree with what is now being produced.

## **VI. GRAND DATA LAB**

GRAND Data Lab is a website that uses programs written in C to access and display the dayfile data in graphics. As previously mentioned, this makes the data easier to analyze and assess and it is useful in diagnostics. Using 14 programs, this website provides options

to correct for both pressure and good huts.

### A. Pressure Correction

Muon flux is subject to atmospheric effects. As cosmic rays travel toward earth, they lose energy due to ionization effects prior to reaching the ground. It follows that the a higher air density allows for more of these ionization events to occur and thus fewer muons to reach the ground. Clearly temperature plays a role in this, but the effects due to pressure are more significant. To correct for pressure, we use the formula

$$N = N_0 \exp [\beta (P - P_0) / P_0] \quad (1)$$

where  $N$  is the corrected count,  $N_0$  is the observed number of muons,  $\beta$  is the barometric pressure coefficient,  $P$  is the pressure, and  $P_0$  is atmospheric pressure. This can also be approximated by the linear equation

$$N = N_0 \left[ 1 + \beta \left( \frac{P - P_0}{P_0} \right) \right] \quad (2)$$

because

$$\beta (P - P_0) / P_0 \ll 1. \quad (3)$$

The GRAND Data Lab program has a feature that allows the user to make this pressure correction before viewing the data. As someone discovered years ago, this calculation was being done incorrectly. Past REU students attempted to determine where the issue lies, but were unsuccessful. One of the past attempts at finding the issue involved finding the pressure value that was used by the program and comparing it to the pressure value that should have been used. The program that performed this procedure had a flaw, but once that was fixed, the error was still unclear. After searching in the code and making test modifications, we determined that there were multiple issues. The main issue was that the program introduced a five hour offset between the pressure data and dayfile data. After

correcting all of the issues that we found, the pressure correction was finally being done correctly (See Figure 3).

To further improve this correction, we also added a line of code that removes pressure data which is inconsistent with reasonable values and this change caused some of the data spikes to disappear.[1][2]

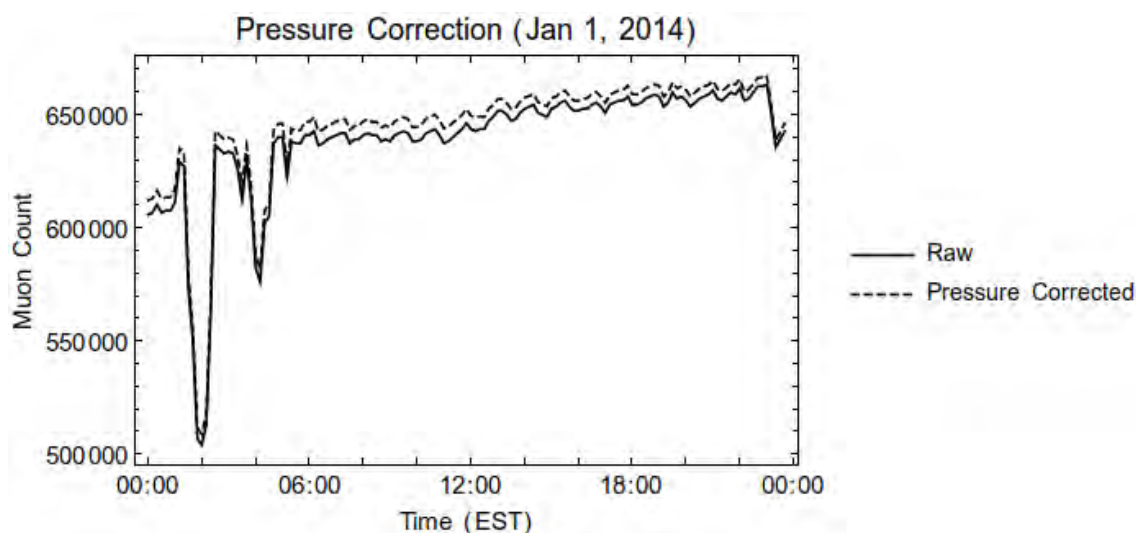


FIG. 3. Each data point represents the total number of muons detected by Project GRAND in a ten minute period. The dashed line represents the data after the count has been corrected for the pressure at that given time.

## B. Muon Count Correction

Each of the points in our dayfile plots (See Figure 3) represents the number of muons counted in a ten minute interval. There are times, however, when more or less than ten minutes of data is recorded. We wrote a program that effectively remakes the dayfiles after removing these unrepresentative blocks of data as well as blocks of data that contain errors. In doing so, we implemented a much simpler format for the files, but still need to modify the GRAND Data Lab program to accommodate these revisions.

## VII. CONCLUSION

Much was accomplished for Project GRAND this summer. The huts were properly serviced and the software was improved significantly. By salvaging data through parameterizing the 5100 clock, introducing a new timestamp for the data records, improving the state of GRAND Data Lab, and creating a reliable backup system, Project GRAND is working much more effectively.

## VIII. ACKNOWLEDGMENTS

I would like to thank Dr. Poirier for helping me get the most out of my summer with this excellent research experience. I would also like to thank Aaron Sawyer, Calvin Swartzen-druber, and Susan Sakimoto for their hard work this summer. Finally, I want to thank Dr. Garg for making this an excellent program and for allowing me to participate in it.

- 
- [1] Catanach, Tom. *Atmospheric Corrections and Periodic Variations at Project GRAND*. Scientia. Vol. **3**. 2012.
  - [2] Poirier, J. and Catanach, Tom. *Atmospheric Effects on Muon Flux at Project GRAND*. **32nd International Cosmic Ray Conference**. Beijing. 2011.
  - [3] Poirier, J. and C. DAndrea. *Status Report on Project Grand*. **30th International Cosmic Ray Conference**. 2007.
  - [4] Poirier, J. *Status Report on Project GRAND*. **32nd International Cosmic Ray Conference**. Beijing. 2011.
  - [5] *Project GRAND In-depth Description*. University of Notre Dame. Web. 04 Aug. 2010. <http://www.nd.edu/grand/grand.html>.

Improving the Low-Energy Electron Beam for  
Electron-Molecular Interactions

Victor Garcia

2015 NSF REU Program

Department of Physics, University of Notre Dame

Advisor: Sylwia Ptasińska

## Abstract

Low-energy electrons (LEEs) have shown to be capable of inducing severe damage to DNA. LEEs are generated through the ionizing radiation interacting with the matter. To better understand how these electrons cause DNA damage, cross beam experiments were often used, which probed the formation of the electron-induced fragmentations of isolated molecular species by using mass spectrometry in later experiments. A well-focused electron beam is necessary to have optimal interaction between both the electron beam and the molecular beam.

## Introduction

Low-energy electrons have been shown to cause genotoxic effects in living cells via mutagenic, recombinogenic, and other lesions in DNA. Initially, these effects were thought to be produced by direct impact of radiation. This is not the entire case as significant damage was found to be caused by the secondary electrons produced by the incident radiation. DNA damage is greatly dependent on the initial kinetic energy of the incident electron [1]. Better understanding about LEEs can lead the way for future benefits, such as a new form of cancer treatment.

The process by which the damage is induced by LEEs is through dissociative electron attachment. Through this process, a temporary negative ion will form as the result of the resonant electronic capture. The temporary negative ion can decay into neutral fragments and a negatively charged ion according to the reaction [2]:



This process can be studied by a cross electron/molecular beam experiment.

Because the electrons are at low energies, there are necessary precautions in the experimental design that must be taken to optimize the efficiency. The electron beam must have

a high energy resolution. This condition is important to observe the damage done to DNA at certain energies. Once the energy spread is reduced, the beam must be focused to improve the probability of the electron interaction with the biomolecules. The low energies of the electrons will also leave them extremely susceptible to external magnetic fields, mainly the Earth's magnetic field. The effect of these external fields can be minimized through the use of magnetic field control.

### **Experimental Setup**

In order to study the damage caused by the LEEs, the following experiment will be conducted inside of an ultrahigh vacuum ( $\sim 10^{-9}$  torr). First, a LaB<sub>6</sub> filament expels electrons into an electron monochromator. In the monochromator, only certain energies of electrons are allowed to pass through. The electrons will then go through an electron lens where they can be focused. Once focused, the electron beam will cross with a molecular beam and the electrons will interact with the biomolecules. The ionic molecular fragments will enter a mass spectrometer where their mass/charge selection and energy dependence of a particular fragmentation process can be detected.

### **The Electron Monochromator**

In order to be able to study the effects of the LEEs on different biomolecules, the development of a focused and high resolution electron beam is necessary. The initial energy of the electron can be determined by the difference between the electric potential at the filament and the electrical potential at the interaction region. The electrons pass through electron lenses at different potentials  $A_1$ ,  $A_2$ , and  $A_3$  (Fig. 1). These lenses are used to prevent the divergence of the beam before it passes through the monochromator. The monochromator filters the electrons to reduce the energy spread around the desired energy. Electrons of certain energies are allowed

to pass through a half torus. The half torus uses two electrodes at different electric potentials to create a potential difference inside the monochromator (Fig. 1). This potential difference is what allows the electrons to pass through if they are at a certain velocity range. The monochromator has disadvantage that must be accounted for. Although it does act as a filter for electrons of certain energy, the electron flux of the beam will be affected severely from before the passage of the monochromator to after the monochromator. The reduction of the amount of the electrons is on the order of  $\sim 100$  to  $\sim 1000$ .

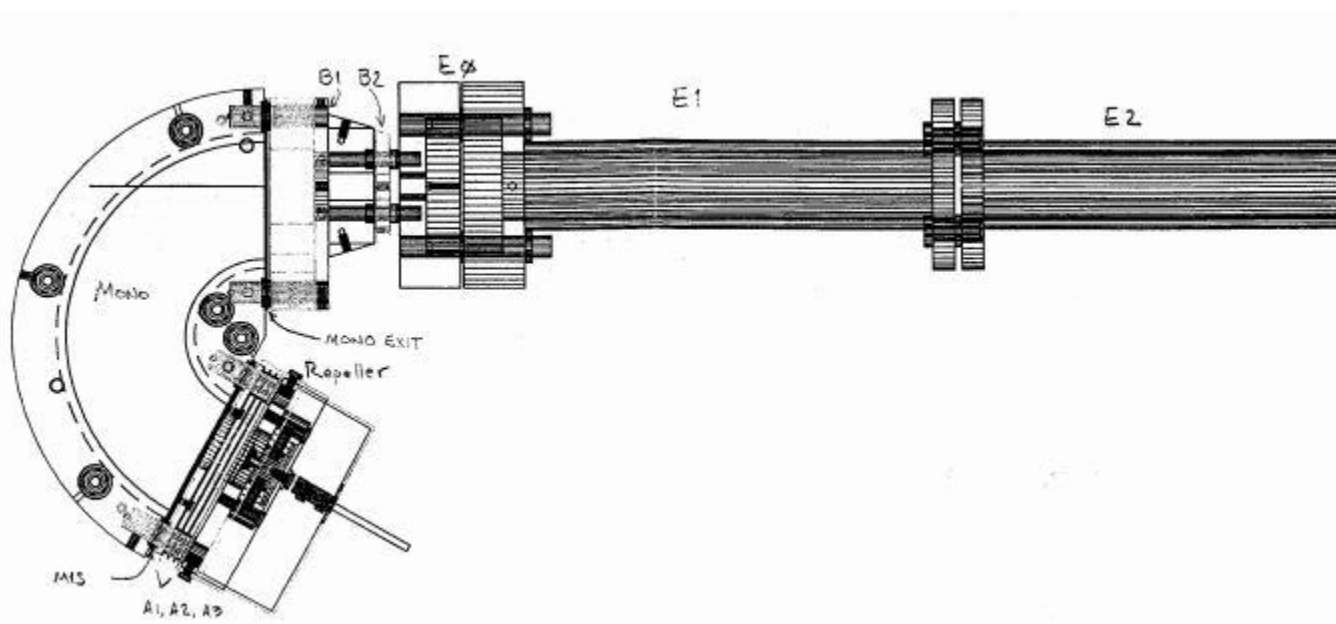


Figure 1. The schematic from [3] shows the filament, the monochromator, and electron lenses.  $E_1$  and  $E_2$  are the electrodes primarily used to focus the beam on the target sample.

### Electron Lenses and the Electron Beam

After passing the monochromator, the electron beam must be focused in order to get optimal number of interactions with the target molecules. This can be done using another set of electrostatic lenses. In the lenses for the experiment,  $E_1$  is horizontally split, for vertical steering of the beam and  $E_2$  is vertically split, to allow horizontal steering of the beam. Varying the voltages in the electrode can focus electron beams with different energies (Table 1). The

electrostatic lenses consist of a set of cylindrical electrodes with different voltages applied. The different voltages induce the electric field that act as the lenses [4]. The electrostatic lenses act very similar to optical lenses. For electrostatic lenses, there is an analogous Snell's Law and focal point definition, with energy as the important parameter.

Table 1, Figures 2-3 were all derived from the simulations (Fig. 4) using the program SIMION [5]. A focal point of 15 cm is chosen for the simulations; due to the fact the target sample is located 15 cm away from the end of  $E_2$ .

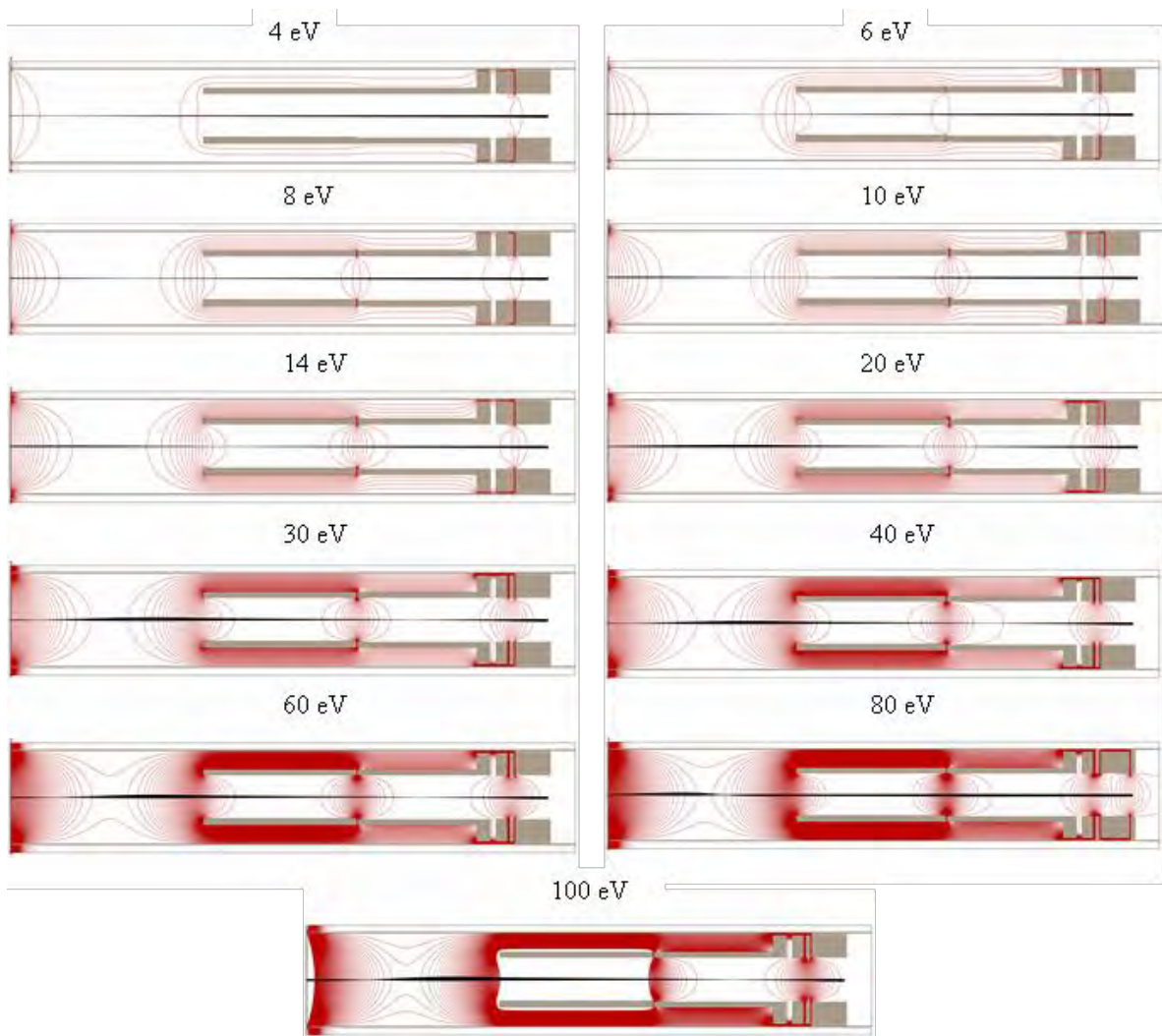


Figure 4. Simulation of the electron beam with different energies, ranging from 4 eV to 100 eV. The black lines show the paths of the incoming electrons, and the red lines represent the equipotential surfaces. The electrodes used in the simulation are  $B_1$ ,  $B_2$ ,  $E_0$ ,  $E_1$ , and  $E_2$ .

$E_0$ (eV)	$U_1$ (V)	Diameter (mm)
4	0.85	0.450
6	1.90	0.141
8	2.87	0.107
10	4.05	0.171
14	6.01	0.143
20	9.07	0.032
30	14.80	0.154
40	19.24	0.026
60	30.05	0.134
80	41.33	0.183
100	52.28	0.098

Table 1. The table shows the varying electric potentials on the electrode,  $E_1$ , needed to focus the electron beam, and the diameter of the beam for various energies. These values were obtained at the focal point of 15 cm from the end of  $E_2$ .

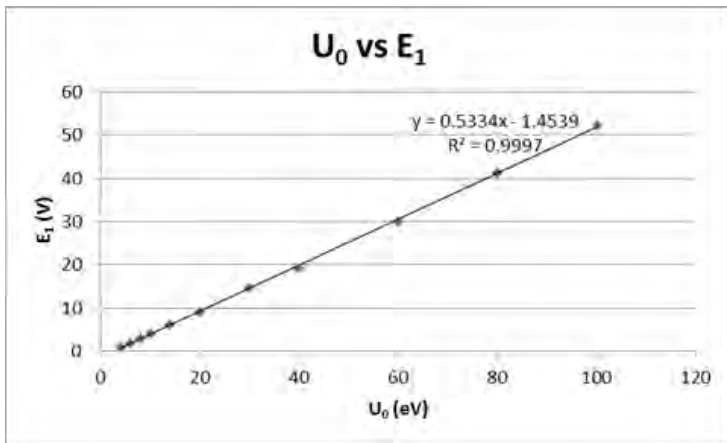


Figure 2. Linear relationship between the energy of the beam and the electric potential required to focus

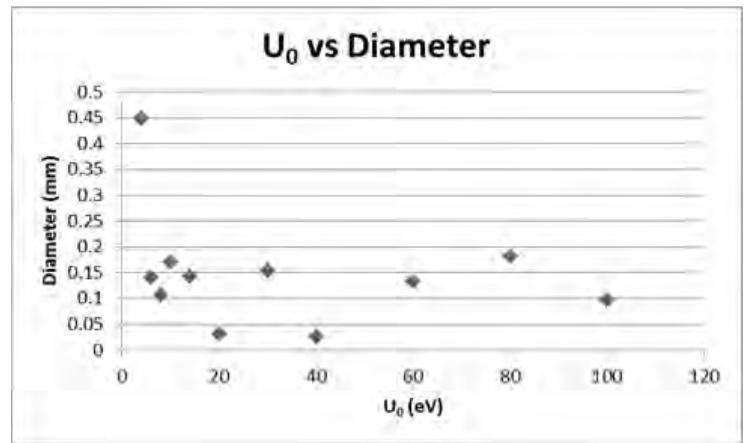


Figure 3. Diameter of the beam at 15 cm as a function of energy.

### Magnetic Field Control

Due to the low energies present for the electron, the beam is susceptible to the influence of external magnetic fields. The effect of the field can have a significant impact on the path of the beam via the Lorentz Force. Magnetic field control can be utilized by the use of a magnetic shield (Fig. 5) and/or the use of Helmholtz coils (Fig. 6).

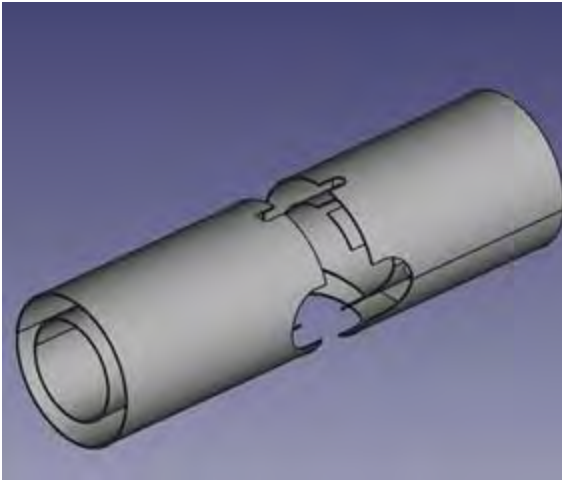


Figure 5. The magnetic shield is composed of two cylinders of Mu-Metal. The high permeability of the Mu-Metal allow for better shielding of external fields.



Figure 6. These are sets of square Helmholtz coils. The lengths of these are 22 in., 24 in., and 26 in. respectively.

Magnetic shielding aids in magnetic field control by redirecting the external field away from the shielded items [6]. The effectiveness of the shield can be measured by its attenuation factor. A higher attenuation factor yields to less external magnetic influence inside of the shield. The definition of the attenuation factor is the ratio of the strength of the field with the shield to the strength without the shield [4]:

$$A \equiv \frac{H_s}{H_0}$$

Using the definition with the equation for the attenuation factor of a cylinder and the equation for a two cylinder shield,

$$A = \frac{\mu t}{d}$$

$$A = A_1 A_2 \frac{2\Delta}{\bar{R}}$$

, where  $\mu$  is the relative permeability,  $t$  is the thickness,  $d$  is the diameter,  $\Delta$  is the distance between the shields, and  $\bar{R}$  is the mean radius of the two shields. The design of the shield has an inner radius of 31 mm, outer radius of 44.5 mm, and thickness for both shields of 1 mm. For Mu-Metal the relative permeability can vary depending on the external field to be shielded. Because

the Earth's magnetic field has a range from 0.30 Gauss to 0.65 Gauss [7] [8], the varying permeability gives an approximate range for the total attenuation factor of  $4.67 \cdot 10^5 < A < 1.30 \cdot 10^6$ . Using these ranges, it is possible to find the deflection of the electron beam using the Lorentz force and Centripetal force (Fig. 7).

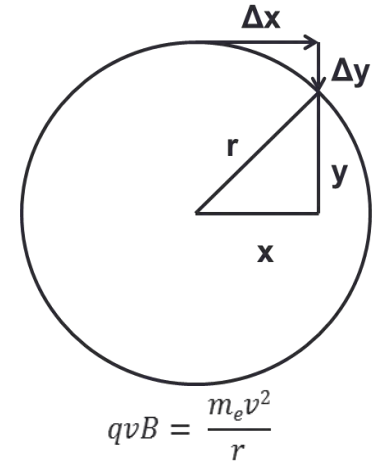


Figure 7. Using the parameters above, the deflection,  $\Delta y$ , of the beam can be calculated.

Deflection without Shield			
0.300 Gauss			
Energy (eV)	1	10	100
Radius (mm)	112.42	355.49	1,124.03
$\Delta y$ (mm)	$r < \Delta x$	33.17	10.05
0.650 Gauss			
Energy (eV)	1	10	100
Radius (mm)	51.89	164.07	518.87
$\Delta y$ (mm)	$r < \Delta x$	97.59	22.15

Table 2. The table shows the deflection of the beam without a shield.

Deflection with Shield			
0.0193 Gauss			
Energy (eV)	1	10	100
Radius (mm)	1,747.50	5,525.68	17,475.03
$\Delta y$ (mm)	6.45	2.04	0.64
0.0250 Gauss			
Energy (eV)	1	10	100
Radius (mm)	1,349.07	4,265.83	13,490.73
$\Delta y$ (mm)	8.46	2.64	0.83

Table 3. The table shows the shielded beam's deflection.

The Helmholtz coils are used for magnetic field control by producing a magnetic field opposite to the offending external field. Production of the opposite field is accomplished by allowing current to flow through copper wire wrapped around aluminum frames. The magnitude of the field in the center of a set of square coils can be approximated by [9]:

$$B(0) \approx \frac{4\mu_0 NI}{1.2965\pi\sqrt{2.2965}a}$$

In the equation,  $\mu_0$  is the permeability of free space,  $N$  is the number of turns,  $I$  is the current, and  $a$  is half of the length of the side. Using  $N=8$ , the values for the magnetic field can be derived with a changing current (Table 4).

Magnetic Field ( $\mu\text{T}$ ) for 22 in., 24 in., and 26 in. Frames			
Current (A)	22 in. Frame	24 in. Frame	26 in. Frame
1	23.32	21.37	19.73
2	46.63	42.75	39.46
3	69.95	64.12	59.18
4	93.27	85.50	78.92
5	116.59	106.87	98.65

Table 4. The magnetic field produced by the Helmholtz coils is of the order of the Earth's magnetic field (30  $\mu\text{T}$  to 65  $\mu\text{T}$ ). This means the coils will be able to reduce the influence of the Earth's magnetic field inside the apparatus sufficiently.

## Conclusion

To better understand the damage induced by LEEs, the importance of a LEE beam is necessary. One quality of this beam is a high energy resolution, meaning a low energy spread. The use of an electron monochromator, as well as the electron lenses, is beneficial to gain this quality in the beam. The focusing of the electron beam through the use of electrostatic lenses helps in attaining an optimal overlap between the electron beam and the target beam in the experiment. Due to the low energies present, sufficient magnetic field control is essential to the optimization of the experiment. Through the knowledge attained through the low-energy electron interactions with various biomolecules, beneficial uses for the fields of medicine and biophysics.

## Acknowledgements

This work was supported by the National Science Foundation through the Notre Dame REU Program. I would like to thank Dr. Sylwia Ptasińska for giving me the opportunity to work in her research group, Dr. Aleksandar Milosavljević, for teaching me new concepts to better understand the experimental project, and Brendan Jones, whom I worked with a lot throughout my research experience. I would like to thank Dr. Umesh Garg for this great summer research experience.

## References

- [1] Boudaïffa, B., Cloutier, P., Hunting, D., Huels, M., and Sanche, L. (2000). Resonant Formation of DNA Strand Breaks by Low-Energy (3 to 20 eV) Electrons. *Science*, 1658-1660.
- [2] Dawley, M.M., and Ptasińska, S. (2013). Dissociative electron attachment to gas-phase N-methylformamide. *International Journal of Mass Spectrometry*, 365-366, 143-151.
- [3] LK Technologies, Inc. (2014). *LK1000M Manual*. Bloomington, IN.
- [4] Moore, J., Davis, C., Coplan, M., and Greer, S. (2009). *Building scientific apparatus* (4th ed.). Cambridge, UK, Cambridge University Press.
- [5] SIMION® Version 8.1. (n.d.). Retrieved July 29, 2015, from <http://simion.com/>
- [6] How Do Magnetic Shields Work? (n.d.) Retrieved June 15, 2015, from [http://www.magnetic-shield.com/pdf/how\\_do\\_magnetic\\_shields\\_work.pdf](http://www.magnetic-shield.com/pdf/how_do_magnetic_shields_work.pdf)
- [7] Magnetic Field of the Earth. (n.d.). Retrieved June 15, 2015, from <http://hyperphysics.phy-astr.gsu.edu/hbase/magnetic/magearth.html>
- [8] Earth's magnetic field. (n.d.). Retrieved June 15, 2015, from [https://en.wikipedia.org/wiki/Earth's\\_magnetic\\_field](https://en.wikipedia.org/wiki/Earth's_magnetic_field)
- [9] Restrepo-Alvarez, A., Franco-Mejia, E., and Pinedo-Jaramillo, C. (2012). Study and analysis of magnetic field homogeneity of square and circular Helmholtz coil pairs: A Taylor series approximation. *Andean Region International Conference (ANDESCON), 2012 VI*, 77-80.

# Experimental investigation of the repelling force from RF carpets

Alec Hamaker

2015 NSF/REU Program

Physics Department, University of Notre Dame

Advisor: Professor Maxime Brodeur

## Abstract

The theoretical description for transporting ions in a helium buffer gas using a radio-frequency carpet was proposed earlier [1]. Using this description, the maximal repelling force created by the RF carpet could be calculated in terms of parameters that can be measured in the lab. This equation was experimentally tested at different values for the amplitude of the RF carpet, the pressure of the helium gas in the chamber, and the electric push field that the RF carpet is counteracting. The experimental conditions were also simulated with the inclusion of hard-sphere collisions. When comparing the effect on the repelling force of varying the RF amplitude to simulations, we observed a difference that could possibly be explained if the ion motion of each ion is simulated for a longer time. When comparing the effect of varying pressure, we noticed a large difference between the theoretical description and the experimental data. Simulations will have to be performed to explain this difference.

## 1. Introduction

With the recent growth of radioactive ion beam facilities worldwide including the Facility for Rare Isotope Beams (FRIB) at Michigan State University, there is a high potential for answering questions ranging from the creation of heavy nuclei to the structure of exotic nuclei. However, the produced beams at FRIB will have high energy and momentum spreads which are at odds with low energy experiments such as high precision mass measurements. Luckily, the development of gas cells has bridged the gap. There are currently two main methods for transporting ions in gas cells: the traditional method, for which a static electric potential of decreasing strength is applied on individual electrodes, forming a so-called RF carpet, and the ion surfing method, which replaces this potential by

a traveling wave. The common feature of both methods is the application of a radio-frequency (RF) on the carpet electrodes to provide a repelling force. The ion motion above the carpet and the stability conditions for that motion were investigated leading to a theoretical description of the maximal force on an ion that an RF carpet can balance [1].

In both situations, a detailed knowledge of the parameters that lead to a maximized repelling force is desirable. Hence, considering the growing use of RF carpet technology, we decided to investigate experimentally the behavior of the repelling force as a function of various experimental parameters. In this paper, we report on the results for various values of the RF amplitude and the pressure inside the gas cell.

## 2. Theoretical Description

An RF carpet is made of a series of closely spaced electrodes with a  $180^\circ$  phase shift between adjacent electrodes on which an alternating potential is applied (see Figure 1). The resulting electric field creates a repelling force above the electrodes. To keep the ions hovering just above the RF carpet, a “push” force is used to balance the repelling force from the RF.

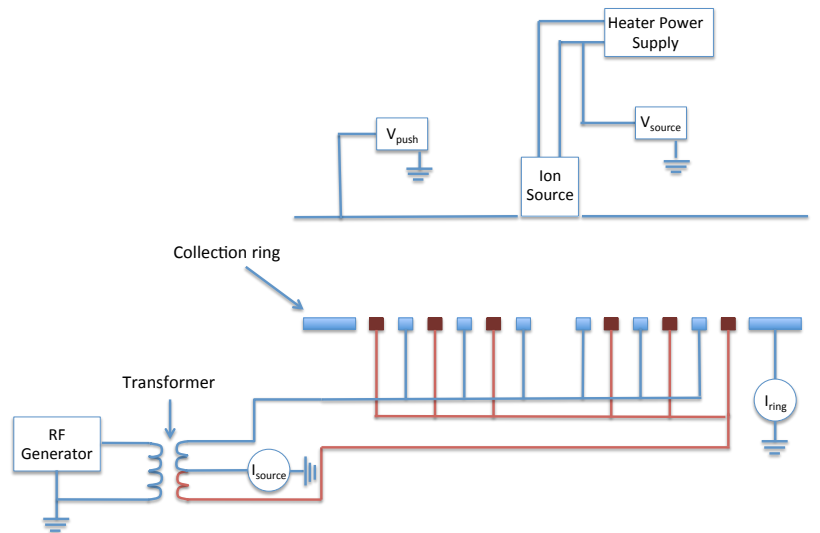


Figure 1. Image of experimental design. The dark and light squares denote the alternating electrodes and the opposite RF phases.

Recently, a theoretical description for the ion motion on the surface of a RF carpet was proposed [1]. This description presented an equation for the maximal repelling force that can be created by an RF carpet when all stability conditions for the ion motion are met.

Since the push force must balance the repelling force, we can determine the maximal electric push force and thus push field:

$$E_{push}(\max) = \frac{m \cdot 4\pi a f^2}{q} \left( 1 - 1.09 \sqrt{\frac{a^2 f}{2VK_0} \frac{p/p_0}{T/T_0} \frac{1}{\text{sinc}(\pi\gamma/2)}} \right). \quad (1)$$

Here,  $a$  is the center-to-center distance between electrodes, also known as the carpet pitch,  $\gamma$  is the ratio of the gap between adjacent electrodes to their pitch,  $f$  is the RF frequency,  $V$  is the RF amplitude,  $m$  is the ion mass,  $p$  is the gas pressure,  $T$  is the gas temperature, with  $p_0 = 1013.25$  mbar and  $T_0 = 273.15$  K,  $q$  is the charge of the ion, and  $K_0$  is the reduced ion mobility in helium.

### 3. Experimental set-up

The experimental set up included an RF carpet, a stainless steel plate to provide the push field, and an ion source (see Figure 2), which were all placed inside a vacuum chamber. The circuitry used to create the RF, the push field, the ion source power supply, and the RF supplies along with the measuring devices were placed outside the vacuum chamber.

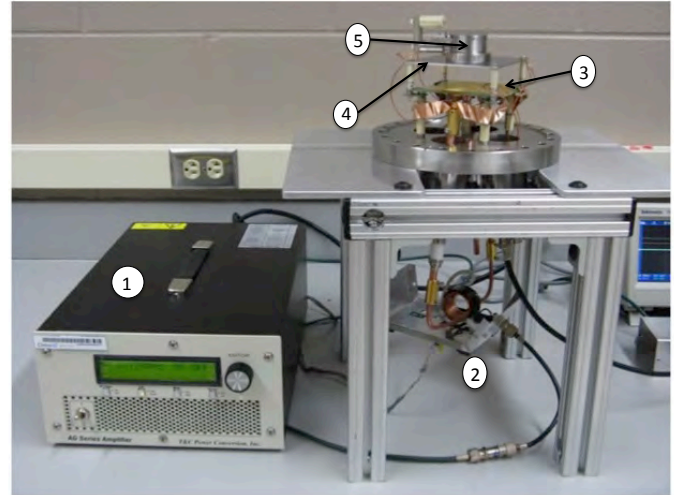


Figure 2. Photograph of the RF carpet and the circuitry on a holding frame for tuning. (1) is the RF generator. (2) is the RF circuit with the air core impedance matching transformer. (3) is the RF carpet. (4) is the stainless steel push plate (5) is the ion source.

The vacuum chamber was evacuated with a scroll pump and a turbo molecular pump (300 L/s) in order to minimize residual air contamination of the helium within the chamber. The system was pumped down to a base pressure in the  $10^{-9}$  mbar range between measurements. During the measurements, grade 5 ultra-pure helium was used. The gas

pressure was monitored using three different gauges: a convection gauge when pumping down the system, a hot cathode gauge at ultra high vacuum conditions, and a baratron gauge for a precise absolute pressure reading during the measurements. A

thermocouple was also used to measure the temperature inside the chamber (see Figure 4). In order to

avoid RF or DC discharges in the chamber, the RF amplitude was kept below 75 V. See Figure 3 for a photograph of the experimental set-up.

The circuitry used to operate the RF carpet was constructed to maximize the RF frequency on the carpet and maintain a stable RF amplitude. In order to maximize the transfer of power from the generator to the carpet, the RF generator signal was impedance matched using an air core impedance matching transformer (see Figure 2). The transformer was made of a single turn of 2 cm wide and 4 cm diameter copper tube while the primary was made of 9 turnings of 14 gauge copper wire. To minimize resistive losses, only copper was used to carry the RF in the circuitry.

Applying a positive potential on a stainless steel plate produced the push field  $E_{push}$  used to bring the ions close to

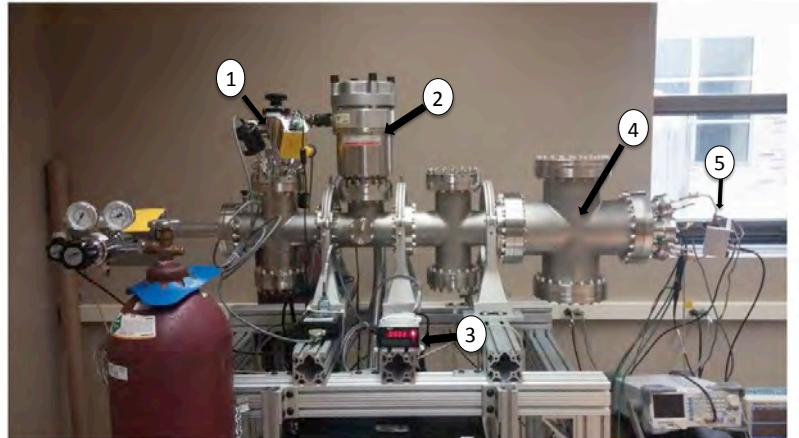


Figure 3. Photograph of the experimental set-up. (1) is the hot cathode gauge, (2) the turbo molecular pump, (3) the baratron gauge controller, (4) the vacuum chamber where the RF is set up, and (5) the RF circuitry.

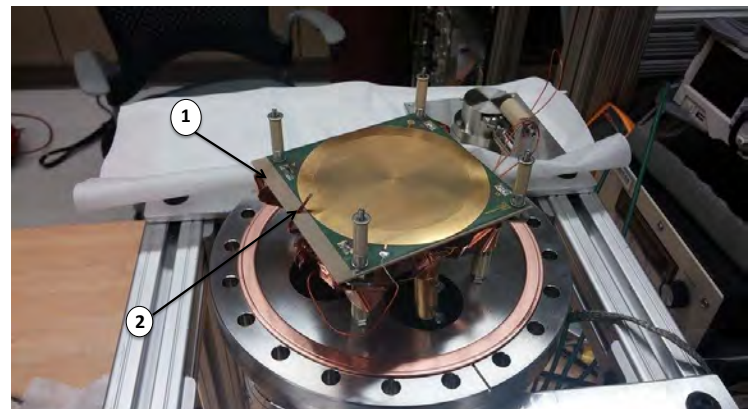


Figure 4. Image of the RF carpet after the installation of the PEEK (1) and the thermocouple (2).

the carpet surface. The commercial surface ion source used during the experiment was created by HeatWave Labs [2]. A sheet of PEEK 1/16" thick was placed under the RF carpet in order to prevent the carpet from flexing (refer to Figure 4). The carpet pitch was 0.16 mm, and the gap between adjacent electrodes was 0.08 mm resulting in a gap-to-pitch ratio  $\gamma$  of 0.5. The distance between the plate and the RF carpet was 2.8 cm.

The heater current for the ion source was provided by a 60 V, 9 A DC power supply. The resulting ion current produced  $I_{source}$  could be measured off the carpet through the center tap of the secondary part of the transformer while the RF was turned off.

The ions produced were focused and directed toward the RF carpet with a lens electrode biased at a lower potential  $V_{push}$  than the potential at the ion source  $V_{source}$ . The RF carpet was set up in such a way as to carry the ions to a collection ring located on the edge of the carpet when the RF was applied. Here another current could be measured  $I_{ring}$  (refer to Figure 1). Both currents ( $I_{source}$  and  $I_{ring}$ ) were measured using an electrometer, which was connected to a switch that could be flipped to measure the desired current.

#### 4. Measurement method

Because the maximal repelling force created by the RF carpet is equal to the maximal push force when the ion is hovering just above the carpet, we could

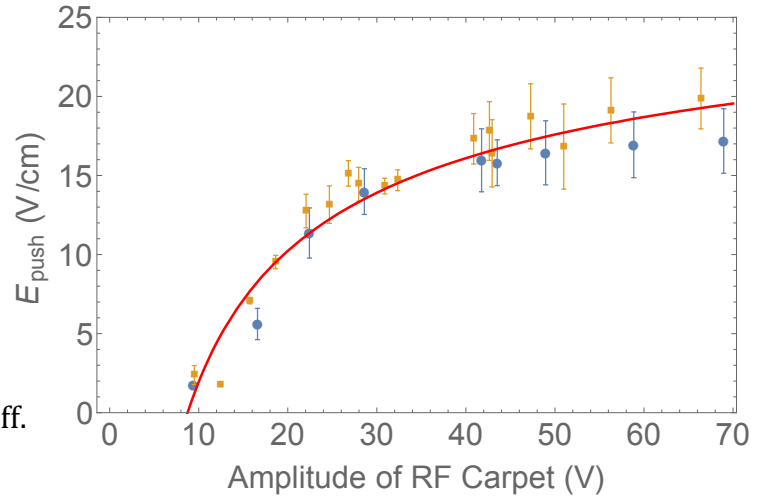


Figure 5. The squares denote measurements taken before the thermocouple was installed. The circles denote measurements taken after the thermocouple was installed. There is on average a 13% difference between the two sets of measurements.

experimentally investigate equation (1). This was to our advantage as we could determine the push field from

$$E_{push} = \frac{V_{push}}{d}, \quad (2)$$

where  $d = 2.8$  cm is the distance between the steel plate and the RF carpet.

Equation (1) was tested by measuring the fraction of the ion beam that diffused across the carpet under various conditions. This is because without the application of a traveling wave or a potential gradient, as long

as the push field is not too strong, the ions will make their way to the outer edge of the carpet through a random walk. The parameters varied were: the gas pressure  $p$ , the push field strength  $E_{push}$ , and the RF

amplitude  $V$ . In order to make proper measurements, an  $I_{source}$  current of 100 pA was chosen to minimize possible effects

due to space charge while having sufficient current for a precise measurement, and  $60^\circ$  C was the measured temperature where a 100 pA current was readily produced. Once the desired  $I_{source}$  and  $T$  were achieved, measurements could be recorded. Starting with  $V_{push}$  at approximately 10 V, a measurement of  $I_{source}$  was recorded. Then, the RF was turned on and a measurement was recorded for  $I_{ring}$ . The RF was turned off again, and another measurement of  $I_{source}$  was recorded to insure there was no fluctuation in the source current while  $I_{ring}$  was recorded. Next,  $V_{push}$  was increased by 10 V and  $V_{source}$  was

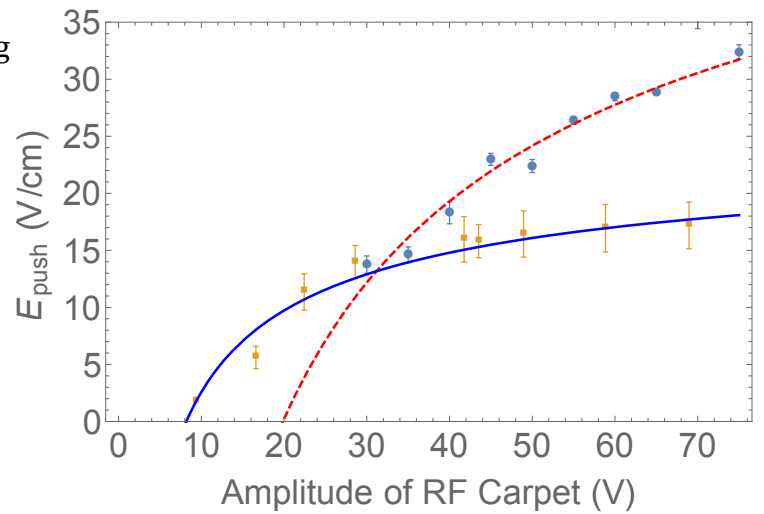


Figure 6. The plot contains data expressing the maximal push field at 50% survival fraction versus the amplitude of the RF carpet. The solid curve with square points represents the experimental data. The dashed curve with circular points represents the simulation data.

increased in order to achieve the specific value for  $I_{source}$ . The process of recording  $I_{source}$  and  $I_{ring}$  was repeated again. This process was continued until  $I_{ring}$  was less than or equal to 5 pA. The currents would typically fluctuate by 2 pA or less.

The process was repeated for different pressures in the chamber and different values for the RF carpet amplitude. The quantity of interest calculated after the measurements was the ion survival fraction which was given by:

$$\epsilon = \frac{I_{ring}}{I_{source}}. \quad (3)$$

## 5. Results

The primary goal of the investigation was to experimentally test equation (1) at different values for the gas pressure  $p$  and the RF amplitude  $V$ . Since an unambiguous measurement of  $E_{push}(\text{max})$  would be difficult, we instead determined the  $E_{push}$  value at a survival fraction of half the maximum survival fraction recorded for a particular RF amplitude value or gas pressure value, and then plotted this data to see if it followed the form of equation (1). The measurements were performed at pressures from 20 mbar to 200 mbar at 20 mbar intervals, with push fields ranging from  $\sim 1$  V/cm to  $\sim 20$  V/cm, RF frequencies of 6.80 MHz, 6.81 MHz and 6.89 MHz, and RF amplitudes ranging from  $\sim 9$  V to  $\sim 66$  V.

### A. Push field vs. amplitude of RF carpet

The thermocouple used to measure the temperature was installed approximately half way through the measurements of different RF carpet amplitude values, so the circuit had to be re-tuned, and the frequency had to be adjusted from 6.89 MHz to 6.81 MHz. Measurements at different RF amplitudes were recorded between two and five times before the thermocouple was installed and six and nine times after the thermocouple was

installed. As one can see in figure 5, there is only a small difference between the two data sets (average percent difference ~13%).

The data plotted in figures 5 and 6 are of push field values when the survival fraction was at 50% of the maximum survival fraction measured for each RF amplitude.

Hence curves used to fit the data are

$$y = a \left( 1 - 1.09 \cdot \sqrt{\frac{b}{x}} \right)$$

where  $a$  and  $b$  are constants.

Simulations of the experiment were

also performed using the IonCool code

[3]. Figure 6 contains experimental data and simulation data. Although the experimental and simulation data

follow the form of equation (1), they are quite different from each other. This difference appears to be due to the value of the maximum time we let the ion hover before

terminating the simulation (maximum time of flight =  $2 \times 10^{-2}$  s) in the IonCool code. We

are now in the process of trying different values for the maximum time of flight to see if one more closely matches the experimental data (see Figure 7).

### B. Push field vs. pressure of helium gas

Measurements at different pressures were recorded between four and sixteen times. The data plotted in Figure 8 is of push field values when the survival fraction was at 50% of the maximum survival fraction measured for each pressure versus the pressure in the gas chamber. The fitted curve is of the form  $y = a(1 - 1.09 \cdot \sqrt{b \cdot x})$  where  $a$  and  $b$  are

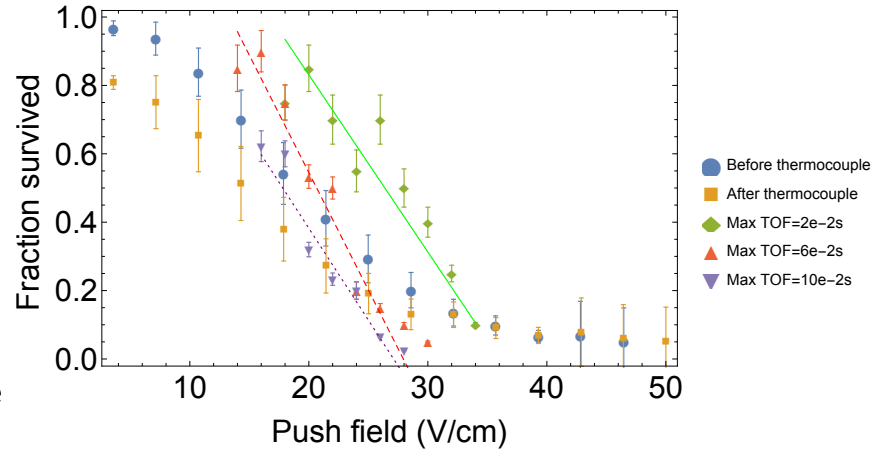


Figure 7. The solid line represents Max TOF=2e-2s. The dashed line represents Max TOF=6e-2s. The dotted line represents Max TOF=10e-2s. It appears that a Max TOF=10e-2s most closely matches the experimental data.

constants. Note that from 20 mbar to 120 mbar, the push field is increasing. This is in contrast to the decreasing push field that is expected from equation (1) for varying pressure. It is not until 120 mbar is reached that the data begins to follow the form of equation (1). This has led us to believe that there might be other factors involved when one reaches lower pressures that equation (1) does not take into account. Simulation data is needed to see if the experimental data is expected.

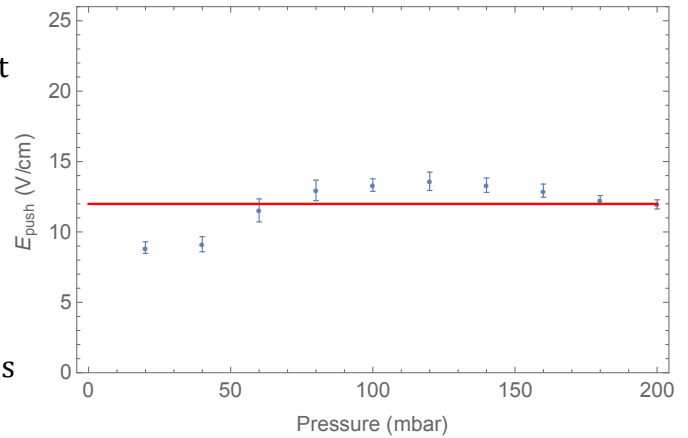


Figure 8. The fitted curve is of the same form as equation 2.

## 6. Conclusion

An experimental test of equation (1) was presented for varying RF amplitude and pressure. Simulations of the experiments were also performed. By comparing the experimental data to simulation in the case of varying RF amplitude, one finds a substantial difference between the two. When studying the varying pressure, the data does not seem to follow the form of equation (1). Additional simulations and data may need to be collected in order to see if there is another factor causing the odd form of the varying pressure data. Further tests of equation (1) could be performed with different carpet pitches or with different frequencies using different masses.

## 7. References

- [1] S. Schwarz, Int. J of Mass Spec. **299**, 71 (2011).
- [2] <http://www.cathode.com/>
- [3] S. Schwarz, Nucl. Instr. And Meth. A **S66**, 233 (2006).

Properties of Carbon-Enhanced Metal-Poor Stars:  
On the Bi-modality of Carbon Abundances

Siyu He

2015 NSF/REU Program  
Department of Physics, University of Notre Dame

Advisors: Prof. Beers  
Prof. Placco  
Prof. Carollo

## Abstract

One of the most important topics in astronomy is the study of chemical evolution in galaxies. Metal-poor stars play a significant role in this subject. They are stellar fossils, and reveal important information on the nature of the early Universe. A significant fraction of metal-poor stars in the Milky Way is enhanced in carbon (carbon-enhanced metal-poor – CEMP – stars). Recently, by using stars with high resolution spectroscopy, (Spite et al., 2013) identified a bimodality in the carbon abundance ( $A(C)$ ) distribution, which is directly connected to the stellar progenitors of such old stars. In this report I have investigated this bi-modality by using a sample of stars with high-resolution spectroscopy available ( $R \approx 35,000$ ) and another sample with medium-resolution spectroscopy ( $R \approx 2,000$ ) available. Most stars in the high carbon abundance plateau belong to CEMP-s/rs (stars enriched in neutron capture process elements), whereas in the low carbon band the majority are CEMP-no (stars with low neutron capture elements abundance). These two classes of CEMP stars (CEMP-s/rs and CEMP-no) can be classified in high-resolution spectroscopy data, while is not possible to make a distinction at medium-resolution. In high-resolution spectroscopy, the carbon abundances are derived mainly from the CH G-band at  $4300 \text{ \AA}$ . For medium-resolution spectroscopy, we removed stars with  $T_{\text{eff}} > 6000 \text{ K}$  and giants stars with surface gravity  $\log g > 2.5$ , because the pipeline used to derive the carbon abundances would provide wrong estimates. We have confirmed that the two carbon bands can also be recognized with medium-resolution spectroscopy in the  $A(C)$  vs. metallicity diagram and by performing Gaussian fitting of the carbon abundance distribution. This is a very important result because we can now separate CEMP-s/rs and CEMP-no by using medium-resolution spectroscopy only. A new data-driven approach to getting stellar label called Cannon is also investigated in the further perspective section of this report and preliminary results are presented.

# 1 Introduction

## 1.1 Metal-Poor stars

Today it's widely recognized that **fossil** stars in Galaxy can include many information about the early Universe, which is described as near-field cosmology (Freeman & Bland-Hawthorn, 2002), especially **those** stars where atmospheric abundances of the heavy elements (all elements heavier than lithium) are substantially lower than the solar content (Beers & Christlieb, 2005). **These stars provide fundamental information on numerous issues of contemporary interest in astronomy, including how to explain the element production from supernovae explosion, understand the nature of the first stars, and shed light on the nature and evolution of early universe** (Beers & Christlieb, 2005).

The abundance of one element with respect to another is often compared with the solar value. The notation is:  $[A/B] \equiv \log_{10}(N_A/N_B)_* - \log_{10}(N_A/N_B)_\odot$  ( $N_A$  and  $N_B$  refer to the numbers of atoms of elements A and B). Metal-poor stars can be classified by adopting the following definition (Beers & Christlieb, 2005):

[Fe/H]	Term	Acronym
>+0.5	Super metal-rich	SMR
0.0	Solar	-
<-1.0	Metal-poor	MP
<-2.0	Very metal-poor	VMP
<-3.0	Extremely metal-poor	EMP
<-4.0	Ultra metal-poor	UMP
<-5.0	Hyper metal-poor	HMP
<-6.0	Mega metal-poor	MMP

Table 1: Definition of Metal-poor Stars

Metal-poor stars mostly possess low mass and evolve extremely slowly, **therefore they can be as old as the earliest stellar generations** ( $\sim 400$  million years after the Big Bang). They are located in the halo system and the bulge of the Milky Way.

## 1.2 Carbon-enhanced Metal-Poor Stars

One important class of metal-poor stars are those with high carbon abundance. These stars are called carbon-enhanced metal-poor (CEMP) stars. Metal-poor stars are defined CEMP when their carbon-on-iron abundance is  $[C/Fe] \geq +0.7$ . CEMP stars are very common at low metallicity (Schneider et al., 2012). Recent investigations on CEMP stars indicated the existence of a bimodal distribution of carbon abundance when we look at the high resolution data, especially in the VMP regime (Bonifacio et al., 2015). We have investigated such bi-modality by exploring a sample high resolution data and confirmed that the same bi-modal pattern can be recognized in medium-resolution data.

## 1.3 CEMP-no and CEMP-s stars

An important class of CEMP stars possess high value of heavy elements produced in neutron-capture process, such as Strontium and Barium. These are called CEMP-s or CEMP-rs. On the contrary, metal-poor stars with low content of slow neutron capture process elements are called CEMP-no stars. Their definition is reported in Beers & Christlieb (2005) and summarized below.

Acronyms	Definitions
CEMP	$[C/Fe] \geq +0.7$
CEMP-s/rs	$[C/Fe] > +0.7$ and $[Ba/Fe] \geq +1.0$
CEMP-no	$[C/Fe] > +0.7$ and $[Ba/Fe] < = 0.0$

Table 2: Definition of CEMP Stars

Some CEMP stars with normal pattern heavy elements are called CEMP-no stars. CEMP-s stars are enriched in heavy elements produced in the s-process neutron capture (*s* stands as slow) while the CEMP-rs stars are enriched by both slow and rapid neutron capture process elements (*r* stands as rapid). The progenitor of CEMP-rs are likely low mass stars in binary systems and they get polluted of carbon and neutron-capture process elements through the mass transfer from a companion during its the AGB phase. In case of the CEMP-no stars the progenitors are likely to

be faint supernovae and massive fast rotating stars (Bonifacio et al., 2015). The CEMP-no stars are perhaps the most important objects to shed light on the chemical evolution and potentially provide a unique probe of the first mass function in the early universe (Hansen et al., 2015).

## 2 Dataset

Our sample contains 621 stars observed in high-resolution ( $R \approx 35,000$ ), selected from the literature. From these, 600 are in the  $-4 < [\text{Fe}/\text{H}] < -2$  range, and were selected by Placco et al. (2014). The remaining 21 stars were selected from Placco et al. (2015). 16 of these stars are UMP stars ( $[\text{Fe}/\text{H}] < -4$ ), and 4 are HMP stars ( $[\text{Fe}/\text{H}] < -5$ ). The MMP star ( $[\text{Fe}/\text{H}] < -6$ ) with  $[\text{Fe}/\text{H}] < -7.8$ , called SMSS J0310–6708 (Keller et al., 2014), is also included. We also have medium-resolution ( $R \approx 2,000$ ) data taken from the Sloan Digital Sky Survey (SDSS), and the total number of stars is 118454.

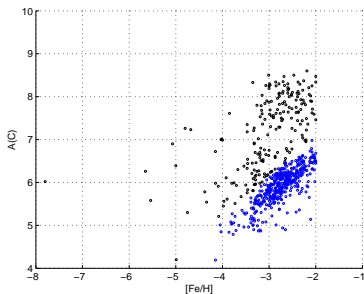


Figure 1: Absolute carbon distribution versus  $[\text{Fe}/\text{H}]$  of high resolution data

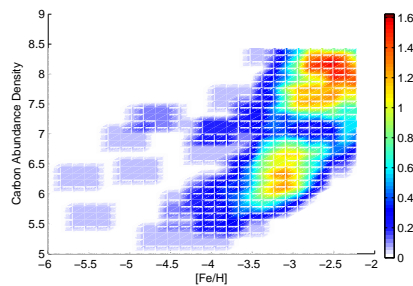


Figure 2: Carbon density distribution versus  $[\text{Fe}/\text{H}]$  of high resolution data

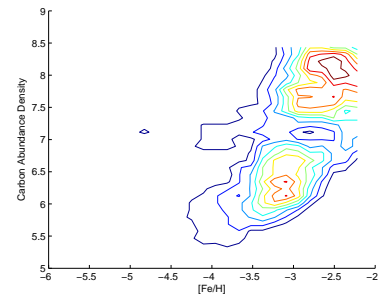


Figure 3: Carbon contour distribution versus  $[\text{Fe}/\text{H}]$  of high resolution data

## 3 Analysis

### 3.1 High-Resolution Data

In this section, we investigate the properties of the carbon abundance distribution ( $A(\text{C})$ ) for the dataset with high-resolution spectroscopy available. Figure 5 plots absolute  $A(\text{C})$  versus

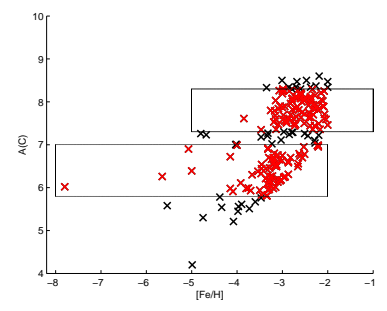
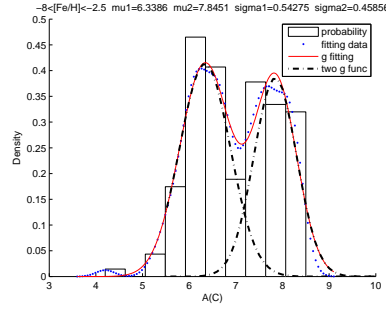
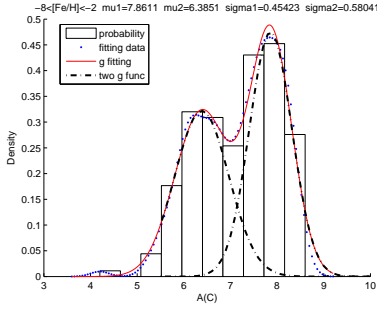


Figure 4: Density histogram and fitting of high resolution data

Figure 5: Density histogram and fitting of high resolution data

Figure 6: Carbon distribution versus  $[Fe/H]$  with boxes of high resolution data

metallicity. The absolute carbon abundance is derived by using the following expression:  $A(C) = [Fe/H] + [C/Fe] + 8.43$ . (8.43 represents solar absolute hydrogen abundance). In giant stars the presence of the CN molecule causes carbon depletion which can provide pseudo carbon values. Therefore we selected the corrected values of carbon-on-iron as reported in [Placco et al. \(2014\)](#). Figure 1, shows all the data. The range of  $[Fe/H]$  is from  $-7.8$  to  $-2$ . The black dots represent CEMP stars (206 stars), and blue dots are carbon-normal metal-poor (NMP) stars (415 stars), while Figure 2 shows the density plots of  $A(C)$  distribution versus metallicity for CEMP stars only. In this figure we can appreciate two separate areas of CEMP stars where the density is higher. The contour of density plot (Figure 3) shows the separation even better.

The two distinct features represent the bimodality in the CEMP stars population mentioned earlier. It can be noticed that the position of lower plateau is located at lower metallicities than the higher plateau. The density histogram of  $A(C)$  are plotted in figure 4 and figure 5 and are used to determine the median and  $\sigma$  of low and high bands. Figure 4 shows the density histogram for CEMP stars in the range of metallicity  $-8 < [Fe/H] < -2$ , and Figure 5 in the range  $-8 < [Fe/H] < -2.5$ . A Gaussian fit of the density histograms provide medians of 7.8 and 6.4 and dispersions of  $\sim 0.5$  and 0.6 for the high and low band, respectively. Figure 6 shows the CEMP stars and the two bands (red cross) derived with the Gaussian fitting (black rectangular areas). The upper box goes from  $A(C) = 7.3$  to  $A(C) = 8.3$ , while the lower box spans from 5.8 to 7.0. Figure 7 is similar to Figure 6, but we also include NMP stars (blue dots). The linear curve that

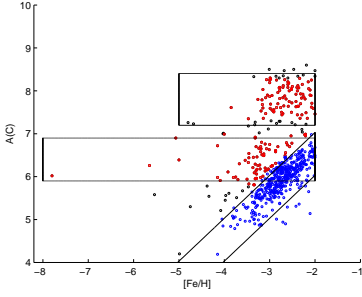


Figure 7: Carbon distribution versus  $[\text{Fe}/\text{H}]$  with boxes of high resolution data

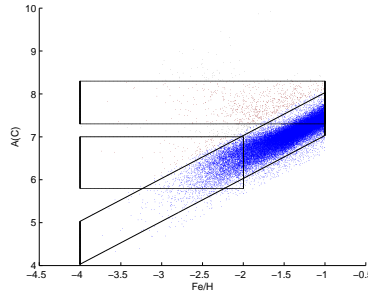


Figure 8: Carbon distribution versus  $[\text{Fe}/\text{H}]$  of medium resolution data

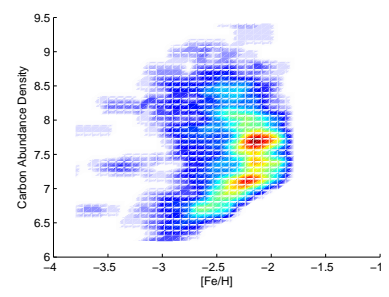


Figure 9: Carbon distribution density of medium resolution data

define the NMP area are obtained by assigning to  $[\text{C}/\text{Fe}]$  the value 0.6 and  $-0.4$ .

### 3.2 Medium-Resolution Data

In this section we investigate the behaviour of the medium resolution spectroscopy data basing on the results obtained with the high resolution spectroscopy data. Stars with  $T_{\text{eff}} > 6000\text{K}$  are removed because of incorrect estimation of the pipeline. Giants stars with  $\log g \leq 2.5$  are also removed because in medium resolution we cannot apply the correction to the carbon-on-iron estimates. The two rectangular boxes base on high-resolution have the following limits: high band from 7.3 to 8.3 and low band from 5.8 to 7.0. This exercise is very useful because the two bands overlap. Figure 8 shows  $A(\text{C})$  versus metallicity for the medium resolution data. The red dots represent the CEMP stars while the blue dots denote the carbon normal stars.

Figure 9 and 10 show the density and the contour plots for the medium resolution data. It is clear that the two plateaus are present and that the low band appears at the  $[\text{Fe}/\text{H}] \approx -2.3$ . Figure 11 shows a series of density histogram with different metallicity ranges with the Gaussian fitting. As the metallicity decreases the peak of the low band increases which is consistent with the expectation that at lower metallicity the low band should be the dominant component. At about  $[\text{Fe}/\text{H}] = -2.25$ , the  $A(\text{C})$  distribution split in two peaks and the dispersions. Note that the medians and dispersions of the last panel of Figure 11 are not included in Figure 12, because the number of stars in each bin was not statistically significant. Note that at low resolution the

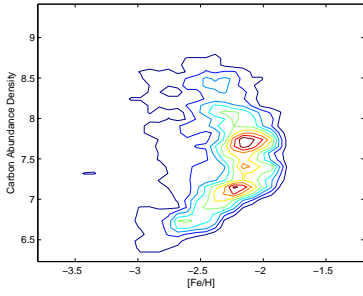


Figure 10: Carbon distribution contour of medium resolution data

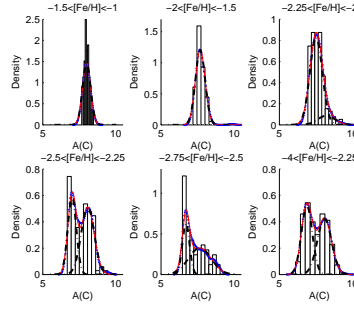


Figure 11: Density histogram and fitting of high resolution data

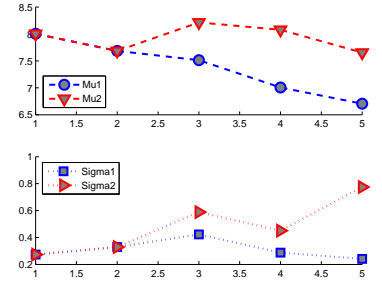


Figure 12: Median and sigma tendency of fitting of different metallicity range

peak of the low band is greater than the peak of the high band. This is due to the fact that we removed a large number of giant stars which reside in the high band. Figure 16 shows the trend of medians and dispersions of the Gaussian fitting functions.

## 4 Distinguishing CEMP-no and CEMP-s/rs

The above analysis can be applied to make a separation between the CEMP classes. We can verify that stars in the low carbon band are CEMP-no, while the high carbon band is populated by CEMP-s stars with some contamination from CEMP-no stars (identified from their Barium abundances on high-resolution spectroscopy, which is high in case of CEMP-s stars). Figure 13 shows  $A(C)$  as a function of the metallicity for the high-resolution spectroscopy dataset. The red symbols represent the CEMP-s/rs stars while the blue denote the CEMP-no stars. Most stars in high carbon band are CEMP-s/rs, whereas most of stars in low carbon band are CEMP-no, though contaminations exist. This properties of the  $A(C)$  vs metallicity plot can be used to separate CEMP-s and CEMP-no in case of medium resolution data, because the the majority of stars in the high band are indeed CEMP-s/rs and those in the low carbon band are CEMP-no stars. This technique can be used to select CEMP-s/rs and CEMP-no in medium-resolution data, but we should take into account that some contamination exist and further investigations need to be done. We also tried to use the Nitrogen abundance to explore a better separation

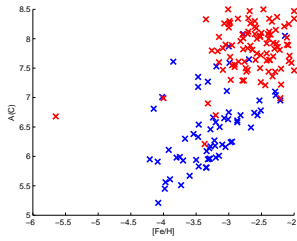


Figure 13: CEMP-no and CEMP-s/rs on carbon abundance distribution

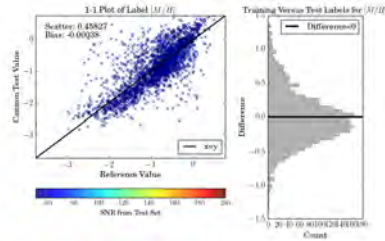


Figure 14: 1-1 diagnostic of metallicity of 2500 LAMOST data

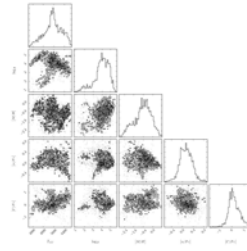


Figure 15: Triangle figure of labels of survey stars

between CEMP-s/rs and CEMP-no, however we didn't find a clear separation in the the  $A(C+N)$  vs metallicity diagram that could be used for this purpose.

## 5 Summary and Further Perspective

### 5.1 Summary

We have analysed two samples of stars, the first with high-resolution spectroscopy available and the second one with only medium-resolution available. By using the information contained in the absolute carbon abundance  $A(C)$  parameter as a function of the metallicity, we have demonstrated that even at medium-resolution the two classes of CEMP stars, CEMP-s and CEMP-no, can be distinguished. This is an important result with large potential application to any survey with medium-resolution spectroscopy available.

### 5.2 Further Perspective

New spectroscopic surveys provide the stellar physical parameters and abundances (stellar labels) but the calibrations varies with different surveys. This discrepancy can be solved by “The Cannon”, a data-driven approach for determining stellar labels from spectroscopic data (Ness et al., 2015). The Cannon employ some reference stars for which the labels are known and learn how the continuum-normalized spectra depend on these labels by fitting a flexible model at each

wavelength, then it uses this model to derive the labels for the stars we want to analyse.

For this exercise, we used 2500 stars from LAMOST (<http://www.lamost.org>) as reference objects and derived the stellar labels for these spectra by using the model learning in the Cannon. Preliminary results are showed in Figure 14 and Figure 15, which are not completely satisfactory. Additional work has to be done on both LAMOST data and The Cannon to improve the derivation of the labels.

## 6 Acknowledgement

I feel very appreciate for having such a God-given experience in University of Notre Dame. And it is so lucky to meet with my kind advisors, Prof. Beers, Prof. Placco, Prof. Carollo, who gave me much help all the summer. I not only opened my eyes to research astronomy from knowing nothing at the beginning, but also learned a lot of computing skills, such as Linux and Python. In addition, I am very thankful to Prof. Garg for giving me such a good opportunity.

## References

- Beers, T. C., & Christlieb, N. 2005, ARA&A, 43, 531
- Bonifacio, P., Caffau, E., Spite, M., et al. 2015, A&A, 579, A28
- Frebel, A., & Norris, J. E. 2015, arXiv:1501.06921
- Freeman, K., & Bland-Hawthorn, J. 2002, ARA&A, 40, 487
- Hansen, T., Hansen, C. J., Christlieb, N., et al. 2015, ApJ, 807, 173
- Keller, S. C., Bessell, M. S., Frebel, A., et al. 2014, Nature, 506, 463
- Ness, M., Hogg, D. W., Rix, H.-W., Ho, A. Y. Q., & Zasowski, G. 2015, ApJ, 808, 16
- Placco, V. M., Frebel, A., Beers, T. C., & Stancliffe, R. J. 2014, ApJ, 797, 21
- Placco, V. M., Frebel, A., Lee, Y. S., et al. 2015, arXiv:1507.03656
- Schneider, R., Omukai, K., Limongi, M., et al. 2012, MNRAS, 423, L60
- Spite, M., Caffau, E., Bonifacio, P., et al. 2013, A&A, 552, A107

---

---

Time-Resolved Spectroscopy of  
J1321: A Mysterious Polar with  
Deep Absorption Features

---

---

PART OF THE REPORTS ON RESEARCH PERFORMED BY STUDENTS WHILE  
PARTICIPATING IN THE NSF-SPONSORED REU PROGRAM AT THE UNIVERSITY OF  
NOTRE DAME

TAYLOR HOYT

*2015 NSF/REU Program*

*Physics Department, University of Notre Dame*

ADVISOR: PROF. PETER GARNAVICH

## 1. Abstract

We present spectra of MASTER OT J132104.04+560957.8 (J1321) taken at the Large Binocular Telescope (LBT) in which we find short-lived, deep absorption features beginning around orbital phase  $\phi = -0.05$  and ending around  $\phi = 0.06$  of a 91 minute orbital period as determined by Littlefield et al.<sup>1</sup> The short and pronounced transition between emission and absorption, which includes Balmer absorption, suggests hydrogen gas at around 8000K-12000K is passing in front of our line of sight. This could be a result of a high mass accretion rate leading to an optically thick and steeply-inclined and/or sporadic accretion stream. The unfocused doppler tomograms suggest an extended accretion mechanism such as an accretion curtain rather than a column, while the apparent absence of cyclotron resonances in the continua and the shape of tomogram may imply a relatively weak magnetic field for a polar.

## 2. Introduction

### 2.1. The Basic Structure of CVs

Cataclysmic variables (CVs) are binary star systems which include a white dwarf (WD) primary and a low mass, typically main sequence, secondary that has filled its Roche lobe, the equipotential surface at which the gravitational forces from both stars are balanced. At this point, the denser primary WD begins to accrete mass from the surface of the secondary, known as Roche-lobe overflow. The primary could potentially accrete enough mass to push it over the Chandrasekhar limit and eventually lead to a supernova. This case, however, is best left to papers dealing specifically with supernovae and CVs with a more massive primary.

The Roche lobe is a teardrop-shaped equipotential contour formed around the massive object. The teardrop shape arises from the spherically symmetric gravitational potential of one object being elongated along the line connecting the two stars by the pull of the companion. Once matter from the secondary breaches its own Roche lobe, the primary begins to accrete this matter through the first Lagrangian point, one of the points of equal

gravitational strength in the system. Figure 1 will assist in visualizing and explaining the geometry.  $L_1$ ,  $L_2$ , and  $L_3$  are saddle points, and generally unstable since the slightest

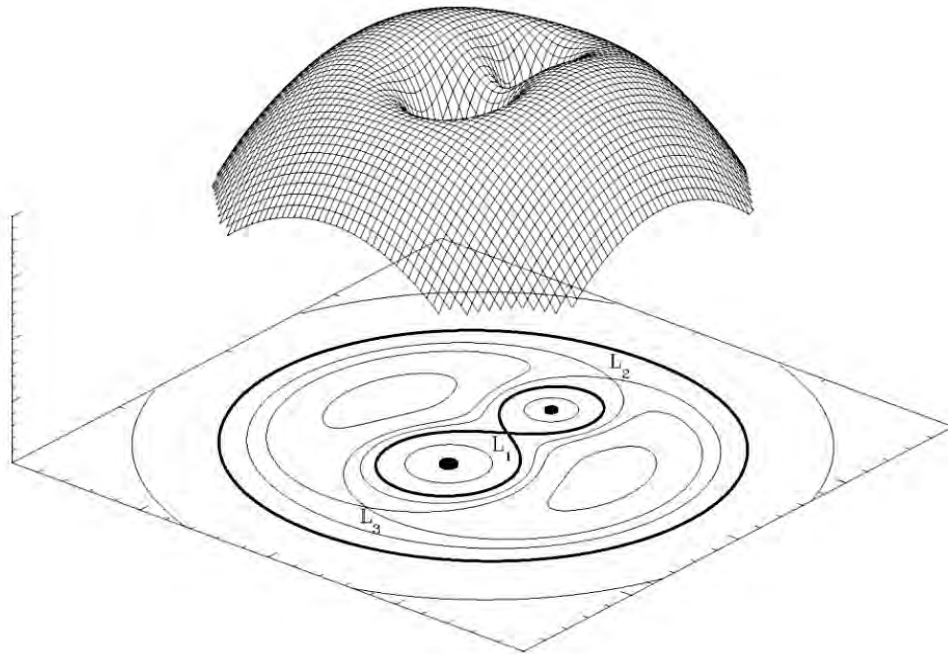


Figure 1: Contours of equal effective potential. The bold-faced lines near the points are the teardrop-shaped Roche lobes of each star in the binary system. Points labelled  $L_n$  are Lagrangian points.

deviation from these exact points would cause rapid flow down the potential contours toward the primary. The most important point for us to concern ourselves with is the  $L_1$  point, through which the primary accretes material. As can be seen in Figure 1, the Lagrangian point  $L_1$ , or the inner Lagrangian point, is the point at which matter that has just escaped the Roche lobe of the donor star will begin to flow around the primary due to its initial angular momentum. In standard CVs, this material loses its angular momentum through viscous and other frictional loss and eventually forms an accretion disk. In a polar, however, the accreted material rarely makes it around to the other side of the primary before getting trapped in its powerful magnetic field with strengths on the order of a few tens of to a few hundred MG.

## 2.2. Accretion in a Polar

The standard models for processes governing accretion in a polar are reviewed by Wu et al. (2003), of which the main ideas will be discussed below.<sup>2</sup> After the gas passes through the  $L_1$  point, it is transported along the dipole field lines of the WD onto one, or both, of the poles. As the gas streams towards the WD, it eventually rams into its surface heating the column of gas to temperatures between  $10^6$  and  $10^8$  K. The region where these accretion columns land on the WD primary becomes a hotspot, typically the brightest source of light in a polar. More dense clumps of gas can actually penetrate into the surface of the WD before being stopped and produce a “buried” shock which heats the WD surface.<sup>3</sup> The column also emits Bremsstrahlung X-rays and/or cyclotron radiation as its primary cooling mechanisms which ionize much of the stream above it and can also irradiate the surface of the secondary. This produces a hotspot in the vicinity of the secondary that can be clearly seen in many Doppler tomograms of polars.<sup>4</sup>

## 2.3. Polar Orbital Mechanics

Polars typically have short orbital periods less than 2 hours in length. Most commonly, a WD primary will rotate synchronously with the orbital period. This is due to a balancing between the torque of accreted material onto the primary and a torque in the opposite direction resulting from the magnetic field of the primary threading along the magnetic field of the donor star. The former works to speed up the rotation of the WD through transfer of angular momentum between the accreted material and the WD. If the orbit is asynchronous, this counter-torque increases considerably due to the field lines of the primary being tangled and threaded through the mass donor or along its own field lines. This “twisting” acts as a rubber band because the more the WD mangles and twists its field lines threaded into the secondary by rotating faster, the stronger the backwards pull from the magnetic stress.<sup>3</sup>

## 2.4. Data Collection and Reduction

The spectra were taken in 120s exposures at an approximately 2 minute readout time using one of the two 8.4m mirrors on the Large Binocular Telescope (LBT) using both the blue and red arms of the MODS spectrograph. The spectra were then bias-subtracted, calibrated in wavelength with Xe+Kr and Ne+Ar arclamps, for the blue and red respectively, and flux calibrated to the standard star HZ+33 using a high-order cubic spline fit. With an orbital period of 91 minutes, the entire run spans 1.4 orbital phase units with a resolution of about 0.04 phase units. Using the other mirror on the LBT, we took simultaneous photometry using the Large Binocular Camera (LBC). Exposures were approximately 15s in length with a 20s dark time giving us a phase resolution of 0.006 phase units.

## 3. The Reddened Continuum

We first look at the evolution of the continuum as a function of time using Figure 3 and confirm the presence of a reddened, almost blackbody, continuum initially seen in the spectra taken by Littlefield et al. The most red-centered spectrum is at  $\phi = 0.00$ , when the absorption is deepest, then the bump in the continuum begins to shift to the blue at the primary maximum located around phase  $\phi \sim 0.15$  and continues to shift blue-wards until  $\phi \sim 0.30$ . At this orbital phase, the continuum begins to flatten out and resemble a more typical polar continuum, which is especially evident in the spectrum right before  $\phi \sim 0.45$ . The phase interval of  $0.30 \sim 0.45$  corresponds to the secondary minimum seen in Figure 2. J1321 then returns to peak brightness at  $\phi \sim 0.70$  after returning to a reddened continuum centered around 4500-5000Å. The continuum then begins to flatten out again from phase  $0.75 \sim 0.90$ , coincident with the V magnitude dropping to the primary minimum. The continuum then transitions quickly to its absorption period from phase  $0.95 \sim 1.05$ . The spectra we obtained after  $\phi \sim 1.00$  follow closely with the corresponding spectra starting at  $\phi \sim 0.00$ , except that the repeated secondary minimum beginning around  $\phi \sim 1.30$  appears to have a much

shorter duration than the first. This is not certain as the increase in brightness could be another of this system’s previously observed, and seemingly random, flares on the order of 0.2 mag. The brighter periods coincide with the reddening of the continuum, suggesting that the majority of the cyclotron radiation, emitted along the direction of propagation of the ionized gas, is lining up with our line of sight.

#### 4. Doppler Tomography

In Figure 4, we look at one of the most powerful techniques in visualizing the dynamics of CVs in order to better understand J1321 as laid out in Marsh and Horne (1988) and later reviewed by Marsh (2001 & 2005) and Echevarria (2012).<sup>5678</sup> A doppler tomogram fits the phase-resolved trailed spectrum, a 2D representation of a particular emission line’s behavior as a function of time, and maps the resulting fit to velocity space in the orbiting inertial frame of the CV.

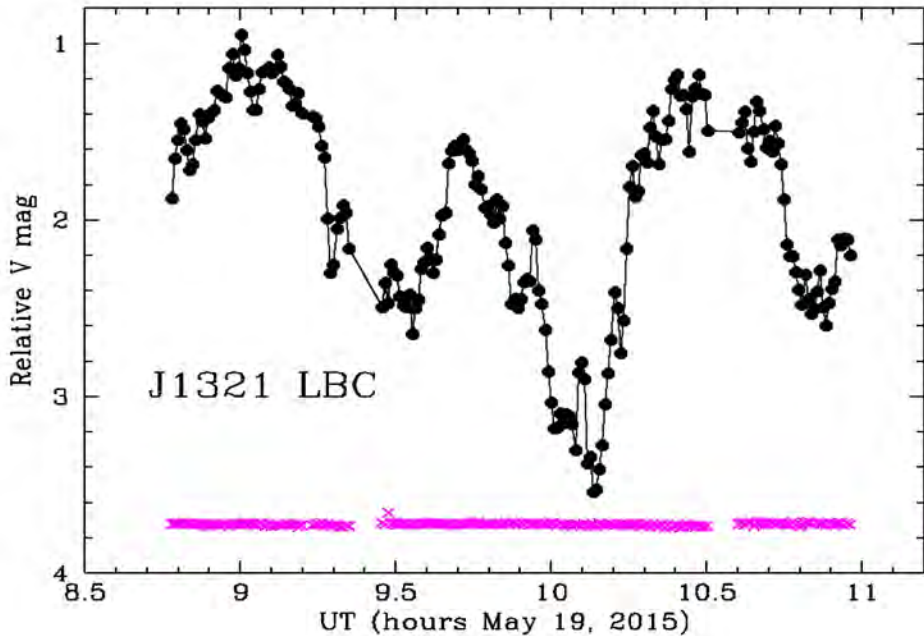


Figure 2: Light curve of J1321 taken simultaneously at the LBT in the V-band.

Positive  $x$  is in the direction from the WD to the secondary mass donor and positive  $y$  is defined as the secondary’s trajectory in the orbit. We see a high-velocity component that

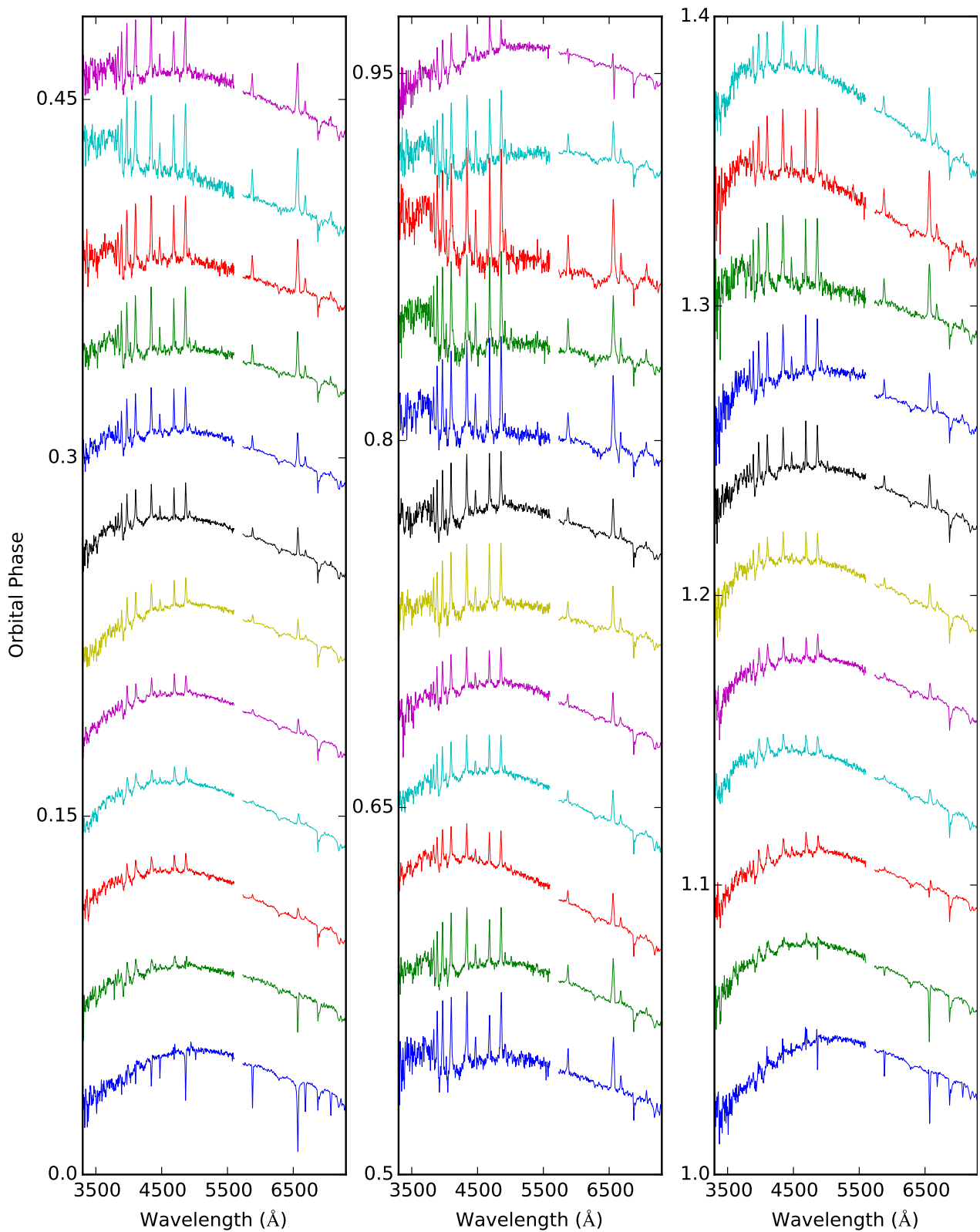


Figure 3: Spectra stacked according to mid-exposure phase to show the change in the shape of the continuum as a function of time. The vertical scale is in phase units while the horizontal scale is in Angstroms. Noisy calibration of the overlap region between the red and blue spectra led to the omission of the region from 5500-5650Å in the figure.

extends out to about  $1000 \text{ km s}^{-1}$  which is most likely the accretion stream or possibly, due to its blurred shape in velocity space, could suggest an accretion curtain with a larger spread of inclination and azimuthal angles. A very bright spot is centered around  $(v_x, v_y) = (0, 0)$  which tells us that a large amount of light is being emitted near the surface of the WD primary, in line with the earlier discussion on accretion in CVs. The hook-like blob that extends along the positive  $v_y$  axis is of particular interest. This is where we would expect to see another localized hotspot resulting from irradiation of the secondary by the X-rays and FUV light produced by the Bremsstrahlung and cyclotron radiation discussed earlier. This could imply a high mass accretion stream smothering and blocking the radiation from reaching the secondary. The structures seen in the tomograms of both CSS081231:071126+440405 (CSS 08) and J1321 are similar as the assumed ballistic stream appears to curve upwards instead of downwards as one should expect to see in a polar tomogram.<sup>9</sup> The blurred out or out-of-focus appearance of the tomogram may also suggest a weaker magnetic field as intermediate polars are known for the unfocused appearance of both their trailed spectra and resulting tomogram.

It is also worth noting that a similar, blob-like doppler tomogram was seen in the asynchronous polar BY Cam by Schwarz et al. (2005).<sup>10</sup> The HeII  $\lambda 4686$  tomogram in BY Cam is very similar to the same wavelength tomogram shown here leading us to believe the extended accretion mechanism exhibited in this system could apply to J1321 as well. However, the H $\beta$  tomogram actually shows a highly visible irradiated secondary and loses the hotspot near the WD entirely. Tomograms of H $\beta$  and other Balmer lines in J1321 do not exhibit this behavior at all, instead maintaining the same structure as found in the HeII  $\lambda 4686$  tomogram.

## 5. Conclusion

After reducing the phase-resolved spectra of J1321, we employed various techniques in an attempt to better understand this intriguing CV. We examined the stacked spectra to better

see how the continuum changes in time and the trailed spectrograms of certain lines and the resultant Doppler tomograms to try and grasp the structure and dynamics. Also, we have begun looking at radial velocity profiles of interesting lines, and will calculate artificial color magnitude light curves by integrating over set wavelength intervals. The techniques we have used, and plan to use, bring us closer to extracting more concrete information about J1321 and will prove to be invaluable experience in my planned future in academia. I would like to thank the National Science Foundation for funding my summer of research at the University of Notre Dame.

## References

- C. Littlefield, P. Garnavich, K. Magno, M. Murison, S. Deal, C. McClelland, and B. Rose. High-amplitude, Rapid Photometric Variation of the New Polar MASTER OT J132104.04+560957.8. *IAU Information Bulletin On Variable Stars*, Dec. 2014.
- Kinwah Wu, Mark Cropper, Gavin Ramsay, Curtis Saxton, and Chris Bridge. Accretion flow in magnetic cataclysmic variables. *Chinese Journal of Astronomy and Astrophysics*, 3(S1):235, 2003.
- B. Warner. *Cataclysmic Variable Stars*. Cambridge University Press, 1995.
- C. Hellier. *Cataclysmic Variable Stars - How and Why They Vary*. Springer, 2001.
- T. R. Marsh and K. Horne. Images of accretion discs. II - Doppler tomography. *Monthly Notices of the Royal Astronomical Society*, 235:269–286, November 1988.
- T. R. Marsh. Doppler tomography. In Henri M.J. Boffin, Jan Cuypers, and Danny Steeghs, editors, *Astrotomography*, volume 573 of *Lecture Notes in Physics*, pages 1–26. Springer Berlin Heidelberg, 2001.
- Tom Marsh. Doppler tomography. *Europhysics News*, 36(4):133–138, 2005.
- J. Echevarría. Doppler tomography in cataclysmic variables: an historical perspective . *Mem. Societa Astronomica Italiana*, 83:570, 2012.
- P. Garnavich. Private communication.
- R. Schwarz, A. D. Schwöpe, A. Staude, and R. A. Remillard. Doppler tomography of the asynchronous polar BY Camelopardalis. *Astronomy & Astrophysics*, 444:213–220, December 2005.

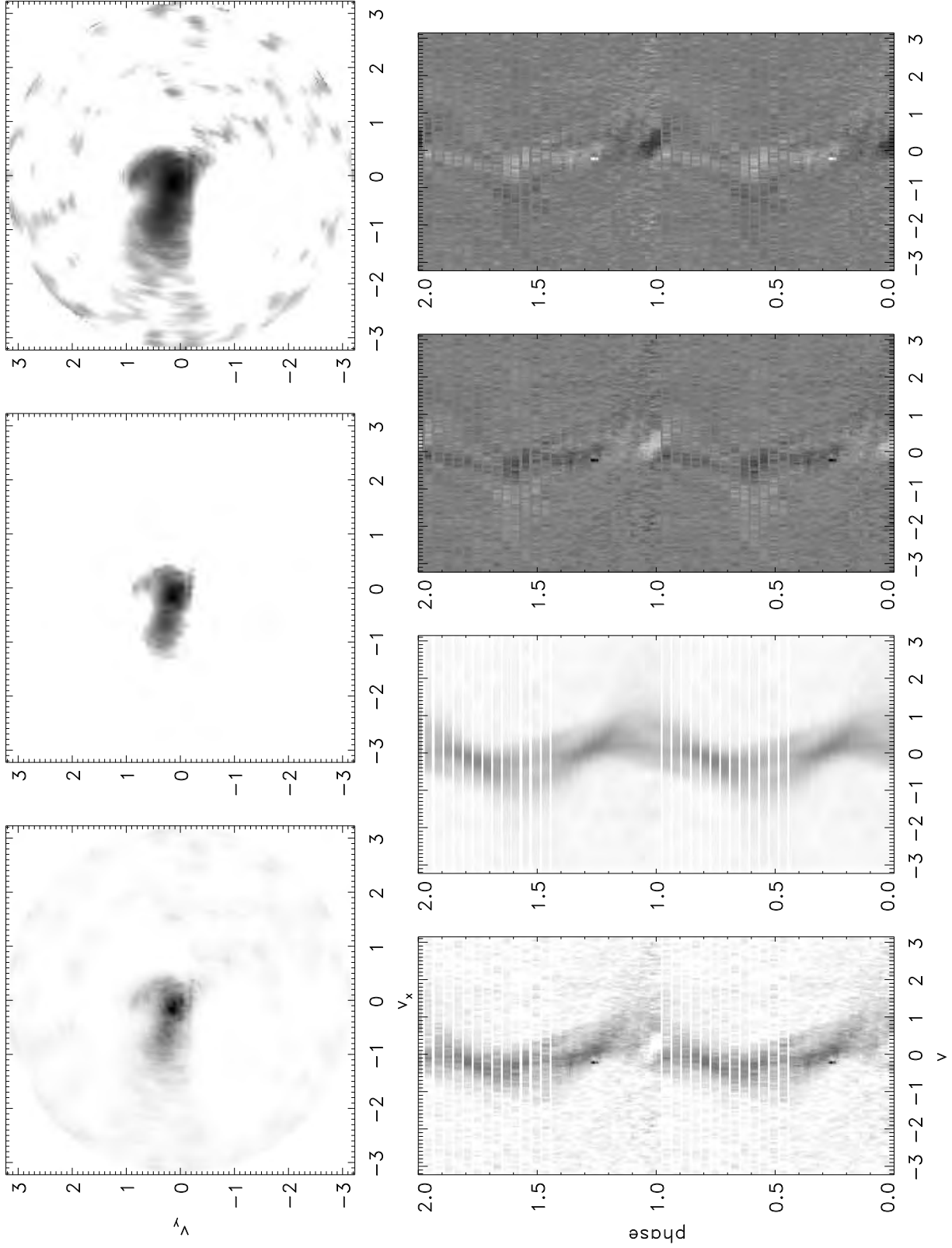


Figure 4: Top row, left to right: Doppler tomograms of HeII  $\lambda 4686$  with full range of contrast levels, with a raised minimum intensity level, with a lowered maximum intensity level. Bottom row, left to right: Phase-folded trailed spectrum of HeII  $\lambda 4686$ , the fit used to calculate the tomogram, the residuals, the negative of the residuals.

# Comparison of Optical Models for 400 MeV alpha scattering off $^{90}\text{Zr}$ and $^{92}\text{Mo}$

Dan Jones

Summer 2015 NSF/REU

Department of Physics, University of Notre Dame

Advisor: Dr. Umesh Garg

## Abstract

Nuclear incompressibility is an important parameter governing the equation of state of nuclear matter. From the measurable centroid energies of the Isoscalar Giant Monopole Resonance (ISGMR), the incompressibility of the nuclear matter can be calculated. The first step in this process is to fit the elastic scattering angular distributions for a particular reaction and to test the obtained model dependent parameters by calculating low-lying discrete state angular distributions for target nuclei. This study tests the suitability of two optical models to reproduce the angular distributions of differential cross sections from elastic and inelastic scattering of 400-MeV alpha particles. The elastic distributions for two heavy isotopes,  $^{90}\text{Zr}$  and  $^{92}\text{Mo}$ , are analyzed and the best parameter sets for each are shown. In the first model, a single folded potential is used for both the real and imaginary volume terms, and the second model utilizes a single folded potential for the real volume term, and a phenomenological Woods-Saxon potential for the imaginary volume term. From this comparison, it is concluded that the second model, the so called 'hybrid model,' is better able to reproduce the angular distributions for both  $^{90}\text{Zr}$  and  $^{92}\text{Mo}$ . Future work will include the comparison of the optical models for  $^{92}\text{Zr}$ , as well as Multipole Decomposition Analysis (MDA) of each reaction to extract the contributions of each resonant mode to the differential cross sections.

## Introduction

The nuclear equation of state (EoS) governs various astrophysical quantities, such as the radii and lifetime of neutron stars and the density of the core of a Type II supernova. Currently, there is still a high degree of uncertainty in the exact form of this EoS, and one of the parameters that needs to be further constrained is the nuclear incompressibility of infinite nuclear matter,  $K_\infty$ . This quantity is defined in terms of the change in the binding energy per nucleon at saturation

density, and can be extracted from the incompressibility of finite nuclear matter  $K_A$ .  $K_A$  can be measured experimentally by the excitation of the ISGMR according the following relation:

$$E_{ISGMR} = \hbar \sqrt{\frac{K_A}{m\langle r \rangle^2}} \quad (1)$$

where  $E_{ISGMR}$  is the measured centroid energy of the ISGMR. In order to be confident in the measured value of  $E_{ISGMR}$ , it first becomes necessary to develop model dependent parameters which allow us to accurately reproduce transition angular distributions in inelastic scattering processes. The means by which we model the target-projectile interactions is the optical model, which describes the interaction between nuclei in terms of a complex potential:

$$U(\mathbf{r}) = -V_V(\mathbf{r}) - iW_V(\mathbf{r}) - V_S(\mathbf{r}) - iW_S(\mathbf{r}) + V_{S.O.}(\mathbf{r}) + V_C(\mathbf{r}) \quad (2)$$

In the above, the real parts are responsible for the elastic scattering and describes the ordinary nuclear interaction between target and projectile, and the imaginary terms are responsible for the absorption.<sup>1</sup> As the nuclear interaction is not well understood, to describe the interaction between the projectile and the target, it is necessary to adopt phenomenological models. The first attempts to parameterize the optical model utilized phenomenological form factors of the Woods-Saxon type:

$$f(r, R, a) = \left[ 1 + \exp\left(\frac{r-R}{a}\right) \right]^{-1}. \quad (3)$$

The real and/or imaginary volume term (subscript V) in the optical model potential given by equation (2) can be represented by the product of a potential depth and the Woods-Saxon form factor. The derivative of equation (3) is necessary to calculate the surface (subscript S) and spin-orbit (subscript S.O.) terms, and the calculation of these terms again requires a linear dependence on the potential depth.<sup>2</sup> Inclusion of the two surface terms is optional and they are added only when it essentially improves agreement with the data.<sup>3</sup> Because isospin-0 probes cannot magnetically

couple to the nucleus and there is no spin-orbit flip interaction, the spin-orbit term is only included when the overall spin of the incident particle beam is non-zero (as in proton scattering). The above describes a phenomenological Woods-Saxon optical model which essentially describes the nuclear scattering reaction as a two point-particle (nucleus-nucleus) interaction.

More recently, it has become possible to fold the potentials over the distribution of mass of one or both of the interacting nuclei (these are known as single or double folded potentials respectively). In such cases, the Woods-Saxon form factor is replaced by an integration over the density distribution of the particular nucleus. As such, the determination of the exact distribution of nuclear mass has become an area of intensive research.<sup>4</sup> The integration over the continuum of the nucleon-nucleus pair interaction typically results in a more precise potential distribution than that obtained from a phenomenological interpretation. The single folded optical model essentially describes the nuclear reaction in terms of the potential interaction between the nucleus (regarded as a point-like particle in this interpretation) of one of the interacting pair with the continuous distribution of mass in the other nucleus (a nucleus-nucleon interaction).

A pure single folded optical model potential utilizes the singly folded potentials for both the real and imaginary volume terms of the optical potential. In this model, the surface and spin-orbit terms, when included, are still adopted as Woods-Saxon form factors. The hybrid model utilizes a single folded potential for the real volume term, and the imaginary term is treated phenomenologically, using a conventional Woods-Saxon form.<sup>3</sup> In previous studies, the hybrid model has been shown to reproduce the elastic and inelastic data better than the pure single folded and pure phenomenological potentials for alpha particle scattering off heavy nuclei.<sup>3</sup> These studies have been conducted up to incident beam energies of 300 MeV, thus this report will test the consistency of these results up to 400 MeV.

## Procedure

Excitation of the ISGMR for  $^{90}\text{Zr}$  and  $^{92}\text{Mo}$  can be achieved by elastic and inelastic alpha particle scattering at forward angles ( $3^\circ - 30^\circ$ ). The experiment was conducted using the Ring Cyclotron at the RCNP (Research Center for Nuclear Physics) facility at Osaka University, Japan. This facility includes the Grand Raiden spectrometer, which affords excellent abilities for a study of this kind.<sup>5,6</sup> Most importantly, Grand Raiden provides the ability to effectively eliminate all instrumental background from the final spectra. To eliminate this noise, a vertical-position spectrum at the double-focused position of the spectrometer was utilized.<sup>6</sup> The vertical focusing allows for a clear quantification of the amount of background events which can be then entirely subtracted.

The single folded potentials were produced using the computer code `sdolfin`, which reads the density distribution parameters for a two parameter Fermi distribution, shown in Table 1 for  $^{90}\text{Zr}$  and  $^{92}\text{Mo}$ .<sup>7</sup> `Sdolfin` outputs the single folded potentials as a function of radius, which are then taken and input explicitly as the real and imaginary volume potentials into the computer code `ecis97`. The single folded potentials were exchanged with phenomenological form factors as necessary depending on the particular optical model in use. From these optical model potentials, `ecis97` computes the differential cross sections as a function of scattering angle, which can then be compared to the angular distributions extracted from the experimental data. By using a least-chi-

Density distribution parameters	$^{90}\text{Zr}$	$^{92}\text{Mo}$
$\rho_0$ ( $\text{fm}^{-3}$ )	0.165	0.168
c (fm)	4.9	4.9
a (fm)	0.515	0.515

Table 1. The Mass density distribution for  $^{90}\text{Zr}$  and  $^{92}\text{Mo}$ . In this analysis, the radius and diffuseness for the two isotopes were assumed to be equal, the difference being the normalization term,  $\rho_0$ .

squared fit to the elastic scattering angular distributions, the best optical model parameter sets were chosen, and these sets were tested against the inelastic scattering data to ensure that the elastic minima in chi-squared do not correspond to weak local minima. The transition potentials for the  $2^+$  and  $3^-$  discrete states were calculated from the excitation energy of each state, as well as the adopted B(EL) values for each state.<sup>8</sup> The adopted values of B(EL) refer to the reduced electric-multipole transition probabilities for the  $L^{\text{th}}$  order.<sup>9</sup>

One of the key components in determining the best optical model parameters is the ability of ecis97 to discover the absolute minimum in the chi-squared space. This component in the fitting process was tested for  $^{90}\text{Zr}$  by first performing a manual search of the parameter space, and comparing the results of this search to the parameter sets obtained from an unpublished computer program written by Dr. James Matta. Without delving too deep into the subtleties of the program, 360,000 different initial parameterizations were input into ecis97, and again a least-chi-squared approach was utilized for each initial parameter set. The result of the least-chi-squared approach for both the manual and program searches is a final optical model parameter set corresponding to the local minima in chi-squared. The stated aim of this program was to reduce the time spent on the manual fitting process, and this goal was clearly met. This test must again be performed for  $^{92}\text{Mo}$  to confirm the existence of an absolute minimum in the chi-squared space found from the manual fitting process.

## Results

The elastic and inelastic scattering for  $^{90}\text{Zr}$  is shown in Figure 1 below, where the discrete values are the experimental data and the solid lines show the optical model calculations for both

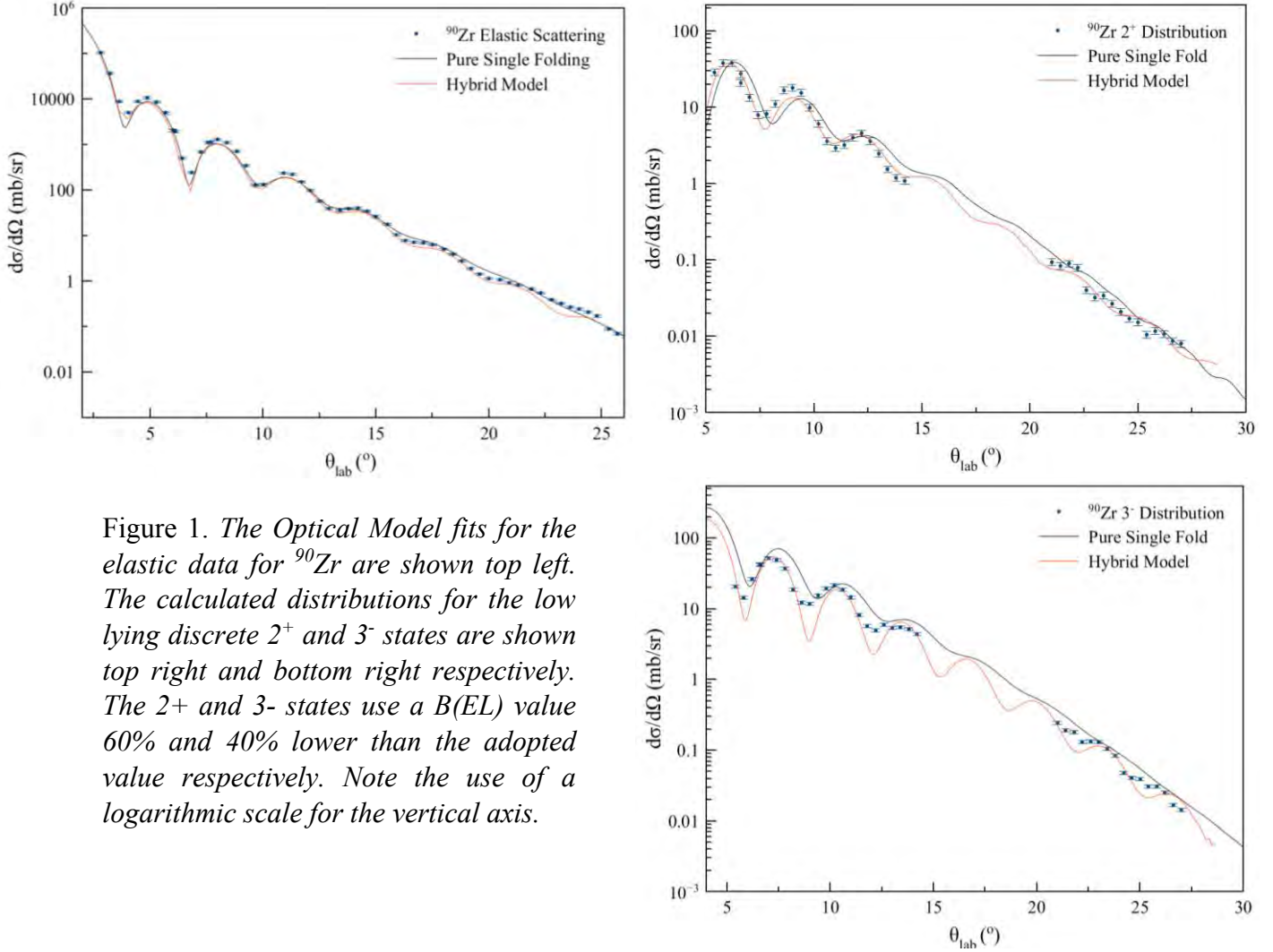


Figure 1. The Optical Model fits for the elastic data for  $^{90}\text{Zr}$  are shown top left. The calculated distributions for the low lying discrete  $2^+$  and  $3^-$  states are shown top right and bottom right respectively. The  $2^+$  and  $3^-$  states use a  $B(EL)$  value 60% and 40% lower than the adopted value respectively. Note the use of a logarithmic scale for the vertical axis.

Pure Single Folding	$V_V$ (MeV)	Radial real volume	$W_V$ (MeV)	Radial imaginary volume component	Reduced $\chi^2$
$^{90}\text{Zr}$	86.068	1.0225	26.402	1.085	12.4
$^{92}\text{Mo}$	63.738	0.944	35.508	1.0545	10.15

Table 2. The optical model parameters extracted from the pure single folding technique. The radial component can be thought of as a horizontal stretching term. Although there is a slight difference in the optical model parameters found from manual fitting and from the unpublished program, the elastic distributions, the distributions for each excited state, and the  $\chi^2$  values were identical.

modeling techniques. The extracted optical model parameters for pure single folding of  $^{90}\text{Zr}$  and  $^{92}\text{Mo}$  are listed in Table 2, and those for the hybrid model are shown in Table 3. The hybrid model distribution for  $^{90}\text{Zr}$  was found and provided by another member of the research group.<sup>10</sup> It is

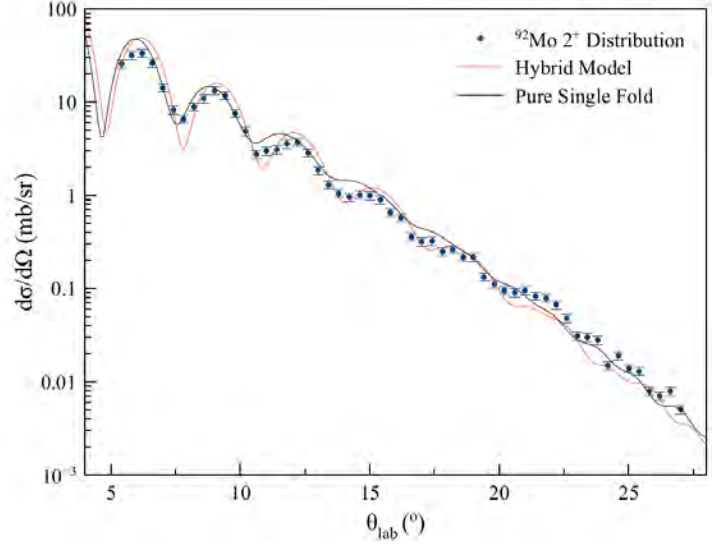
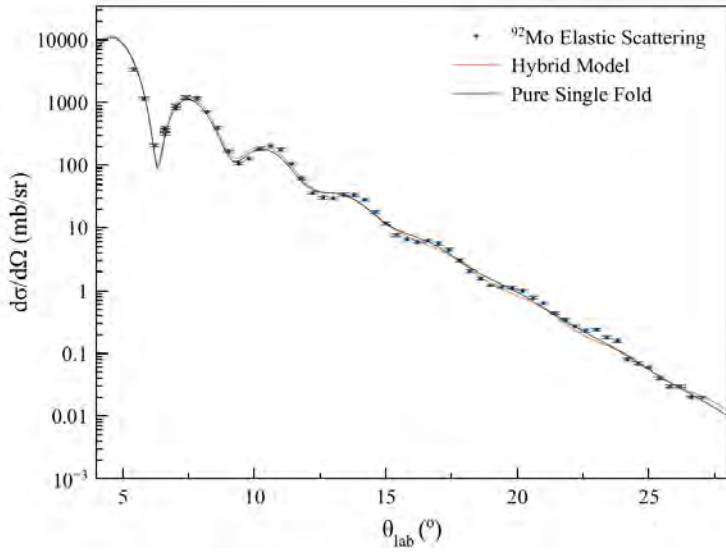
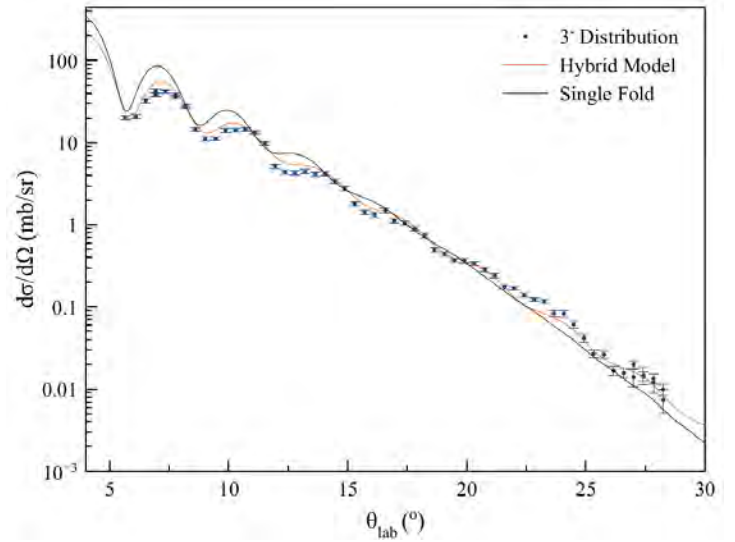


Figure 2. The Optical Model fits for  $^{92}\text{Mo}$  alpha particle scattering. The incident particle beam was at  $E_{\text{Lab}}=386$  MeV for both nuclei. The  $2^+$  and  $3^-$  distributions use a  $B(EL)$  value 60% and 40% lower than the adopted value respectively. It is important to note that the hybrid model distributions for  $^{92}\text{Mo}$  are considered preliminary, and that this will be an area for future work.



Hybrid Model	$V_V$ (MeV)	Radial real volume component	$W_V$ (MeV)	$R_{WV}$ (fm)	$a_{WV}$ (fm)	Reduced $\chi^2$
$^{90}\text{Zr}$	97.438	1.00	32.975	1.0263	0.59004	8.7
$^{92}\text{Mo}$	78.377	0.955	37.748	1.339	0.678	9.9

Table 3. The optical model parameters extracted from the hybrid model. The last three columns represent Woods-Saxon parameters, with the latter two comprising the form factor itself. It is called a form factor since the radial dependence is what gives the potential its structure – the depth is merely how attractive (or repulsive) the potential can be. These parameters are used to describe the imaginary term of the optical potential.

important to note that the optical model parameters for  $^{92}\text{Mo}$  are considered preliminary, and that the angular location of each peak is the most important aspect of the inelastic distributions, as opposed to their magnitudes. The optical model parameters for  $^{90}\text{Zr}$  found from the manual fitting process correspond to identical distributions as the parameter sets obtained from the unpublished

program. The distributions for  $^{90}\text{Zr}$  and  $^{92}\text{Mo}$  are both shown in the lab frame with the error fixed at 5% of the experimental differential cross sections. These errors are the result of several factors, including the uncertainty from the momentum analysis during the data acquisition, and statistical errors.

## Conclusions

Parameter sets were found for the real and imaginary volume terms of the Optical Model for 400 MeV alpha particle scattering off  $^{90}\text{Zr}$  and  $^{92}\text{Mo}$  by fitting the angular distributions of differential cross sections for elastic scattering. These parameter sets were then shown to be able to reproduce the inelastic distributions within the errors quoted by the appropriate B(EL) sources. The transition potentials for both excited states were calculated using the adopted B(E2<sup>+</sup>) and B(E3<sup>-</sup>) values. While both optical models fit the elastic distribution reasonably well, it is clear that the hybrid model was able to reproduce the structure of the elastic and inelastic angular distributions at higher scattering angles better than the pure single folding technique. Based on the comparison of optical models, it can be concluded that the hybrid optical model consistently reproduces the elastic and inelastic angular distributions for the ( $\alpha,\alpha'$ ) reaction up to 400 MeV incident energy better than the single folded potentials.

## Acknowledgements

I would first like to thank the University of Notre Dame and the NSF/REU program for providing me the experience of participating in this wonderful opportunity. Special thanks go to my advisor Dr. Umesh Garg for admitting me into the program and allowing me to work with his research group. Special thanks also go to Kevin Howard for his patient guidance and thorough

oversight throughout the summer, and also to Menekse Sinyiget for providing the hybrid model parameters for  $^{90}\text{Zr}$ .

## References

1. Krane, Kenneth. *Introductory Nuclear Physics*. (1988)
2. Howard, Kevin. *Study of the Pure Double Folding Optical Model for 100 MeV/u Deuteron Scattering*. 2014 NSF/REU Program, University of Notre Dame.
3. Khoa, Dao T., Satchler, G. R., W. von Oertzen. *Nuclear incompressibility and density dependent NN interactions in the folding model nucleus-nucleus potentials*. Phys. Rev. C. **56**. 954-969. (1997).
4. Alvarez, M. A. G. et. al. *Precise nuclear matter densities from heavy-ion collisions*. Phys. Rev. C. **65**. 014602. (2001).
5. Fujiwara, M. et. al. *Magnetic spectrometer Grand Raiden*. Nuclear Instruments And Methods in Physics Research A **422**. (1999) 484-488.
6. Hedden, M., Garg, U. *The Isoscalar Giant Dipole Resonance in  $^{208}\text{Pb}$  and the Nuclear Incompressibility*. Nuclear Physics in the 21st Century, 2002, (880).
7. Vries, H. De. et al. *Nuclear Charge-Density-Distribution Parameters from Elastic Electron Scattering*. Atomic Data and Nuclear Data Tables **36**, 495-536 (1987).
8. National Nuclear Data Center, Reduced Transition Rate Probabilities: Brookhaven National Laboratory. [www.nndc.bnl.gov](http://www.nndc.bnl.gov).
9. Kibedi, T., and Spear, R. H. *Reduced Electric-Octupole Transition Probabilities:  $B(E3; 0_1^+ \rightarrow 2_1^+)$ —An Update*. Atomic Data and Nuclear Data Tables **80**, 35-82. (2002).
10. M. Senyigit, private communication.

Resolution and Stability Analysis of the ATF2  
Straightness Monitor

Changhao Li

2015 REU Program

Physics Department, University of Notre Dame

Advisor: Michael Hildreth

## Abstract

The Accelerator Test Facility 2 (ATF2) is a demonstrator system for final focus beam lines of future linear high energy colliders. There is a cavity beam position monitor (BPM) system and a Zygo interferometer system as part of the ATF2 diagnostics. This article mainly describes trying to improve the resolution of the BPMs using the Zygo interferometers to correct for mechanical shifts. The long-term stability of the system and the relationship with temperature are also discussed.

# 1 Introduction

## 1.1 BPM system

The Accelerator Test Facility 2 (ATF2) [4] at KEK laboratory in Japan uses the beam extracted from the ATF damping ring to help design the focusing system and analyses its stability for future linear high energy colliders [1].

The ATF2 beam line is instrumented with 37 BPMs, which are inside or close to quadrupole or sextupole magnets. They are installed for the purpose of measuring the beam trajectory with high precision in order to maintain and monitor the stability of nanometer sized beams.

Cavity BPMs are used in the system because of their potential of achieving high resolution in the nanometer range and with center accuracy at the micrometer level [2]. The resolution can be measured by comparing the predicted beam position at each BPM with the measures value. The beam position can be predicted by using singular value decomposition method (SVD) to calculate the trajectory of the beam

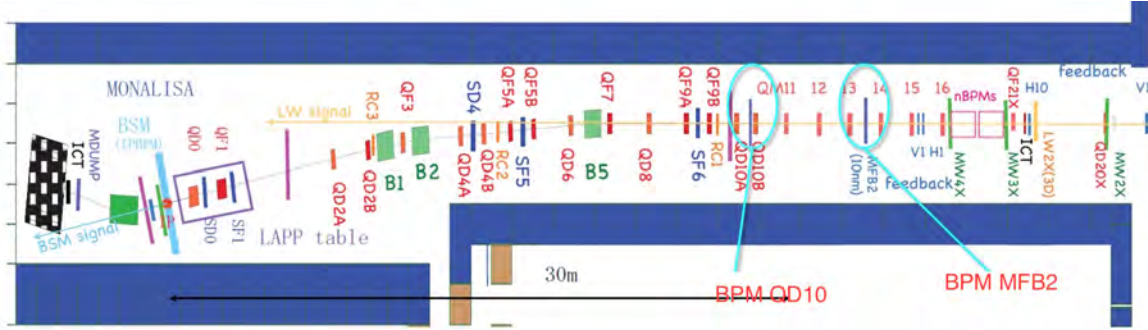


Figure 1: The ATF2 beam line, marking the BPMs, from ref [3]

through the entire beam line [1]. The resolution of the BPM is defined as the root mean square values of the residuals  $R_i$  between the predicted beam position values and measured values.

$$\sigma = \sqrt{\frac{\sum_i^N R_i^2}{N}} \quad (1)$$

The best resolution that has been seen until now is 27nm, which is surely sufficient for the need of the AFT2, but this resolution was only achieved in specific conditions. In our analysis, we find much larger values, and only consider the data files with the smallest available resolutions ( $\leq 150$  nm), which are the most useful for our resolution analysis.

Magnets after QM16FF with the BPMs mounted on their poles are placed on movers [1]. The movers are capable of moving the magnets a few microns over a range of several millimeters, with a position precision of  $2 \mu m$ . Movement of order hundreds of microns is needed in a BPM calibration step, which we will see in the plots discussed below.

## 1.2 Zygo interferometer system

Zygo interferometers and CCD cameras are set up in the system for the purpose of measuring relative position of system components. The Zygo system has been shown to have a resolution of approximately 7nm in air. In our study, we are interested in the three Zygo interferometers which are installed with BPMs in order to observe the motion of the BPMs.

The data of position, speed and time is recorded by the interferometers with about 300 ms spacing and 200 beam pulses or entries for each data file. At every turn four measurements are taken with a time difference of 475 ns. Since the speed is given in units taken directly from the electronics, we first calculate the constant coefficient  $k$  of the speed values using the simple formula  $\frac{y_2 - y_1}{t_2 - t_1} = v_1 \cdot k$ . The time difference between the four measurements is quite small hence it can be regarded as uniform motion. Calculation shows the constant coefficient is  $6.3562 \times 10^{-5}$ . With such a high resolution system, the interferometer system should allow a determination of BPM electrical and mechanical resolution and long-term stability.

## 2 Resolution Studies

### 2.1 Velocity and position extrapolation

As explained above, higher resolution BPMs are necessary for the system. Our purpose is try to figure out whether we can use the Zygo interferometer measurements to subtract vibration and hence improve the measured BPM resolution. Only the BPM that is being monitored by the second interferometer, which monitors the

sixteenth BPM, has a good enough resolution that we have a chance at seeing an improvement if we subtract the vibration.

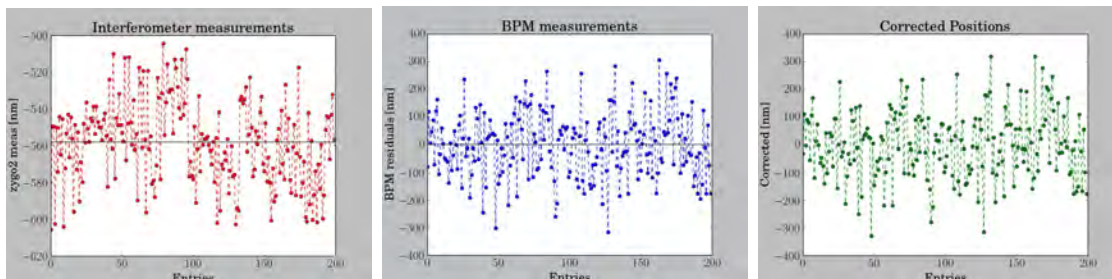


Figure 2: BPM and interferometer measurements as well as the subtraction

The problem is that the interferometer measurements were not necessarily taken at exactly the time when the beam passed the BPM, so we don't know the beam arrival time. While there are four measurements each time, we don't know which, if any, correspond to the exact arrival time. Considering this dilemma, we would like to extrapolate the position forward or backwards in time, and see if we can measure an improvement in the resolution as a function of time. If a minimum in resolution can be observed, the time shift should correspond to the time offset for the beam arrival.

The extrapolation is quite simple. As we have the speed values of BPMs, it makes sense to using the fourth (or third) speed  $v_4$  and position  $p_4$  to go forwards in time and using the first (or second) values to go backwards, as the formula below shows.

$$\begin{aligned}
 p_{forward} &= p_4 + v_4 \cdot k \cdot \Delta t \\
 p_{back} &= p_1 - v_1 \cdot k \cdot \Delta t
 \end{aligned}
 \tag{2}$$

To see the accuracy, we compared the measured speed values with the values

calculated using the position and time data. The result shows that in a small time range the error of the extrapolation is reasonable. Previously, the extrapolations up to 1ms have been shown to be good to 10 nm.

Furthermore, as we don't know the sign of whether the BPM is going upward or downward, both the plots of minus the vibration and plus the vibration should be considered. Comparing with the resolution without subtraction, we can know how well the interferometer is corrected.

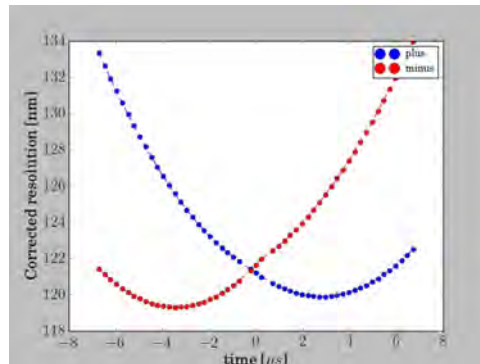


**Figure 3:** Resolution vs time

In theory, the measured beam positions should be the sum of the true positions and the BPM vibrations, which both obey a Gaussian distribution and are independent. The relationship of standard deviations should be:

$$\sigma_m^2 = \sigma_t^2 + \sigma_v^2 \quad (3)$$

Since we know the distribution width  $\sigma_v$  of the interferometer measurements and the means of the residuals are close to zero, the corrected resolutions are expected to be  $\sqrt{\sigma_m^2 - \sigma_v^2}$ .

Fitting of the resolution vs time gives us the minimum values. A quadratic function fits pretty good, with more than 99% of the coefficient of determination. For every data file, the fitting function, the distribution width, the original resolution, the minimum resolution, and the time of the minimum are recorded.

Apparently using the first and fourth data works better than using the second and third, as expected. Furthermore, minus the vibration can lead to a better result

in most cases. Basically the beam arrival time is within a  $3 \mu s$  range from the middle of our measurements, which is reasonable compared with the 300 us spacing. Two results from these studies are confusing: firstly the resolution only improved for about half of the data files, and then by only about 1 nm while the expected average improvement should be about 2.5 nm; Secondly the beam arrival time seems to vary with the data files. Further analysis may be needed for this.

## 2.2 Huge movements

We also analyzed data files corresponding to BPM calibrations. In figure4, huge movements can be seen in both BPMs (Fig.4) and interferometers (Fig.5) due to the shifting of the magnet movers.

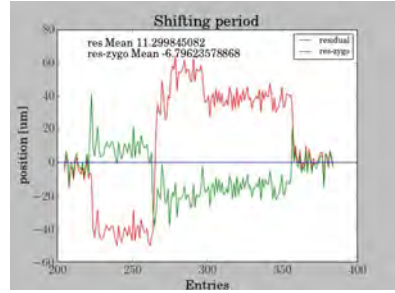
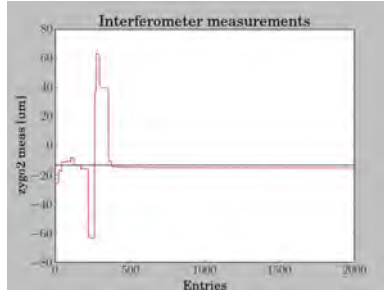
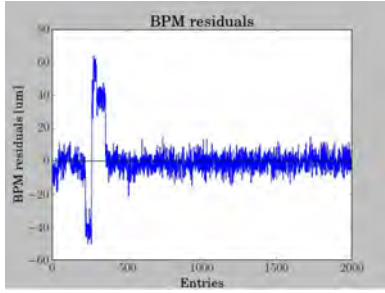


Figure 4: BPM measurements

Figure 5: Interferometer measurements

Figure 6: Correction in shifting period

In order to study the performance in this extreme situation, we look at the mean values before and after correction in the shifting period to know how well the interferometer corrected, as Fig.6 shows.

Similarly, we calculated the resolution in periods which have large movements. Among the data files we study, the resolution are improved for a half. Both the

mean values and the resolution show the interferometer corrects pretty well in this extreme case.

### 3 Stability

#### 3.1 long-term stability

The future application of these techniques would be to build a "LEP-style" BPM-based energy spectrometer [3], which uses a precise measurement of the beam bending in a magnetic field to calculate the energy. In order for this technique to work, the system must be stable for time scales of order 1 hour.

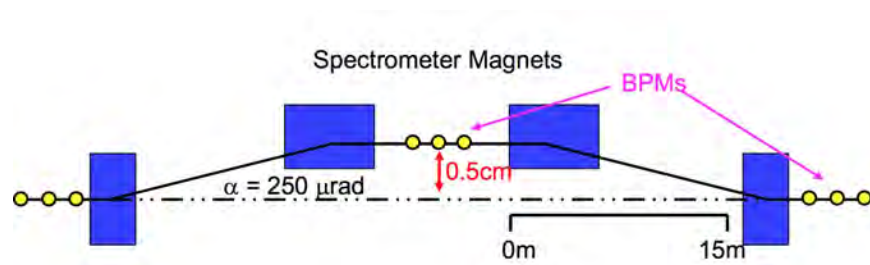


Figure 7: Energy spectrometer system, from ref [3]

To achieve sufficient precision of the energy measurement, the stability of the BPM needs to be less than 100nm vibration over half an hour. Considering this, we study the max and average gradient of BPM vibrations over hours.

The Fig.8 shows us the long-term BPM position changing. The average slope in the periods we studied is 38.62 nm/h and the max slope is 143.86 nm/h, which can basically meet the requirement of the energy spectrometry.

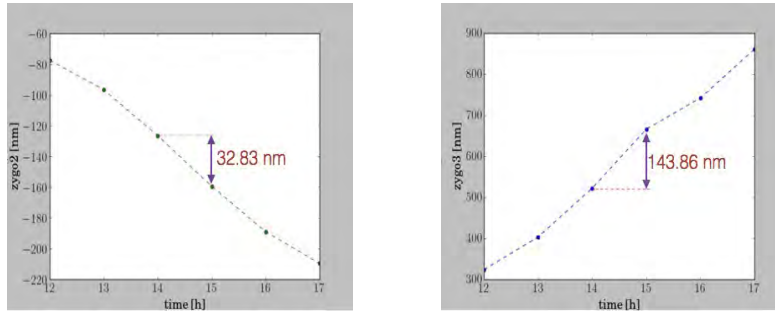


Figure 8: BPM absolute position changing over period 12:00-18:00

### 3.2 Influence of temperature

A collection of thermistors are installed in the BPM system hence most BPMs have a measurement of temperature. Temperature changes would lead to slow thermal expansions of system components as well as a change in the index of refraction of the air, which would change the optical path length of the interferometer and look like real motion.

Further analysis would concentrate on the influence stated above. Since we don't have temperature data now, we studied the long-term position change of the BPM and Zygo measurements as well as the residuals in order to see what if temperature change leads to thermal expansion. The result shows that over a period of several hours, the residuals only shift in a scale of several nanometers, much small compared with BPM (several microns) and interferometer (several ten nm) measurements. It indicates that if all the components go up or down because of shift of temperature, the residuals would only change in a small range.

## 4 Conclusion

In this report, we describe studies of the BPM resolution in ATF2 and attempt to the way to improve the measured BPM resolution by subtracting the interferometer measurements. For small vibrations, only some of the BPMs show improved resolution after interferometer subtraction, but with a magnitude much less than theory predictions. For huge movements like the mover calibration step, the resolution has an obvious improvement. As it's more important to get the true resolution of small movements in the system, further analysis may be necessary.

As for the stability, the long-term BPM motions are studied and basically the stability can meet the need of future energy spectrometry. Beam position residuals change for a small scale over periods of several hours. Further analysis would focus on the influence of temperature.

## References

- [1] *Cavity beam position monitor system for the Accelerator Test Facility 2*, Y.I.Kim, et al. Phys. Rev. ST Accel. Beams 15, 042801 (2012).
- [2] *Cavity BPM designs, related electronics and measured performances*, D. Lipka. Proceedings of DIPAC09, Basel, Switzerland 2009
- [3] *The Straightness Monitor System at ATF2*, Michael Hildreth, et al.
- [4] ATF Collaboration, <http://atf.kek.jp/collab/ap/>

**Testing the predictive power of statistical model calculations  
of the  $(\alpha, \gamma)$  reaction cross-sections for the  $p$ -process**

Brendan Murphy

2015 NSF/REU Program  
Department of Physics, University of Notre Dame (UND)  
Nuclear Science Laboratory (NSL)

Advisor: Prof. Anna Simon

**Abstract:**  $p$ -process nucleosynthesis is believed to be the origin of 35 stable, proton-rich nuclei called “ $p$ -nuclei”, that cannot be synthesized by neutron captures in the  $r$ - and  $s$ -processes. The complex  $p$ -process network includes, among others,  $(\alpha, \gamma)$  reactions, whose cross-sections are not very well described by current theoretical models. Here, a collection of experimentally measured  $(\alpha, \gamma)$  reactions from the KADoNiS- $p$  database was used as a test for various models obtained from TALYS, a nuclear reaction program, and NON-SMOKER, the principal theoretical database in this field. Statistical models in this investigation required the alpha optical model potential, the gamma strength function, and the level density model as input. Permutations of all three were used in theoretical calculations; after calculating cross-sections, a  $\chi^2$  test was used to determine the set of permutes that was closest to the experimental data. The  $(\alpha, \gamma)$  reaction of the  $^{91}\text{Zr}$  target is presented as the example case.

### **Introduction:**

The “ $p$ -nuclei” are the naturally occurring isotopes of certain elements between selenium and mercury. These isotopes are believed to form in the O/Ne burning layers of massive stars (on the order of  $25M_{\odot}$ ) during their explosions as type II supernova, through the  $p$ -process [1]. In current  $p$ -process models, pre-existing heavy “seed” nuclei are destroyed by photodisintegration reactions, producing unstable proton-rich nuclei; these unstable nuclei then  $\beta^+$ -decay to stability, producing the  $p$ -nuclei. This makes the  $p$ -process unique in the nucleosynthesis (NS) investigation as a whole, since the other major models are the  $r$ - and  $s$ -processes, both of which are neutron-capture processes. The ‘ $r$ -’ and ‘ $s$ -’ stand for ‘rapid-’ and ‘slow-’ neutron capture, respectively, and are responsible for the production of most of the stable nuclei via neutron capture followed by  $\beta^-$ -decay [2]. The abundances of the heavy isotopes created in each of these processes are shown in Figure 1.

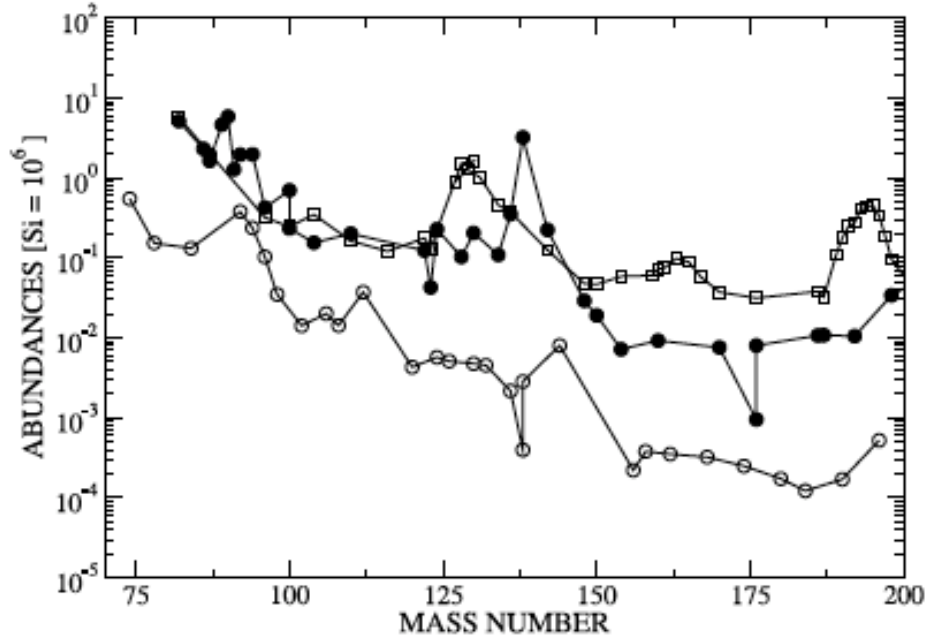


**Figure 1** – Relative abundance of heavy isotopes synthesized in the  $p$ - (open circles),  $r$ - (squares), and  $s$ -processes (filled circles). Image taken from [1].

There are questions concerning the mechanisms of  $p$ -nuclei synthesis, as well, and only a handful of reactions associated with the  $p$ -process have been measured. For example, it is possible to synthesize some  $p$ -nuclei through  $\gamma$  photodisintegration reactions, which follow nuclear reactions of the type  $(\gamma, n)$ ,  $(\gamma, p)$ , or  $(\gamma, \alpha)$ , and which have photons as the impetus for reaction [2]. Through these reactions,  $s$ - and  $r$ -nuclei can become proton-rich nuclei, as explained earlier. Other reactions associated with  $p$ -nuclei synthesis include  $\nu$ -process reactions triggered by neutrinos, and  $p$ -,  $n$ -, or  $\alpha$ -particle-capture processes (*i.e.*, the reverse reactions of the photodisintegration series) [3]. These latter processes are of particular interest because their cross-sections relate to those of the  $\gamma$ -induced reactions. And, while the  $\gamma$ -induced reactions are difficult to measure in the lab, the inverse reactions occur at projectile energies on the order of a few MeV, making them easy to create in a lab setting. The reaction investigated this summer was the  $(\alpha, \gamma)$ , in which the seed nucleus captures an  $\alpha$  particle and emits  $\gamma$  radiation. In my work this summer, I investigated 19 reactions relevant for the  $p$ -process; the targets considered are given in Table 1.

**Table 1** – Table of the 19  $p$ -process isotopes addressed in this report.

Atomic (Proton) Number, $Z$	Elemental Symbol, $X$	Mass Number, $A$ (Isotope)	
32	Ge	70	
40	Zr	91	
42	Mo	92	94
44	Ru	96	
47	Ag	107	
48	Cd	106	
49	In	113	115
50	Sn	112	118
53	I	127	
56	Ba	130	
57	La	139	
62	Sm	144	
63	Eu	151	
69	Tm	169	
70	Yb	168	
79	Au	197	

The primary goal in the current  $p$ -process investigation has been to determine the cross-section for the isotopes created in various reactions, without having to measure the cross-section for each atom individually. To achieve this goal, statistical models have been used to find averaged properties of the isotopes. This method works particularly well for heavy nuclei that have deeper potential wells and more excited states, because there are more nuclear levels to include in the model [4]. Statistical models require as input: (i) the alpha optical model potential (aOMP), which aids in determining characteristics of level transitions; (ii) the gamma strength function (gSF), which highlights  $\gamma$ -ray transitions between excited states within the nucleus; and (iii) the level density model (ld). In order to answer the question of how well statistical models reproduce the behavior of an  $(\alpha, \gamma)$  reaction, I used various versions of all three inputs in my theoretical calculations, and compared the achieved results with the available data compiled in the KADoNiS-p database [5]. There exist 5 separate theoretical models for aOMP and gSF respectively, while ld has 6 models; therefore, in my simulations, I tested  $5 \times 5 \times 6 = 150$

permutations of the three variables of interest. The various models are implemented in TALYS, a statistical model calculation code [6]. A detailed description of the inputs can be found in TALYS Manual.

I ran TALYS for each isotope in Table 1, to calculate cross-sections, using the possible model combinations. I then graphed cross-section versus energy using GNUPLOT [7], a command-line utility that generates plots of functions, data, and data fits. Finally, I performed a  $\chi^2$  goodness of fit test on the KADoNiS-TALYS data sets, to determine how well the theoretical data from TALYS fitted the data from KADoNiS. Data from NON-SMOKER [8] was also included in this study, for comparative analysis; the inclusion of NON-SMOKER curves proved helpful for demonstrating the validity of using the KADoNiS-TALYS package as a model for computing ( $\alpha$ ,  $\gamma$ ) reaction cross-sections.

### **Procedure:**

Most of the procedures in my study this summer were executed through a bash script I wrote to calculate the ( $\alpha$ ,  $\gamma$ ) reaction cross-sections. I began by recording the ( $\alpha$ ,  $\gamma$ ) reactions for the isotopes listed in Table 1. For example, the  $^{91}\text{Zr}(\alpha, \gamma)^{95}\text{Mo}$  reaction is of particular interest because it is crucial to explaining the production of  $^{94}\text{Mo}$ , the most puzzling p-nucleus [2]. After recording reactions, I went to KADoNiS to record energy and cross-section data. I created three data files from KADoNiS: one for the energy range of the center of mass for the target element ( $E_{c.m.}$ ), one for the cross-sections of the seed nucleus ( $\sigma$ ), and one for the cross-section errors ( $\Delta\sigma$ ). All energies were in MeV, and all cross-section data was in millibarns.

In my first project, I created a script to run TALYS. TALYS requires a list of inputs before running; therefore, I generated a file with a list of initial conditions that included:

- the **projectile** or incident particle in the reaction of interest;
- the target **element** (seed nucleus) of the reaction;

- the atomic number,  $Z$ , of the target; and
- $A$ , the atomic **mass** number (*i.e.*, the number of the isotope of interest).

For the  $^{91}\text{Zr}$  reaction, the TALYS input list appeared as

```
projectile a
element Zr
Z 40
mass 91
energy 91Zr_energy.dat
```

where “a” denotes  $\alpha$  particle, and “91Zr\_energy.dat” is the KADoNiS energy file. As the goal of each test was to run the initial values through TALYS with a different combination of the three statistical-model parameters aOMP, gSF, and ld each time, I had a section of my bash script run through the possible permutations of these models and append the following lines to the input:

```
alphaomp 1
strength 1
ldmodel 1
```

With the list above, I included ten other TALYS-specific parameters; these, however, were set to fixed values for every test reaction, so only the contents of the list above were changed for each isotope. My script continued to generate input files as it cycled through the values for alphaomp, strength, and ldmodel, until it ran through the final permutation, where “alphaomp 5”, “strength 5”, and “ldmodel 6”. In effect, 150 input files were generated for each of the isotopes in Table 1.

After creating these input files, I called TALYS and ran the files through its system. The result was 150 TALYS output files – one for each permutation of the statistical models. One of the greatest features about TALYS is that it simulates every possible nuclear reaction with the input it receives. A large part of the output files, though, are lists of cross-sections at given energy levels, and this was the part I would plot. Constrained by my investigation’s focus, I had my script pull the TALYS output data related only to the  $(\alpha, \gamma)$  reaction. In KADoNiS, theoretical data points (with error bars) are plotted for nuclear cross-sections at given energies, and a theoretical curve,

taken from the NON-SMOKER database, is plotted against these points to show the general trend of the data. I would recreate these plots, replacing the NON-SMOKER curve with TALYS curves.

For plotting, I called the GNUPLOT command-line and preset graph titles and labels. I created a loop inside GNUPLOT to move through the 150 TALYS output files and graph cross-section data versus energy; I made 30 graphs, each with five permutation curves. The cross-section data from KADoNiS was plotted as points, with error bars corresponding to  $\Delta\sigma$ . Line color indicated the model number of gSF, while line type indicated the model number of aOMP and ld. TALYS outputs were labeled in a legend using ‘aOMP-gSF-ld’ as the naming standard.

I understood that each of the three model variables contributes to the TALYS output in its own way, and so my final project was to determine if there was a permute, or set of permutes, of aOMP-gSF-ld that was closer to the KADoNiS data points than the rest. I was advised that this could best be done using a  $\chi^2$  goodness of fit test, so I returned to my bash script and made such a test. The  $\chi^2$  values necessary for my investigation were defined by the equation:

$$\chi^2 = \sum_{i=1}^N \left( \frac{\sigma_{ex,i} - \sigma_{th,i}}{\Delta\sigma_{ex,i}} \right)^2,$$

where  $N$  is the number of data points,  $\sigma_{ex,i}$  are the experimental data from KADoNiS,  $\sigma_{th,i}$  are the data which compose the TALYS curves, and  $\Delta\sigma_{ex,i}$  are the cross-section error values, also from KADoNiS. To calculate  $\chi^2$ , I called Python 3.4.3 in my bash script; I saved the results to a new data file, listing the  $\chi^2$  value next to the related aOMP-gSF-ld permute. I then reorganized this file according to  $\chi^2$  value, from least to greatest, allowing me to quickly see which permutes were closest to fitting the KADoNiS data (*i.e.*, which had the lowest  $\chi^2$  value). To clearly identify the lowest  $\chi^2$  values out of the lists for each isotope, I determined the degrees of freedom ( $df$ ) for all reactions by computing  $df = (N - 1)$ ; then, I consulted a Distribution Table for the  $\chi^2$  value

associated with each isotope's degree of freedom, for my choice of confidence level. This  $\chi^2$  value became my limit.

To explain through example, for  $^{91}\text{Zr}$ , there were 11 data points; that meant there were  $(11 - 1) = 10$  degrees of freedom in the  $^{91}\text{Zr}$  data range. I chose to look for the  $^{91}\text{Zr}$   $\chi^2$  values corresponding to a 95.0% confidence level. This means that there is only 5% chance that I could find a model that works better than the given one. The  $\chi^2$  value associated with a 95.0% confidence level, for 10 degrees of freedom, is  $\chi^2_{950} = 3.940$ . This then was my limit: I only looked for the  $^{91}\text{Zr}$  permutes that had  $\chi^2 \leq 3.940$ .

### **Results:**

The 7 TALYS permutes with  $\chi^2$  values in the 95.0% confidence level for the  $^{91}\text{Zr}$  ( $\alpha, \gamma$ ) reaction are plotted in Figure 2. A portion of the NON-SMOKER theory curve for the same isotope and energy range is included in the graph, as well. This was done to compare the KADoNiS-TALYS package to NON-SMOKER, which has been used for many years as the theoretical standard in  $p$ -process NS modeling. Table 2 gives the  $\chi^2$  values for these  $^{91}\text{Zr}$  permutes in the 95.0% confidence level.

Due to fairly large differences between  $\sigma_{ex,i}$  and  $\sigma_{th,i}$ , the majority of the  $\chi^2$  values I calculated from the TALYS output data were on the order of  $10^2 - 10^3$ . The  $^{91}\text{Zr}$  reaction, in fact, had the best test results of all 19 isotopes considered. The lowest  $^{91}\text{Zr}$   $\chi^2$  value was 1.60641, as Table 2 shows. From my calculations, four of the first eight permutes for the  $^{91}\text{Zr}$  reaction had aOMP = 2, while four had aOMP = 4; and the first two permutes with the lowest  $\chi^2$  values both had aOMP = 2 and gSF = 3. Unfortunately, there was no such pattern apparent in the tests for the other 18 isotopes.

**Table 2** –  $\chi^2$  values of the KADoNiS-TALYS permutes in the 95.0% confidence level for the  $^{91}\text{Zr}$  isotope. Recall that  $\chi^2_{950} = 3.940$  for  $df = 10$ .

Permute (aOMP-gSF-ld)	$\chi^2$
2-3-2	1.60641
2-3-4	2.23698
4-5-2	2.65050
4-5-3	3.44975
2-4-2	3.65264
4-2-6	3.71466
2-4-4	3.74720

The lowest  $\chi^2$  values for the other isotopes considered were all below the 1.00% confidence level, which was disappointing. What this suggests, however, is that the permutations in Table 2 might be a set of suitable models special to a particular mass region, centered around the  $^{91}\text{Zr}$  seed nucleus.

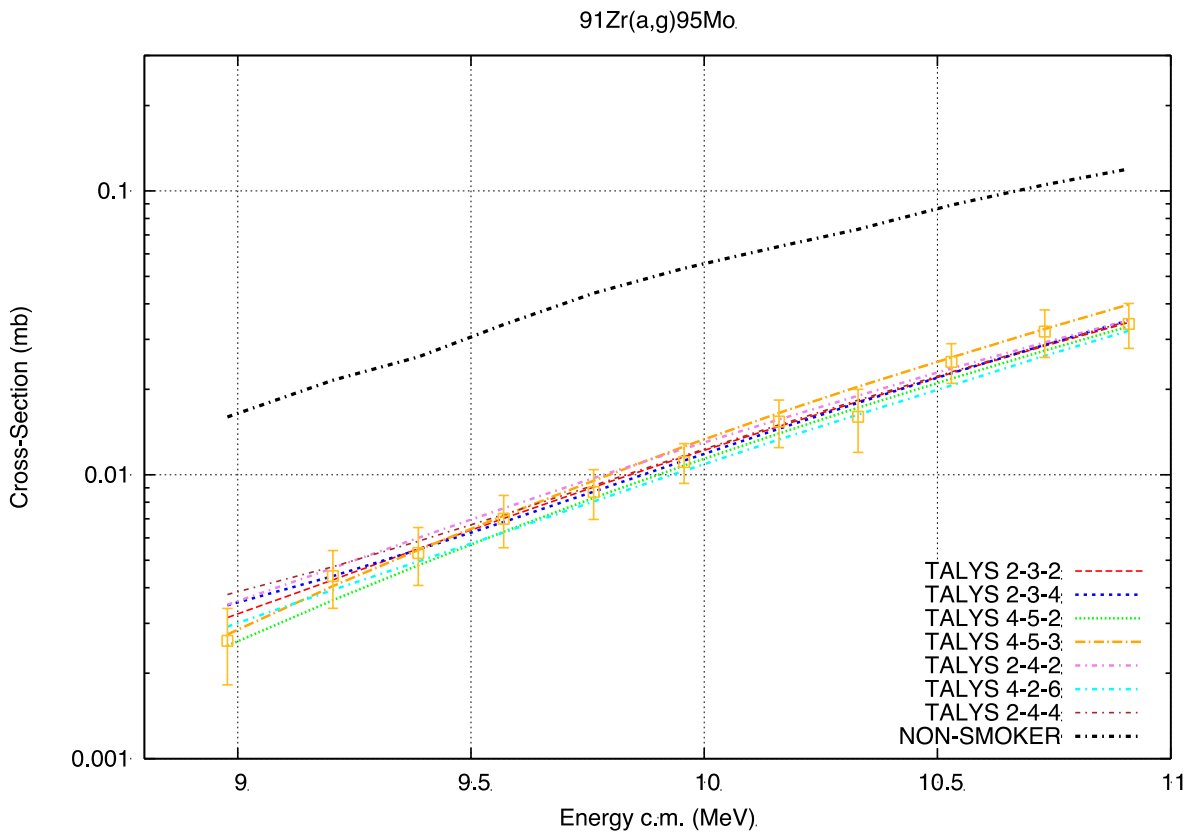


**Figure 2** – NON-SMOKER and the KADoNiS-TALYS package,  $^{91}\text{Zr}(\alpha, \gamma)^{95}\text{Mo}$ . KADoNiS data is represented by data points with error bars.

**Conclusion:** Only further investigation will lead to a more conclusive understanding of the virtues and shortcomings of the KADoNiS-TALYS package. From here, this package could be used to test other reactions in the  $p$ -process model. If it can be shown that TALYS provides accurate theoretical models for the remainder of the  $\gamma$  photodisintegration series, for example, or for any of the other proposed mechanisms of  $p$ -nuclei NS, then perhaps TALYS can become a new standard for theoretical modeling in the overall  $p$ -process study. Certainly in light of the results plotted in Figure 2, it is clear that the KADoNiS-TALYS package is at least superior to NON-SMOKER for the  $^{91}\text{Zr}(\alpha, \gamma)$  reaction. For now, though, it seems fair to conclude in total that using TALYS in union with the KADoNiS database is at least a step towards a better method for cross-section computation in the  $p$ -process investigation.

---

#### References:

- [1] W. Rapp, J. Görres, M. Wiescher, H. Schatz, & F. Käppeler. “Sensitivity of  $p$ -process nucleosynthesis to nuclear reaction rates in a  $25M_{\odot}$  supernova model”. *Astrophys. J.*, 653: 474–489, 2006.
- [2] M. Arnould & M. Rayet. “Nuclear reactions in astrophysics”. *Ann. Phys. Fr.*, 15: 183–254, 1990.
- [3] M. Arnould & S. Goriely. “The  $p$ -process of stellar nucleosynthesis: astrophysics and nuclear physics status”. *Physics Reports*, 384: 1–84, 2003.
- [4] S. V. Harissopulos. “Cross-section measurements of proton captures relevant to the  $p$ -process nucleosynthesis”. *Proceedings of the 3<sup>rd</sup> International Balkan School on Nuclear Physics (Thessaloniki, Greece, September 2002)*, 349–381, 2002.
- [5] Karlsruhe Astrophysical Database of Nucleosynthesis in Stars (KADoNiS). <http://kadonis.org/pprocess/index.php>, 2015.
- [6] TALYS. <http://www.talys.eu/>, 2015.
- [7] GNUPLOT. <http://www.GNUPLOT.info/>, 2015.
- [8] NON-SMOKER. <http://nucaastro.org/nonsmoker.html>, 2015.

Physics List Comparisons for the  
Deep Underground Neutrino Experiment

Alison Peisker

2015 NSF/REU Program  
Physics Department, University of Notre Dame

Advisor: Professor John LoSecco

## **Abstract**

Neutrinos are the most abundant particles in the universe, but scientists know the least about them. The Deep Underground Neutrino Experiment (DUNE) is an experiment that will be carried out at Fermilab whose purpose is to help physicists gain a better understanding of neutrinos. The neutrinos will travel eight hundred miles underground from Fermilab to the Sanford Underground Research Facility so that physicists can answer some fundamental questions about these small particles. This summer I studied the effects of three different physics lists on the neutrino flux at the far detector. A physics list contains the code used to model the interactions between particles. These studies were done using various tools such as ROOT, Geant4, and the Fermilab Grid to run simulations and plot the results. I determined that there is a significant difference between physics lists for both the neutrino and the antineutrino flux at the far detector. This implies that physicists will need to take the physics list into consideration when running future simulations and analyzing the data of this experiment.

## **Physics of Neutrinos**

Neutrinos are leptons that have no electrical charge and very little mass. They rarely interact with other particles, but when they do, they only interact by the weak interaction. They come from the sun, supernovae, other celestial objects, and are also products of beta decay. Neutrinos come in three different flavors: the muon neutrino, the electron neutrino, and the tau neutrino. Muon neutrinos are the most common of the three types in the Deep Underground Neutrino Experiment. The observation that neutrinos can change from one type to another and the discovery that they have mass contradict the Standard Model, which gives physicists the motivation to study these mysterious particles.

## The Experiment

The Deep Underground Neutrino Experiment (DUNE), formerly known as the Long Baseline Neutrino Experiment (LBNE), seeks to reveal some of the fundamental properties of neutrinos. The overall goals of this experiment are to determine the neutrino mass, to explain the asymmetry of matter and anti-matter in the universe, to look for proton decay, and to learn about the dynamics of supernovae explosions.

Fermilab's proton accelerator will produce a proton beam that will be collided with a graphite target. This will produce pions and kaons, which are sent into a tunnel that is 680 feet long where they then decay into neutrinos. A near detector will measure the composition of this neutrino beam as it leaves Fermilab. Figure 1 shows a schematic of the neutrinos as they are produced and sent out to South Dakota.

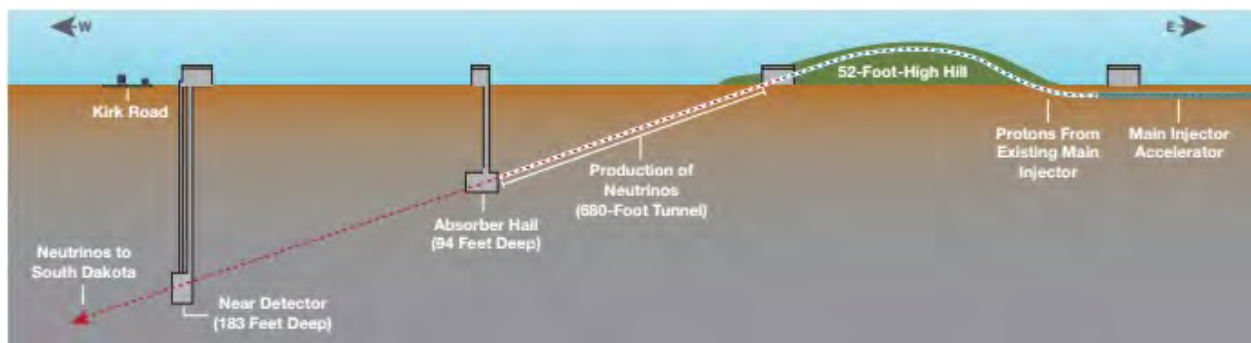


**Figure 1:** The production of the neutrino beam at Fermilab. This shows the acceleration of protons from the main injector over a hill, the production of neutrinos in the tunnel, and the path of the neutrinos through the near detector as they are sent out to South Dakota.

The neutrinos will travel 800 miles (1300 km) from Fermilab in Batavia, Illinois, to the Sanford Underground Research Facility in Lead, South Dakota, where they will be measured by

the far detector. There is no need for a tunnel since the neutrinos can travel right through the earth. The far detector is a Liquid Argon Time-Projection Chamber, and will contain 40,000 metric tons of liquid argon. Since neutrinos rarely interact with matter, the far detector must contain a lot of matter and the experiment will be run for at least a decade in order to obtain enough interactions to study. The near detector will be placed 183 feet underground, and the far detector will be placed 4850 feet underground, so that there will be no background noise from cosmic rays. Figure 2 shows the path of the neutrinos starting from the protons and Fermilab and ending at the far detector in South Dakota.

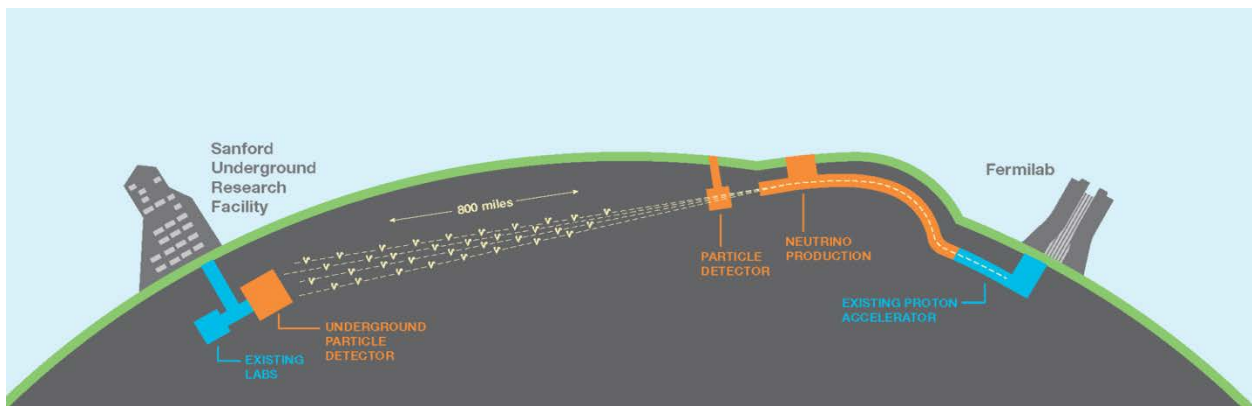


**Figure 2:** Schematic of the Deep Underground Neutrino Experiment. This shows the components of the apparatus and the path that the neutrinos travel.

## Physics Lists

A physics list is a component of the Geant4 toolkit that contains the code that models the interactions between particles. The Geant4 toolkit provides several reference physics lists that are updated with each new release. The choice of physics list made by the user depends on the detail of the physics modeling and the CPU performance desired. This summer, I compared three of these reference physics lists; I looked at QGSP\_BERT, FTFP\_BERT, and LHEP.

The physics list QGSP\_BERT is the default list that is currently being used in the Deep Underground Neutrino Experiment. It applies the quark gluon string model to model interactions of protons, neutrons, pions, and kaons above 20 GeV. It uses the Bertini cascade for hadrons below about 10 GeV, and it uses low energy parameterized models in between 10 and 20 GeV.

The physics list FTFP\_BERT uses the Fritiof model for interactions of hadrons above 5 GeV, and it uses the Bertini-style cascade for hadrons below 5 GeV. It is currently recommended by Geant4 for high energy physics experiments.

The LHEP physics list uses a combination of low energy parameterized and high energy parameterized hadronic models. It is designed to reproduce shower shapes and high energy behavior. In terms of CPU, this is the fastest of the reference physics lists since it conserves energy and momentum on average instead of on an event-by-event basis.

## **Process**

In order to study the differences between the three physics lists, I used the tools G4LBNE, the Fermilab grid, and ROOT. I ran the input macro file through the program G4LBNE using the Fermilab grid, and analyzed the results using ROOT.

G4LBNE is a Geant4 based simulation software specialized for the LBNE (now DUNE) experiment. It takes a macro file as its input and outputs a root file. The macro file contains information about the neutrino beamline such as its geometry, the initial proton energy, and the number of events. The output file contains all the data obtained from running G4LBNE.

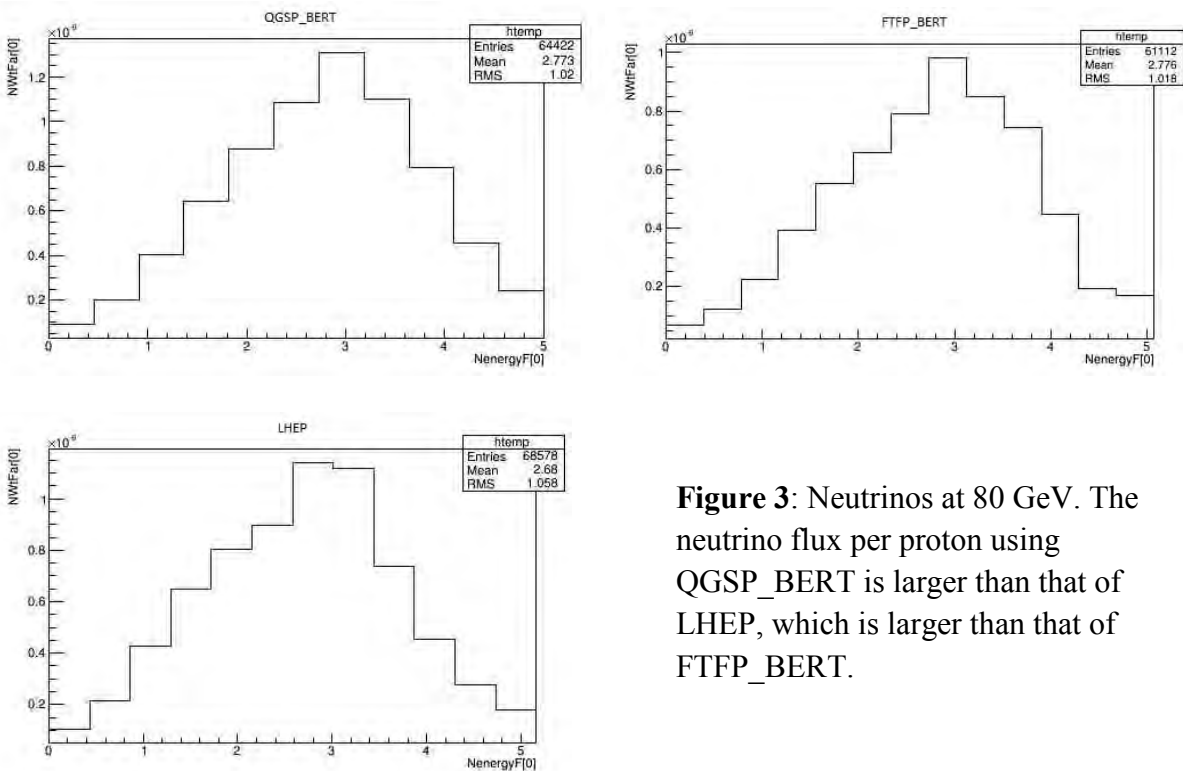
The Fermilab grid is used to submit and run many jobs at higher speeds and with greater statistics. ROOT is the program used to read the data contained in the output file from G4LBNE and to plot the results.

## Comparison of Physics Lists

The geometry of the neutrino beamline was held constant throughout all of the runs performed. First I studied the differences between physics lists for neutrinos produced from protons at 80 GeV and then 120 GeV, and then I looked at the antineutrinos produced from protons at both 80 GeV and 120 GeV.

The following graphs represent the unoscillated neutrino flux per proton through the far detector. The neutrino flux at the far detector is an extrapolation from the near detector flux and does not account for neutrino oscillation. On the x-axis is the energy of the neutrinos at the far detector and on the y-axis is the weights, or the probability that a neutrino will hit the detector.

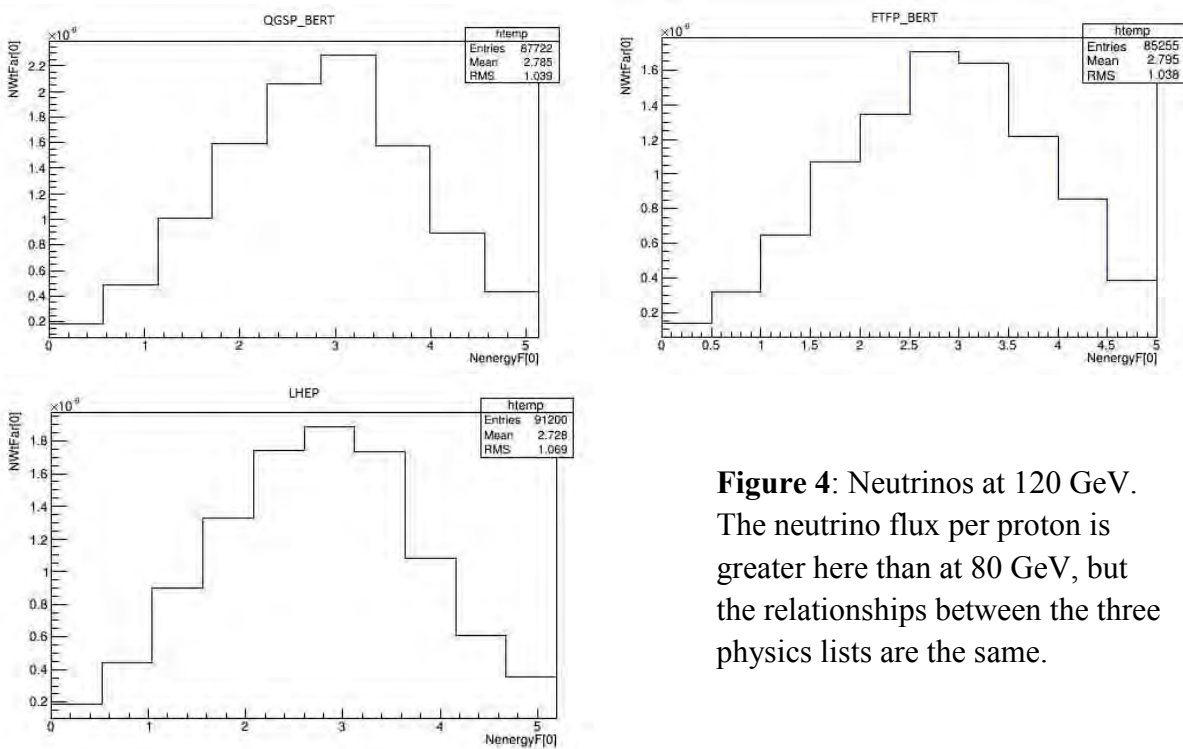
Figure 3 shows the neutrino fluxes per proton at 80 GeV for the three physics lists. The plots look similar at a first glance, but the y-axis is different. There is a 20% difference between QGSP\_BERT and FTFP\_BERT, and a 10% difference between QGSP\_BERT and LHEP.



**Figure 3:** Neutrinos at 80 GeV. The neutrino flux per proton using QGSP\_BERT is larger than that of LHEP, which is larger than that of FTFP\_BERT.

When comparing the neutrino fluxes per proton between the two different energies, it is important to take a correction factor into consideration. Since there are more protons produced per unit time at 120 GeV than at 80 GeV, there are 1.34 times as many protons at 120 GeV than at 80 GeV in a given unit of time. This signifies that all of these plots represent the neutrino flux per centimeter squared per proton and not the neutrino flux per centimeter squared per unit time.

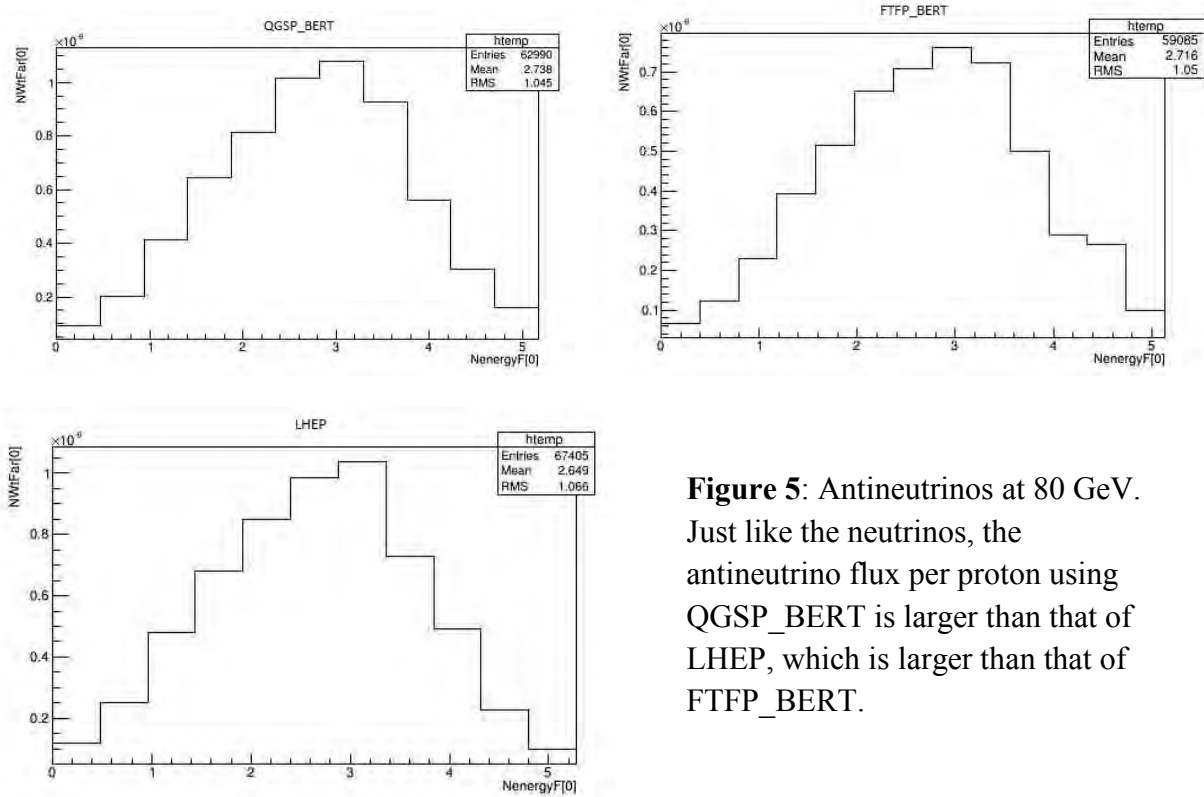
There is a greater flux per proton of neutrinos at higher energies than at lower energies, but the systematic differences between the fluxes per proton produced using the three different physics lists are the same. The neutrino flux per proton produced from 120 GeV protons for the three physics lists is shown in Figure 4.



**Figure 4:** Neutrinos at 120 GeV. The neutrino flux per proton is greater here than at 80 GeV, but the relationships between the three physics lists are the same.

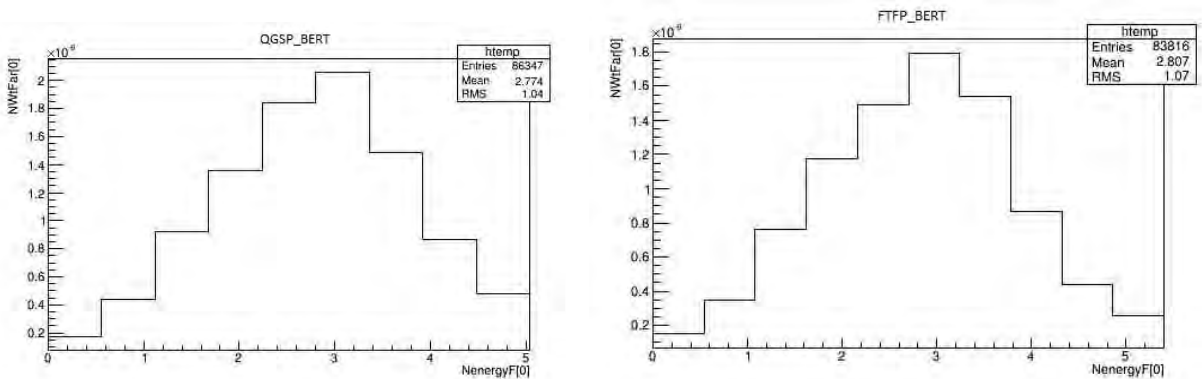
The antineutrino beam is produced by changing the sign of the horn current. This changes the direction of the magnetic field and thus selects the negative pions. Again, it is important to observe the variation in the y-axis of these plots. There is a 27% difference between QGSP\_BERT and FTFP\_BERT, and a smaller difference of 13% between QGSP\_BERT and

LHEP. The differences between the lists for the antineutrino flux per proton is greater than that of the neutrino flux per proton. The antineutrino flux per proton produced from 80 GeV protons is shown in Figure 5, and from 120 GeV protons is shown in Figure 6.



**Figure 5:** Antineutrinos at 80 GeV. Just like the neutrinos, the antineutrino flux per proton using QGSP\_BERT is larger than that of LHEP, which is larger than that of FTFP\_BERT.

Similar to the neutrinos, the antineutrino flux is also greater at higher energies, but still with the same differences between physics lists. Again, the antineutrino flux is the flux per proton produced and not per unit time, so there will be a correction factor here as well.



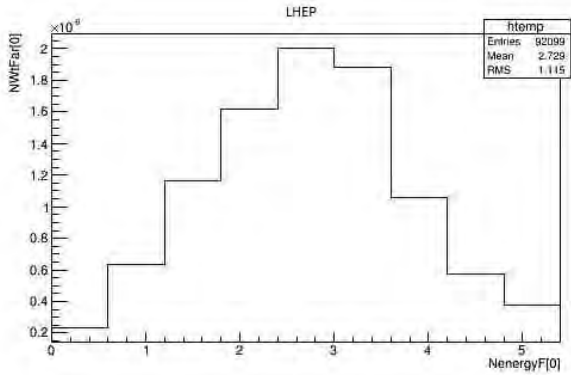


**Figure 6:** Antineutrinos at 120 GeV. As was the case for the neutrinos, the antineutrino flux per proton is greater at this higher energy but the systematic differences between the physics lists are the same.

## Conclusions

Based on my studies of the three different physics lists, there is a significant difference between the models being used in this experiment to simulate the interactions between the particles. The physics list being currently used, QGSP\_BERT provides the results with the optimal flux through the far detector. It could be a potential problem to run the simulations that produce the optimal flux because it may not be the most accurate physics model to use. This means that when the experiment is actually run, the results may not be as great as scientists' expectations from running these simulations. Therefore, it is important for the physicists working on this experiment to consider the choice of physics list when running future simulations.

## Future Work

The next step in this process would be to run the output fluxes from G4LBNE through Fast Monte Carlo. This is a program that simulates the measured energy and momentum of each final-state particle. It produces sensitivity plots so that physicists can study the sensitivity to charge parity (CP) violation.

## Acknowledgements

Thanks to my advisor Professor John LoSecco for all of the advice and guidance he provided me throughout the summer. Also many thanks goes to Professor Tom Junk at Fermilab for assisting me in the process of obtaining a Fermilab account and accessing the program ROOT from my Fermilab account. I appreciate all the help Professor Daniel Cherdack at Colorado State University gave me by helping me install and attempt to run the Fast Monte Carlo program. Thanks to the National Science Foundation for providing funding for my research and making my project possible. Finally, thanks to the University of Notre Dame and Dr. Garg for hosting me this summer and providing me with the opportunity to conduct this research project.

## References

- “Deep Underground Neutrino Experiment.” *DUNE Science*. 2015. <[www.dunescience.org](http://www.dunescience.org)>.
- “Deep Underground Neutrino Experiment (DUNE).” *Our Science*. Brookhaven National Laboratory. <<https://www.bnl.gov/science/DUNE.php>>.
- Heavy, Anne, et al. “About the Long Baseline Neutrino Facility and Deep Underground Neutrino Experiment.” Fermilab. June 2015.
- Kopp, Sacha E. “Accelerator Neutrino Beams.” Department of Physics, University of Texas at Austin. 14 Sept. 2006.
- “Neutrino Division.” *Fermilab*. U.S. Department of Energy, 15 July 2015. <[neutrino.fnal.gov](http://neutrino.fnal.gov)>.
- “Neutrinos.” *Science*. Fermilab, 15 July 2015. <[www.fnal.gov/pub/science/particle-physics/experiments/neutrinos.html](http://www.fnal.gov/pub/science/particle-physics/experiments/neutrinos.html)>.
- “Neutrinos.” *The Particle Adventure*. Berkeley Lab. <[www.particleadventure.org/neutrinos](http://www.particleadventure.org/neutrinos)>.
- “Reference Physics Lists.” Geant 4, 27 March 2013. <[http://geant4.web.cern.ch/geant4/support/proc\\_mod\\_catalog/physics\\_lists/referencePL.shtml](http://geant4.web.cern.ch/geant4/support/proc_mod_catalog/physics_lists/referencePL.shtml)>.
- Wright, Dennis. “A Short Guide to Choosing a Physics List.” Jefferson Lab. 13 July 2012.
- Wright, Dennis. “LHEP Physics List.” SLAC National Accelerator Laboratory, 16 May 2007.

# Measuring Magnetic and Electrical Properties of Ferromagnetic Semiconductors

Cesar Perez

2015 NSF/REU Program

Physics Department, University of Notre Dame

Advisors:

Dr.J.K.Furdyna

Dr.X.Liu

## Abstract

Molecular Beam Epitaxy (MBE) was used to grow ferromagnetic semiconductors under ideal conditions. The magnetic and electrical properties of the diluted magnetic semiconductor alloys were then measured. Magneto measurements were done using a SQUID machine made by Quantum Design. Electric transport was used to measure electric properties, which uses the principles of the Hall effect. Observations from these measurements show that higher concentrations of Mn in (001) GaAs lead to higher magnetization, which in turn leads to higher Curie temperatures and affects other properties of the semiconductor.

## 1 Introduction

Diluted magnetic alloys are an interest in research due to their technological applications. Semiconductors are essential to integrated circuits and are the root of modern technology. Non-volatile memory such as Hard Disk Drives (HDD) are intrinsic to standard computing. Ferromagnetic semiconductors are a step towards combining the powers of circuits and memory into one device, making them incredibly advantageous. Molecular Beam Epitaxy (MBE) provides optimal growing conditions to make the needed diluted alloys. The epitaxial growth allows for ideal non-equilibrium deposits, which layer any atoms or molecules one mono-layer at a time. The standard substrates used in these experiments are (001) GaAs. Magnetic properties are measured using a Superconducting Quantum Interference Device (SQUID). SQUID applies the Josephson effect, and uses parallel Josephson junctions attached to a superconducting ring. SQUID is highly sensitive and can detect very faint changes in magnetic flux. Electric measurements are done using the Hall effect and anomalous Hall effect. Electric measurements typically involve calculating Hall resistance, longitudinal resistance, and resistivity of any given sample.

## 2 MBE Technique

Molecular Beam Epitaxy (MBE) is the standard fabrication method of growing thin films on substrates. The molecular beam in this case is the unidirectional flow of atoms, and epitaxy is the growth of one crystal layer on another, and each epitaxial layer mimics the one beneath it. The MBE process is non-equilibrium growth that allows films to grow in ways not found in nature. Semiconductor films can be deposited on a substrate one atomic layer at a time, achieving a structure of high crystalline perfection and an arbitrary compositional profile. Growing films one mono-layer at a time gives the advantage of being able to make thin film structures such as quantum wells, superlattices, and semiconductor devices. MBE effusion cells, on the left hand side of Fig.1 contain group III and group V elements used for III-V alloy research. The III-V system and II-VI are inter-connected by an ultra high vacuum (UHV) transfer chamber. This allows the transfer of wafers without exposure to atmosphere. Molecular beams are achieved from thermally evaporated elemental sources in a cell made of pyrolytic boron nitride (PBN). Vapor escapes the effusion cell and forms a well collimated beam, which then travels ballistically through the UHV without collision. This allows for the molecular beams to deposit on a substrate, to form an epitaxial layer, at a relatively slow rate in UHV conditions. In the MBE process, good crystalline quality of the deposited films are obtained by an appropriate adjustment of the growth conditions, such as the flux of the molecular beam and the wafer temperature. Growth rates are usually 1 mono-layer per second, which is ideal for control over lattice positions. This makes control of the temperature of effusion cells and substrate essential to MBE. The substrates used for this project are GaAs (001). The substrate is adhesively stuck on a Molybdenum (Mo) block with Indium, giving adequate thermal contact. The substrate is rotated with a frequency approximately 1 Hz to achieve uniform crystal quality across the wafer surface.

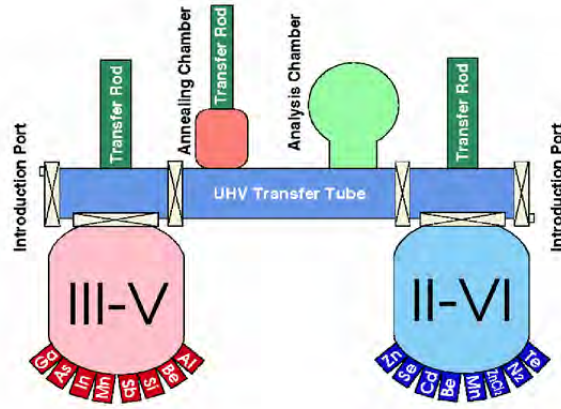


Figure 1: MBE schematic for growth of III-V and II-VI alloys

### 3 SQUID

A Superconductive Quantum Interference Device (SQUID) is used for magnetic measurements of ferromagnetic semiconductors; in particular  $Ga_{1-x}Mn_xAs$ . The main use of SQUID is to determine hard and easy axes of magnetization, the Curie temperature, the coercive field, and other magnetic properties (Fig.2).

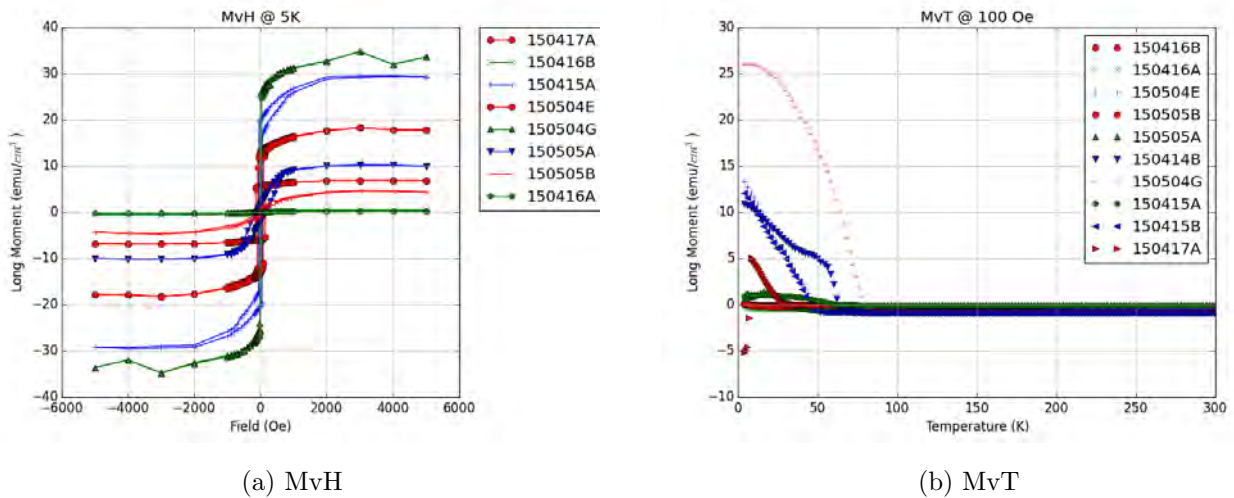


Figure 2: (a) Graph of magnetization versus applied field, which is used to determine saturation and coercive fields, (b) graph of magnetization versus temperature: used to determine Curie temperature of samples.

The magnetometer works on the dc Josephson effect, which takes advantage of the tun-

neling effect of electron pairs between superconductor-nonsuperconductor-superconductor pairs. SQUID uses a superconducting ring with two parallel Josephson junctions. When a dc magnetic field is applied through the ring, the wavelength of the cooper pairs taking the other path is decreased; further, when the two currents rejoin they will generally have different phases.

Magnetic Property Measurement System (MPMS) model XL, from Quantum Design, has the capability of measuring a sample's magnetic moment as small as  $10^{-9}$  emu. The system has rapid precision measurement over the range of 1.9 to 400 Kelvin, and the superconducting magnet provides a field ranging from -7.0 to +7.0 Tesla with 0.1 Gauss resolution. As the sample is moved through the superconducting coils, it induces an electric current in the detection coils which detect any change in magnetic flux. In addition, SQUID voltages are proportional to magnetic moment of the sample.

Sample	Temperature (K)	Coercivity (Oe)	Saturation (Oe)	Curie Temperature (K)
150415B	5	$\sim \pm 90.5$	$\sim \pm 2000$	$\sim 50$
	300	$\sim -1450, \sim -195$	$-5000, \sim -3050$	
150415A	5	$\sim \pm 50.6$	$\sim \pm 2000$	$\sim 70$
	300	$\sim -213, \sim -197$	$\pm 5000$	
150414B	5	$\sim -34.7, 50$	$\sim \pm 3000$	$\sim 80$
	300	$\sim -218, \sim -194$	$-5000, \sim -3000$	
150504E	5	$\sim \pm 89.5$	$\sim \pm 2000$	$\sim 60$
	300	$\sim -331.6, 173$	N/A	
150504G	5	$\sim -10.5, \sim -24$	$\sim \pm 1200$	$\sim 90$
	300	$\sim -152, \sim -116$	$\sim \pm 4000$	
150505A	5	$\sim -135.5, \sim -137.5$	$\sim \pm 2000$	$\sim 70$
	300	$\sim -113, \sim -116$	N/A	
150505B	5	$\sim -71, \sim -73$	$\sim \pm 3050$	$\sim 80$
	300	$\sim -68, \sim -64$	$\sim \pm 3000$	
150416A	5	$\sim -77, \sim -65.4$	$\sim \pm 3000$	$\sim 35$
150416B	5	$\sim -5.4, \sim -8.4$	$\sim \pm 2000$	$\sim 35$
150417A	5	$\sim \pm 150$	$\sim \pm 1000$	$\sim 34$

Table 1: Magnetic properties of different samples measured with SQUID.

## 4 Transport

Electric properties of  $Ga_{1-x}Mn_xAs$  are measured using the Hall effect, which is used to determine carrier concentration, carrier type, resistivity, and etc. \*A magnetic field is applied perpendicular to the direction of current flow, which in turn produces an electric field perpendicular to both the magnetic field and current. A rectangular sample with thickness  $d$  and width  $w$ , has a current  $I$  applied along the long axis and the magnetic field along the  $z$ -direction. A Lorentz force is experienced in the  $y$ -direction. There is no net force in the  $y$ -direction due to no current flow in that direction. The electric field is derived as  $E_y = Bv_x = BI/qwdn$ . Where  $B$  is the applied magnetic field,  $v$  is the drift velocity,  $I$  is the current,  $q$  is the charge of an electron, and  $n$  is the carrier concentration. The electric field in the  $y$ -direction produces the Hall voltage given as,  $V_H = wE_y$

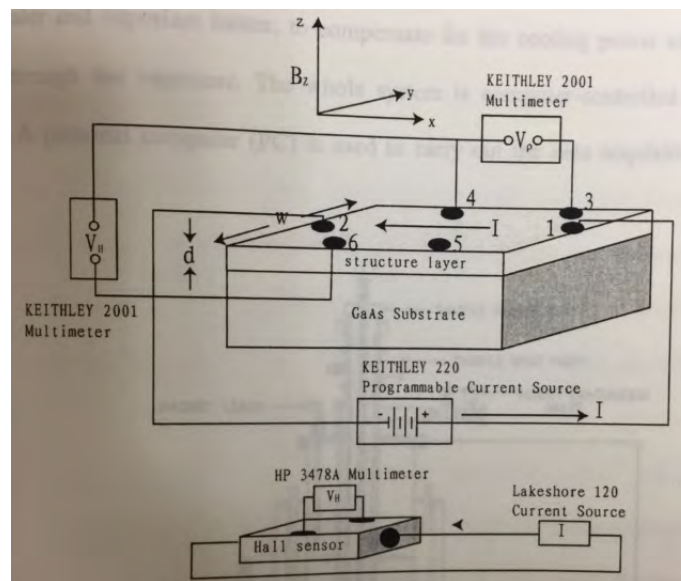


Figure 3: Schematic for basic Hall measurements. A bar shape sample is mounted with thickness  $d$ , and width  $w$ . Six contacts are made on the sample as shown. For measurement the current,  $I_{12}$  and Voltage,  $V_{3,4}$  along are used to measure resistivity along with other properties of each sample.

Six contacts are made on the rectangular sample and gold wires are attached to each of the contacts soldered with Indium. A current labeled as  $I_{12}$  is sent along the long axis of the sample, where subscript 12 states "between contacts 1 and 2." A voltage,  $V_{34}$  is measured,

which contacts 3 and 4 are at a distance  $l$  apart, which allows us to calculate the resistivity as  $\rho = V_{34}dw/I_{12}l$

Anomalous Hall effect depends directly on the magnetization of the material, and is often larger than the Hall effect. The anomalous contribution is often seen as proportional to the magnetization of the sample and becomes constant once the magnetization has reached its saturation value. The anomalous Hall effect is a scattering technique that distributes electrons based on their spin, in which the magnetization of the sample changes their angular momentum.

## 5 Effects of Growth Parameters

Low temperature MBE (LT-MBE) is used to grow GaMnAs, in which strong non-equilibrium growth conditions allow larger amounts of Mn atoms to be incorporated into GaAs. After growing a GaAs buffer layer on (001) GaAs substrate at normal conditions, the substrate temperature  $T_s$  is cooled to  $200^\circ C - 300^\circ C$ , and a low temperature GaAs buffer is deposited to a thickness between 0-100 nm. At growth rate of  $0.8\mu/h$  different variations of Mn concentrations,  $0 \leq x \leq 0.1$ , are grown to make  $Ga_{1-x}Mn_xAs$ . Table 2 provides information on growth parameters made for measurement. Previous experimentation shows that for an increase of Mn concentration, up to  $x = 0.03$ , the transition temperature also increases. There also is suggestion that hole concentration and Curie temperature are strongly correlated. Magnetotransport measurement at various magnetic fields were done on GaMnAs. Zero-field resistivity peaks around the transition temperature as seen in Figure 5.

Sample	Growth Parameters
150414B	GaAs (001) Substrate GaAs ~ 8 min (100 nm) LT-GaAs ~ 20 s (3 nm) LT-GaMnAs ~ 240s (~50 nm) $T_{Ga}=910^{\circ}C$ ; $T_{Mn}=760^{\circ}C$
150415A	GaAs (001) Substrate GaAs ~ 8 min (100 nm) LT-GaAs ~ 20 s (3 nm) LT-GaMnAs ~ 240s (~50 nm) $T_{Ga}=915^{\circ}C$ ; $T_{Mn}=760^{\circ}C$
150415B	GaAs (001) Substrate GaAs ~ 8 min (100 nm) LT-GaAs ~ 20 s (3 nm) LT-GaMnAs ~ 480s (~50 nm) $T_{Ga}=915^{\circ}C$ ; $T_{Mn}=770^{\circ}C$
150504E	GaAs (001) Substrate GaAs ~ 8 min (100 nm) LT-GaAs ~ 20 s (3 nm) LT-GaMnAs ~ 330s (~70 nm) $T_{Ga}=910^{\circ}C$ ; $T_{Mn}=750^{\circ}C$
150504G	GaAs (001) Substrate GaAs ~ 8 min (100 nm) LT-GaAs ~ 20 s (3 nm) LT-GaMnAs ~ 330s (~70 nm) $T_{Ga}=910^{\circ}C$ ; $T_{Mn}=775^{\circ}C$

Table 2: Growth Parameters of different samples grown in MBE.

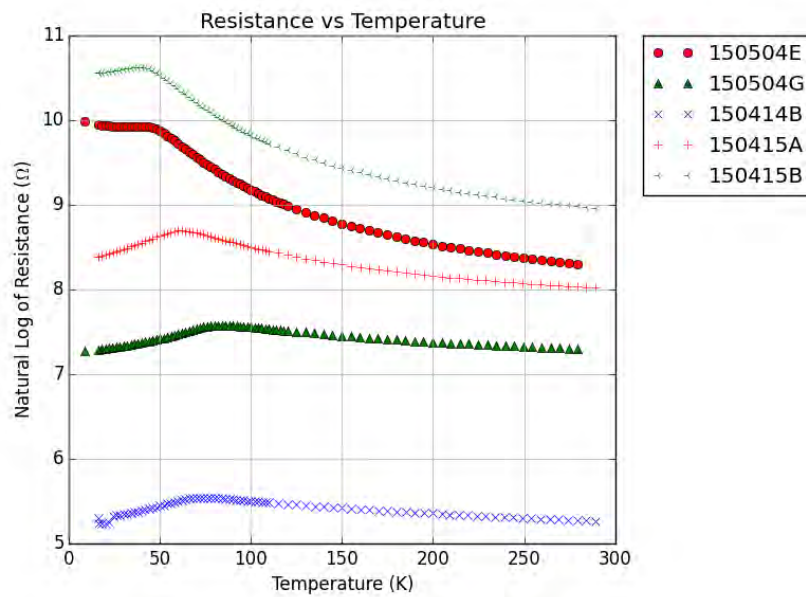
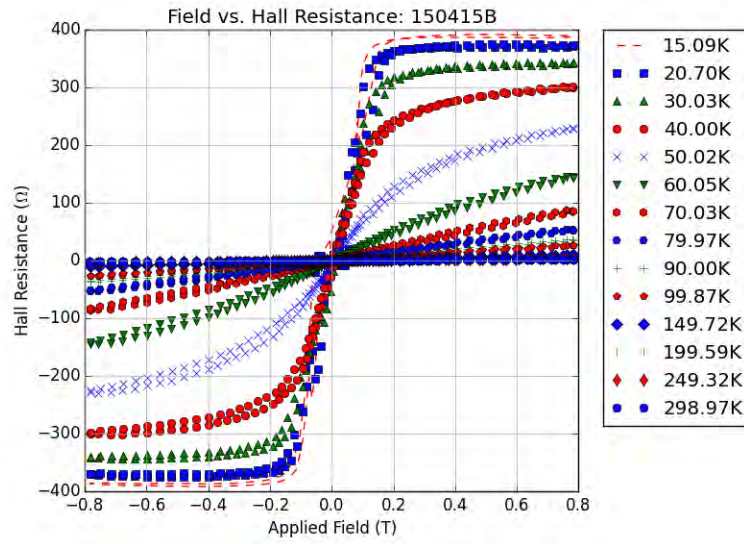
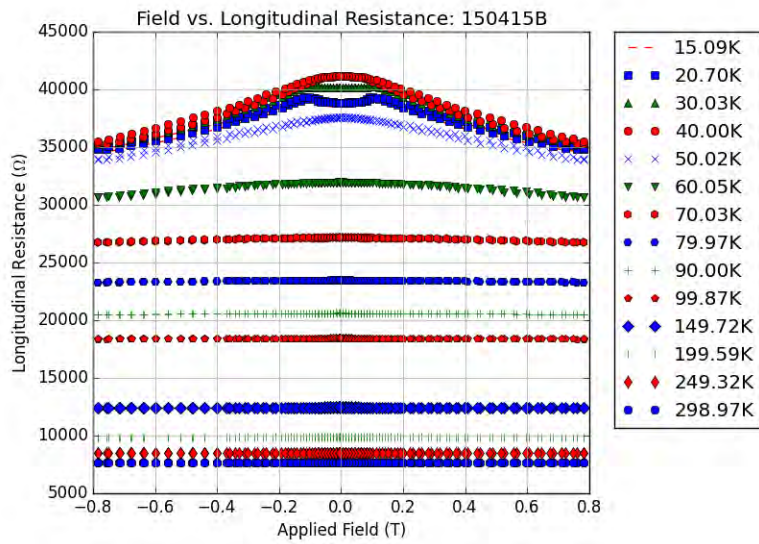


Figure 4: Logarithmic graph of resistance versus temperature.



(a) Hall Resistance



(b) Longitudinal Resistance

Figure 5: (a) Hall resistance measured at different temperatures measured against an increasing applied magnetic field, (b) longitudinal resistance also measured at different temperatures against an applied magnetic field.

## References

- [1] L.I. Maissel and R. Glang (eds.), *Handbook of Thin Film Technology*. McGraw-Hill, New York, 1970.
- [2] "On a new action of the magnet on electric currents", E.H. Hall, *Am. J. Math.*, 2, 287 (1879)
- [3] "A method of measuring specific resistivity and Hall effect of disc or arbitrary shape", L.J. Van der Pauw, *Philips Res. Rep.*, 13, 1 (1958).
- [4] B.D. Josephson, *Phy. Lett.* 1, 251 (1962). See also the articles by Josephson and Mercereau in *Superconductivity*, R.D. Parks, ed. (Dekker, New York, 1969).
- [5] J. Kossut, J.A. Gaj, *Introduction to the Physics of Diluted Magnetic Semiconductor*. Springer, Verlag Berlin Heidelberg (2010).

Statistical Mechanics of Extreme Value Statistics in  
Equilibrium and Non-equilibrium

Shangran Qiu

2015 REU Program

Physics Department, University of Notre Dame

Advisor: Dervis Can Vural

We study one novel aspect of extreme value statistics. Instead of studying the extreme value distribution of 1-D time series data, we introduce 2-D data sample with additional freedom which is spatial information in our case. Just like traditional extreme value theory(EVT), the distribution of extreme events on spatial degree, rather than merely time degree, strongly presents an invaluable potential of applications in a lot of practical situations. Our numerical work, by analyzing our mechanical toy model, reveals a strong proportional relationship between the correlation of data and distribution of extreme events on spatial degree which is independent on statistical quantities we choose.

## 1 Introduction

Extreme value theory has arisen great interests due to its broadening applications. For instance, there is a sealed box which is inflated with a mixture of oxygen and methanol gas in equilibrium condition. The maximum relative velocity of various gas molecules before collisions would be a valuable information because the possibility of explosion depends on the distribution of extremed collision velocity over the safe threshold. Fisher-Tippett theorem, the most basic theorem in traditional extreme value theory, states that the distribution of the largest or least value among a collection of  $N$  random variables generated from i.i.d (independent and identical distribution) can only be one of three types: Gumbel distribution, Frechet distribution and Weibull distribution under the limit when  $N$  goes to infinity 1. Because of its precise and also universal limiting distributions of extreme events, Extreme Value Theory(EVT) has been a curious and fascinating blend of an enormous variety of

applications involving natural phenomena such as rainfall, floods, wind gusts, air pollution, and corrosion, and delicate advanced mathematical results on point processes and regularly varying functions. Since the establishment of EVT, the steady and constant developments of EVT make it become a large branch of statistics. Right now, people desire to access the extreme properties not only the i.i.d random variables, but also the dependent and correlated data. The recent study of Brownian motion with strong correlated variables shows the general method in dealing with near extremes problems of strongly correlated variables 2.

Here, our work is still in the range of extreme value statistics, but we go to a deviated routine from standard extreme value theory. In traditional extreme value theory, the quantity used to generate extreme valued sample from parent distribution, no matter by BM method or POT method, is also the independent variable of extreme value distribution. The quantity we used to pick out the extreme valued sample isn't the variable of extreme value statistics. For example, still in above example, addition to tell possibility of explosions, more interesting question is about when and where the explosion will be originated. To answer latter question, we need to know the distribution of extreme events as a function of time and space. Further more, along the river side, can we tell the possibility or distribution of extreme flood events only at specific position? The desire to answer these kinds of question, we develop this new aspect of extreme value statistics from a different view.

## 2 Model Description

In our study, we build up a toy model consisted of springs and balls aligned in 1-dimension which is a very simple disordered mechanical model. There are totally 100 balls and 99 springs connecting them. From left to right, we give every ball an integer spatial index from 1 to 100. After different initial conditions and boundary conditions are given, we solve the evolution of system by 4-order Runge-Kutta method. With information of phase space, we can conveniently access the extreme value distribution of all kinds of physical quantities, under various states of system, including equilibrium, non-equilibrium steady state, or the transiting process from non-equilibrium into equilibrium. The method of accessing the state of system, whether in equilibrium or not, is based on theory of classical canonical ensemble<sup>3</sup> which will be briefly illustrated in the next part. There is one thing needed to be noted is that we assume the springs are so long that the ball with smaller spatial index will always be at the left of that of larger index. This assumption guarantee the equation of motion doesn't change with time.

## 3 Results and Discussion

We design three experiments to illustrate the deterministic factors of distribution of extreme events on spatial index. This classical disordered system can be properly described by theory of canonical ensemble. Regardless the complex form of potential energy, merely by analyzing the distribution of momentum, can we access  $\beta$ , the factor relevant to temperature, by fitting with normal distribution because the independence of potential energy and kinetic energy parts in partition function. For

the achievement of equilibrium, we focus on isolated system with free-end boundary condition. Except for isolated systems, we also study open system with energy exchange with outside by steady adjusting the state of the 1st and the 100th balls at each time step. The driving we act at the boundary is by adjusting momentum of the balls at two ends according to the random variables of normal distribution.

From a practical view, the extreme valued events generated by POT method is more physically significant than that of BM method. Thus we merely utilize POT method to generate extreme valued sample. As I mentioned before, instead of fitting the extreme valued data with Generalized Pareto Distribution(GPD), we focus out attention on the second degree in data space, the distribution of extremes events on spatial information.

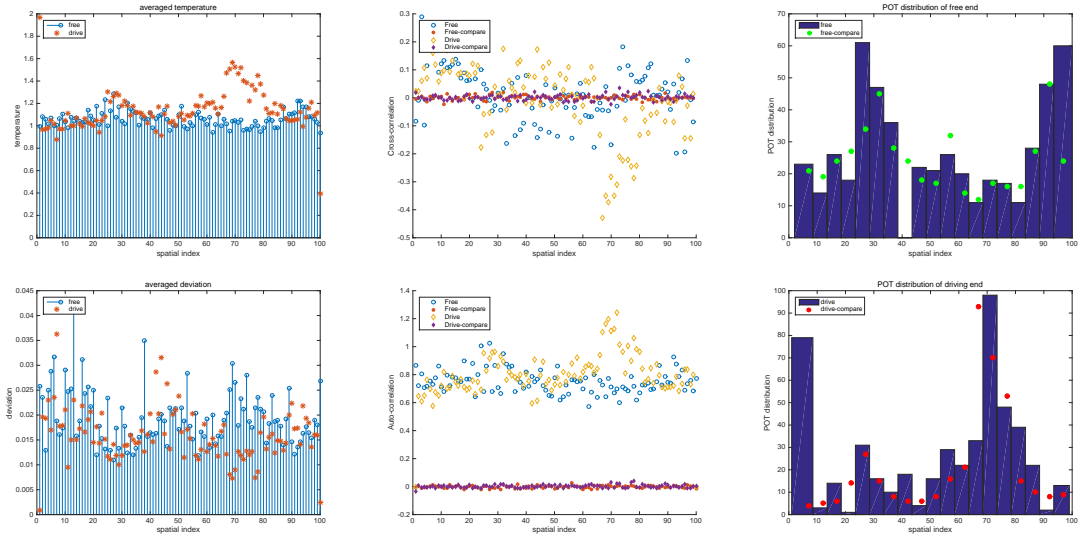


Figure 1: Experiments with uniformed spring constants

In the first series of experiments, we only consider the identical and uniformed spring constants. We firstly simulate two experiments which one with two free ends

and another one with driving ends, and then followed by another two controlled experiments respectively which will be demonstrated later. The identical spring constants in the first two experiments are the same. By adjusting the initial and boundary condition, after the systems goes to stable states, the average temperature over the whole system and over long time can be achieved roughly the same. In the following controlled experiments, we build up isolated subsystems whose temperatures are exactly the same as that of the relevant areas in original mechanical experiments. The most important difference between these two compared experiments is that the data from following controlled experiments is independent due to the generation from random variables, however the phase space data is strongly correlated. Another most important thing needs to be noted that, even through the microscopic correlation condition is different for two experiments, the macroscopic property of data from two experiments are same.

By comparing these pairs of experiments, we can access the impact purely from data's correlation on distribution of extreme events on spatial information. We give out the distribution on spatial index of two compared experiments. When we compare cases of free and driving ends, we can find that the adding of driving force both increases the temperature variance and deviation variance. Even though the intrinsic property of the system, spring constants are the same, driving boundary can still be used as a tool of stimulating more correlations, both in time correlation and space correlation. The point that there is a obvious correspondence between correlation, temperature and distribution on spatial index. When we compare the real balls and springs system and the compared experiments, we can clearly observe the differences in correlations, both in time correlation and spatial correlation. Both in

free boundary and driving boundary cases, we can observe the excellent correspondence between real mechanical system and the builded-up ideal system consisted of independent sub-systems which drives us to properly infer the effect of different correlation is eliminated by temperature variance along the spatial index.

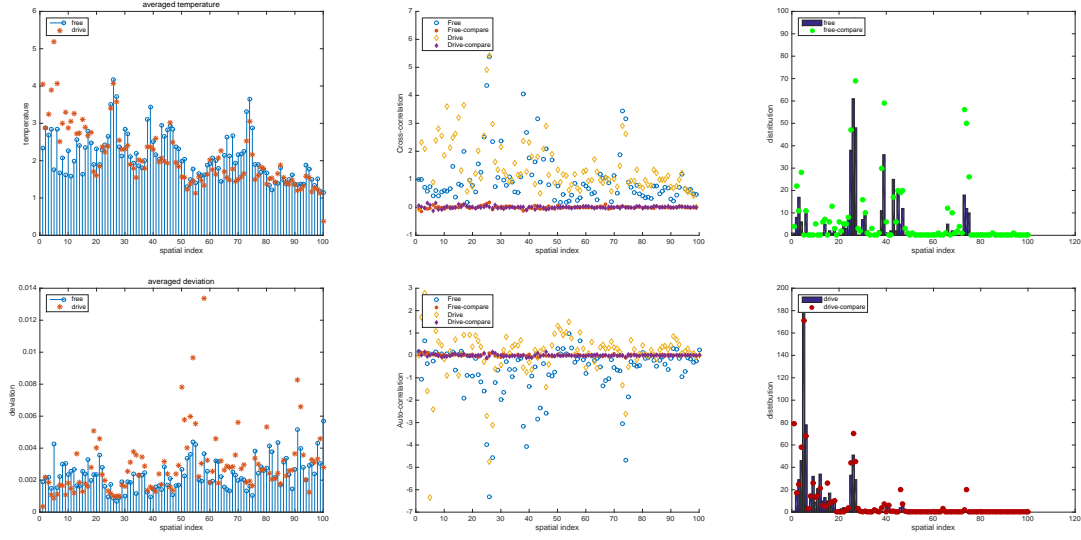


Figure 2: Experiments with random spring constants

In the second series of experiments, we study systems of randomly distributed spring constants. The difference of spring constants will of course dramatically alter the spatial correlation of data from the case of uniform spring constants. The spring constants are intrinsic properties of the system. In real world, the intrinsic properties, like the stress tensor of crust or steepness of river bed, may have the similar function as spring constants in our toy model when we apply this theory on seismic surface wave propagating along crust or water flux along river respectively. Even though these intrinsic quantities can never be distributed uniformly in practice due to the diversity of our world, the above study of uniform spring

systems is still have its theoretical benefits in the sense that right now, we can more precisely determine the influence of spring constants on the distribution, compared to the uniformed case. In figure 2, we show the same information as first figure. We still can see the driving can enhance fluctuation of temperature and deviation over systems and the similar role of correlations in the distribution on spatial index.

In the third series of experiments, we extended to other physical quantities to check whether the result of correspondence is still valid for other quantities rather than just momentum. Here we directly demonstrate the relation between correlation and distribution in figure 3 in Appendices. For example, when we study potential energy, the correlation we get is the correlation of each potential energy in 2-D sample space. And the POT sample is also picked out by judging the extreme valued potential energy and then we find out the distribution of extreme valued potential events on spatial indexes. We can clearly get that the POT extreme-valued statistical distributions of each physical quantities all have strong correspondence with the correlations of these physical quantities except for displacement. The new correlation pattern of displacement still needs more explorations.

## 4 Conclusions

We demonstrate the similarity between correlation and distribution on spatial index. In our compared experiments, the great fitness between distributions in mechanical system and isolated and independent systems shows the information of correlation has been reflected by temperature variance. Correlation variance is independent on quantities, no matter potential energy, kinetic energy or total energy.

But the correlation of displacement, which shows up a total different pattern, needs more works and attention on studying this unique correlation pattern.

## References

- [1] *Extreme Value Distributions, Theory and Application*, Samuel Kotz, Saralees Nadarajah Oct. 2000.
- [2] *Near-Extreme Statistics of Brownian Motion*, Anthony Perret, et al. Phys-RevLett.111.240601
- [3] *Statistical mechanics of classical systems*

## 5 Appendices

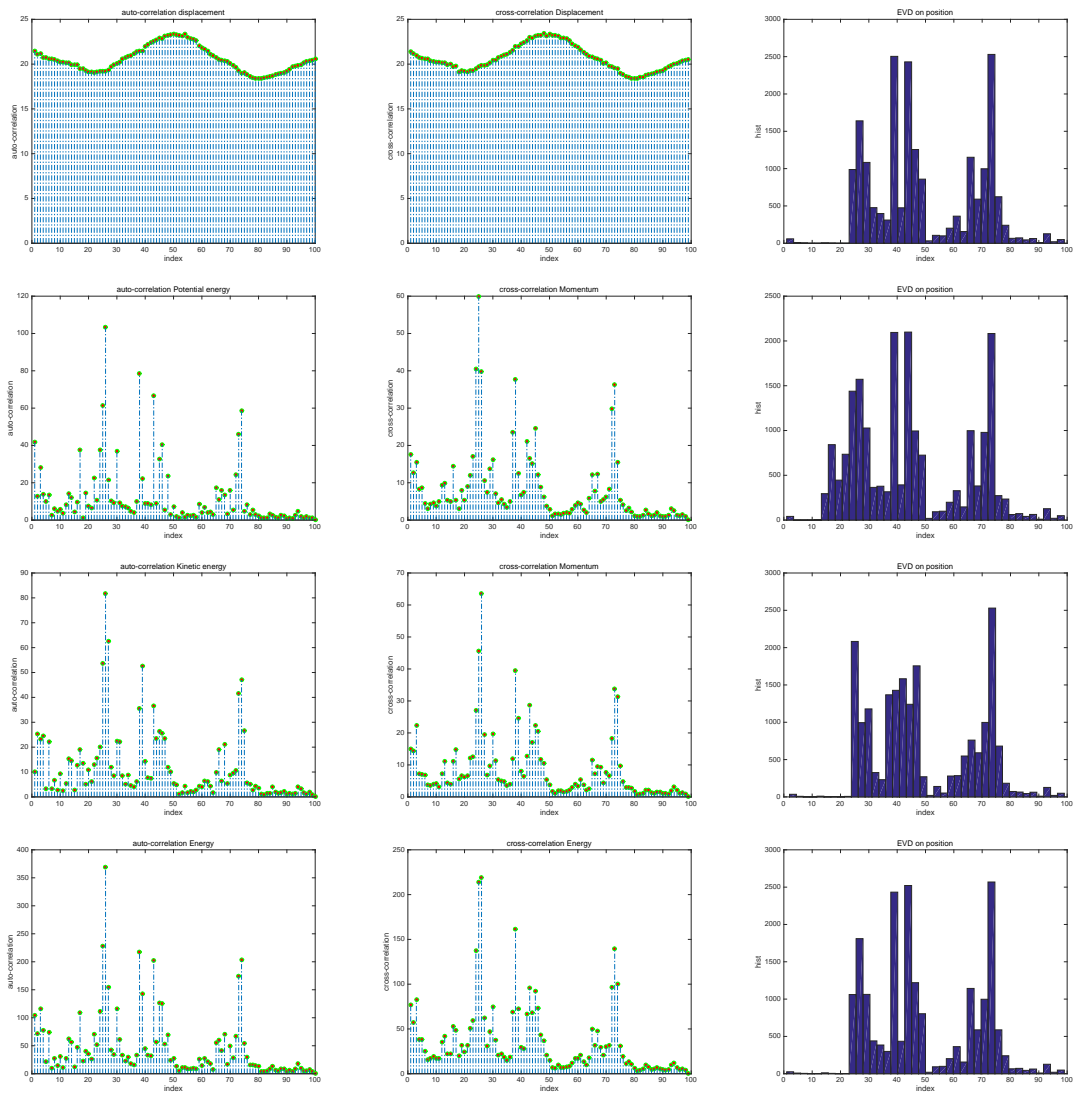


Figure 3: Extension on other physical quantities

# Atmospheric Dispersion Corrector for the iLOCATER Spectrograph

Alissa Runyon

2015 NSF/REU Program  
Department of Physics, University of Notre Dame

Advisor: Prof. Justin R. Crepp

## Abstract

As light enters the Earth's atmosphere it experiences refraction as it changes medium from vacuum to air. This causes differing wavelengths of light to disperse. As scientists seek to broaden their understanding of the universe, new techniques must be developed in order to create clear images despite the dispersion effects of the Earth's atmosphere. iLOCATER is a new diffraction limiting, planet-finding spectrograph being designed and built at the University of Notre Dame for use on the Large Binocular Telescope (LBT) in Arizona. One method of creating diffraction limited images is through the use of adaptive optics (AO), which is what iLOCATER will use. AO systems correct for the optical wavefront error caused by the Earth's atmosphere. The other primary contributor to creating diffraction-limited images is the coupling light into a tiny single mode fiber. These two methods allow for observations as if in space and eliminate modal noise, resulting in much higher resolution images. This paper discusses the design and testing of an atmospheric dispersion corrector (ADC) that will go inside iLOCATER.

## Introduction/Background:

The infrared Large binOCular Telescope Exoplanet Reconnaissance, or iLOCATER, is a new spectrograph currently being designed at the University of Notre Dame for use on the Large Binocular Telescope (LBT) in Tucson, Arizona. It works with images in the near infrared (NIR), focusing on the Y and J band which includes wavelengths from 0.95-1.33 $\mu\text{m}$ . The end goal of the project is to use iLOCATER to detect the presence of extra-solar planets orbiting within the habitable zone of nearby stars. Focus is more specifically on M-stars because their signal is brighter at NIR wavelengths and they have a habitable zone that is closer to the star so the orbital period of those planets is much shorter (on the order of tens of days as opposed to hundreds of days). While in the past spectrographs have used multimode fibers, iLOCATER will be the first of its kind to couple starlight into single mode fibers (SMF). The use of SMFs will eliminate modal noise in images entirely by getting rid of the noise introduced by changes in the interference pattern of starlight within the fiber [1].

Light refracts when it enters the Earth's atmosphere. The dispersion of different wavelengths of light occurs as a result because the index of refraction of light is wavelength dependent. This makes it harder to view objects, like planets, that are very near those stars and significantly dimmer. Light refracts at different angles depending on how off-axis the observer or object being observed is. This also affects the amount of dispersion that occurs (Fig. 1).

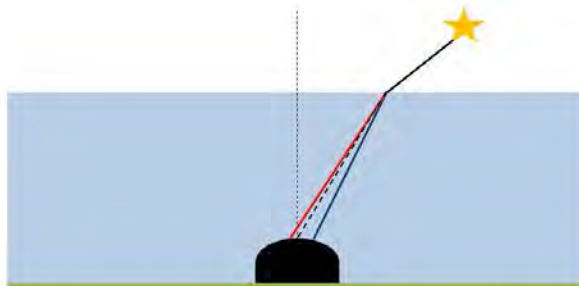


Fig. 1: Dispersed starlight as seen from telescope. Zenith is measured from vertical dotted line to angled dotted line. At every point at which light enters the atmosphere, wavelengths disperse, but at given angle we can only see a certain color of light

The more off-axis the observer is, the more of the Earth's atmosphere that the light has to travel through in order to reach them, and thus the more opportunity that it has to disperse. The amount of dispersion depends the angle from the observer that the star is at relative to the vertical. This angle, from the vertical, of the star relative to the observer is called the zenith,  $z$  (Fig. 1), and up to a certain maximum zenith the effects of dispersion are minor enough that they can be corrected for using an ADC. The maximum zenith angle is the maximum angle before the minimum and maximum wavelengths of our band can be seen separately if imaged. Our ADC design, which this paper discusses in-depth, is capable of correcting for the dispersion effects introduced by the Earth's atmosphere at a zenith of up to sixty degrees, or airmass two, with a throughput of 90% or better.

### **Theory:**

In order to correct for dispersion, it is first important to know how much dispersion needs to be corrected for. This depends directly on the zenith and can be calculated using Snell's law.

$$n_1 \sin(z) = n_2 \sin(\theta_2)$$

where  $z$  is the zenith angle,  $n_1$  and  $n_2$  are the indices of refraction of the medium that the light is exiting and entering respectively, and  $\theta_2$  is the angle at which the light exits the first medium.

When looking at light dispersing from prisms rather than from the atmosphere, the same equation is used, but with  $z$  as the wedge angle of the prism.

Due to the dispersion effects of the Earth's atmosphere, different wavelengths of light have different angles of refraction. Since dispersion is the amount that the largest and smallest wavelengths of light in the band have separated, the angular dispersion that needs to be corrected for is the difference between angle of refraction of the smallest wavelength and that of the largest wavelength of light in the band being tested. Thus, the maximum dispersion that the ADC needs to be able to correct for is relative to the angles of refraction of light at  $0.95\mu\text{m}$  and  $1.33\mu\text{m}$  when at the maximum zenith of sixty degrees. This turns out to be an angular dispersion of about 0.285 arcseconds. iLOCATER's ADC design uses a pair of round wedge prisms to correct for atmospheric dispersion. The two prisms are rotated relative to one another in order to correct for the dispersion at various zeniths. Snell's law can be used again in order to calculate the amount

that each prism rotation will correct for. When these two prisms are rotated the wedge angle of the prism will no longer suffice when using Snell's law. Instead, an equivalent prism angle must be used that accounts for total angle from both prisms. The equivalent prism angle,  $\alpha$ , can be represented by a sine curve.

$$\alpha = 2\beta \sin\left(\frac{\gamma}{2}\right)$$

where  $\beta$  is the wedge angle of a single prism, and  $\gamma$  is the relative prism angle, or total angle that the prisms have been rotated relative to their null position (which is the prism position at which light passes straight through the prism pair). From here, the angular deviation,  $\delta$ , of the beam after exiting the prisms can be found; which is the difference between the angle of refraction of the light as it exits the prisms and the equivalent prism angle.

$$\delta = \sin^{-1}\left(\frac{n(\lambda_{prism})}{n(\lambda_{air})} \sin \alpha\right) - \alpha$$

where  $n(\lambda)$  is the index of refraction of prism or air at a given wavelength, and  $\alpha$  is the equivalent prism angle. Because the prisms have some space between them, a lateral shift of the beam occurs since the light is propagating through air in that space. This lateral shift,  $L$ , relates directly to the angular deviation of the beam via the equation

$$L = d \tan \delta$$

where  $d$  is the distance between the prisms, and  $\delta$  is the angular deviation of the beam. This all needs to be taken into consideration as, upon exiting the ADC, the beam needs to be coupled into a 6.2 $\mu\text{m}$  optical diameter single mode fiber. This is extremely difficult even without a lateral shift, especially difficult with one that will change depending on zenith.

### **Experimental Setup:**

iLOCATER as a whole is a new spectrograph being designed, tested, and built for use on the Large Binocular Telescope in Arizona. It has two primary pieces, the acquisition camera and the spectrograph. Light travels from the Large Binocular Telescope Interferometer (LBTI) into the acquisition camera where the light is coupled into a single mode fiber before entering the spectrograph. The ADC is located within the acquisition camera. The purpose of the acquisition camera is to correct for dispersion and to couple the beam into a SMF.

For our purposes, when designing and building the ADC we assumed a plane-parallel atmosphere. Although the most common design for ADCs uses two prism doublets that rotate relative to each other, our ADC uses off-the-shelf components, while doublets are custom optics

[2]. The other common option is a linear ADC design. This however, also won't work for our purposes because the space required for such an ADC (on the order of 1.7m) is more than can be spared in our demonstrator system [2]. Therefore, a simple two-prism design is the best approach. All optics used in experimentation and in the final demonstrator system have a  $\lambda/10$  surface flatness. The only problem with using single prisms instead of doublets is the angular deviation of the beam that occurs as a result, part of which is corrected for by a steering mirror after the ADC. The ADC consists of two round UV fused silica wedge prisms of a 0.5 degree wedge angle and 600-1340nm broadband AR coating. These two prisms rotate relative to one another in order to correct for the dispersion at multiple zeniths. Unfortunately, dispersion can only be corrected for this way in discrete steps. Therefore, it is necessary to maximize the number of rotation steps between null and the rotation angle that corrects for maximum dispersion. This is especially important as the dispersion to be corrected for, at maximum, is only  $0.285''$ . This method will achieve the best accuracy in dispersion correction. In order to do this the wedge prisms used must have the minimum possible wedge angle. This is why the prisms for the final demonstrator system have a wedge angle of  $0.5^\circ$ . First, we used a setup that created dispersion with the prisms and imaged it at various wavelengths of visible light using a CCD in order to characterize the prisms (Fig. 2). The prisms used at this point in time were  $3^\circ 53'$  wedge angle N-BK7 prisms. This was in order to see how the spot moved on the CCD given different rotation angles.

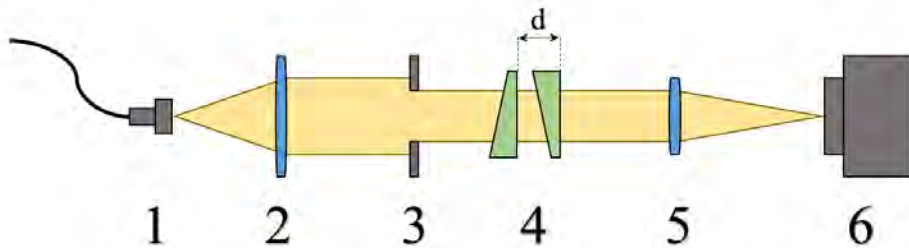


Fig. 2: Setup of dispersion creating experiment to characterize prisms. 1-Fiber, 2-Collimating lens (200mm focal length achromat), 3-Iris, 4-ADC Prisms ( $d=26.4\text{mm}$ ), 5- Focusing Lens (750mm focal length), 6-Detector.

Prisms are mounted in rotation mounts in order to determine and keep track of relative prism angle (Fig. 3).



Fig. 3: Prisms in Newport rotation stage for ease in determining relative prism angle. Distance between the two prisms is 26.4mm. Immediately behind the two prisms is a 750mm achromat focusing lens.

Experimentation was done using Newport rotation mounts, however the final system will be operated remotely using motorized rotation stages that interface with a computer program. These motorized stages will have a much smaller minimum incremental motion, allowing for improved precision. The program will allow any zenith between zero and sixty degrees to be input and will calculate the amount of dispersion to be corrected for at that given zenith. Those dispersions will correspond to a specific relative prism rotation angle and will interface with a DC servomotor that will rotate the motorized stages to the specified rotation.

The second experiment involved simulating our own atmospheric dispersion in the lab in order to correct for it using the ADC design shown in Figure 2. While  $0.5^\circ$  wedge angle UVFS prisms will be used in the ADC in the final demonstrator system of iLOCATER, this simulation, like the previous test, also used  $3^\circ 53'$  wedge angle N-BK7 prisms as that was what was available at the time. This experiment was accomplished by mounting one prism to create the dispersion, and then using the two prism rotation setup from before to correct for it. A fianium broadband source and an Omega Mauna Kea Y-band filter were used for this test. First, an image was taken with just the beam and no prisms creating or correcting for dispersion. Then, another was taken with just the dispersion creating prism. The correcting prisms were then introduced into the

system at a null position, the position at which the correcting prisms have no effect on the system, and then rotated and imaged until dispersion had been corrected for.

The final experiment involved using the broadband source and various filters to measure the dispersion of three different wavelengths of light (700nm, 980nm, and 1050nm) from a fourth wavelength (560nm). Various neutral density filters were also used to allow for properly saturated images.

**Data/Analysis:**

In the first experiment, two sets of images were taken. The first set was by increasing the relative prism angle by rotating only the front prism in two degree increments. The second set was by increasing the relative prism angle by rotating each prism in opposing one degree increments. The images from both sets were then stacked and the compilation image can be seen in Figure 4.



Fig. 4: Stacked image compilation. Curved set of dots result from rotating only the front prism in  $2^\circ$  increments. Straight line of dots is the result of rotating both prisms in opposing  $1^\circ$  increments.

As can be seen in the image compilation, rotating only one prism results in a very large angular deviation as the relative rotation angle increases. Rotating both prisms by the same total amount in opposing directions to increase the relative rotation angle however, eliminates this angular deviation only leaving a lateral shift. This second method is slightly more ideal for the ADC in the demonstrator system as we want to couple this light into a SMF and be able to correct for dispersion at multiple zeniths. This test also confirmed the  $\sin(\gamma/2)$  relationship between the relative prism angle and the equivalent prism angle as shown in Equation 2.

In the second test, an Omega Mauna Kea Y-band filter was used in conjunction with neutral density filters in order to take three sets of images using the broadband source. The first set was of the system without any prisms, the second with a single prism creating dispersion, and the third both creating dispersion and then correcting for it using the two rotating prisms. Each set of images was then compiled into a thirty image stack making it easier to see a more noticeable airy pattern. The three stacked image sets are placed side-by-side in Figure 5 including their corresponding intensity plot.

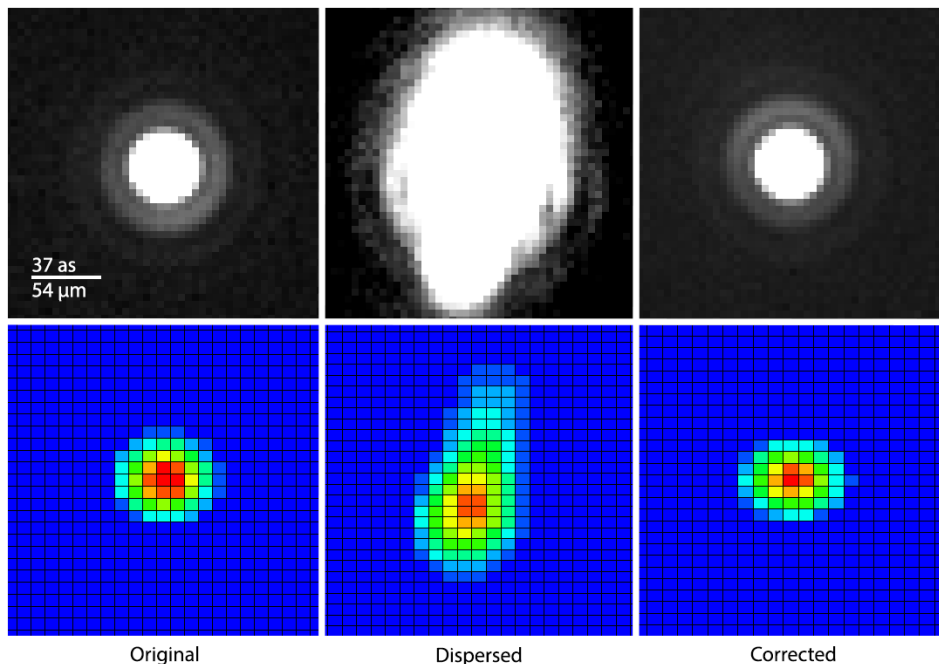


Fig. 5: Original, dispersed, and corrected images using broadband source and Omega Mauna Kea Y-band filter as imaged using Maxim DL, with their corresponding intensity plot below each image stack.

This shows the accuracy of the correcting prisms and their ability to return the images to their original state with good image quality. So it is almost like imaging the star from space without the effects of the Earth's atmosphere. It should also be noted that the dispersed image stack looks oversaturated due to shortcomings in the Maxim DL imaging program, not actual oversaturation.

The final experiment tests for the dispersion between set wavelengths of light. Images were taken at 560nm, 700nm, 980nm, and 1050nm rotating each prism in opposing one degree increments up to a total rotation angle of thirty degrees. Experimental dispersion was then compared to theory (Fig. 6). All dispersion is calculated relative to a 560nm wavelength with experimental dispersion being relative to the centroid of the image.

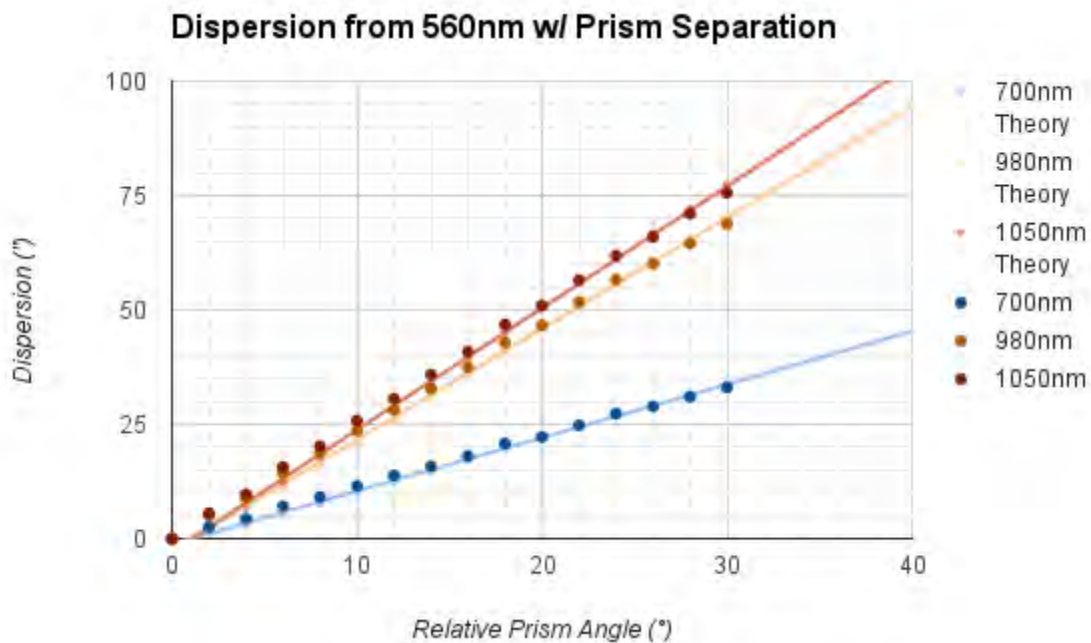


Fig. 6: Relationship between theory and experiment for dispersion relative to 560nm beam versus relative prism angle.

As anticipated, experiment matches the theory presented on pages 4-5 very well. The dispersion increases with an increased rotation angle from the null position and also as wavelength gets further from 560nm.

**Conclusion:**

The ability of iLOCATER to detect extra-solar planets orbiting nearby stars depends on a functioning ADC to correct for the dispersion effects of the Earth's atmosphere. The tests of this ADC design show that this model is well on its way to being sufficient for the demonstrator

system of the iLOCATER spectrograph. It corrects for dispersion while still producing quality images that are indistinguishable from undispersed images. However, there are still key issues that need to be fixed in order for iLOCATER to have consistently corrected images. The most significant problem that still needs to be pursued is that of lateral shift. With the current system, there is about 0.9mm of lateral shift as the prisms are rotated. This lateral shift increases with an increased relative rotation angle, which means that it increases with a larger the zenith. Since the starlight needs to be coupled into a 6.2 $\mu$ m optical diameter SMF, a change in lateral shift due to a change in zenith will result in misalignment of the beam. This would make it extremely difficult to couple light into the SMF consistently at multiple zeniths. More testing should be done in order to find a way to eliminate lateral shift when correcting for dispersion. One way this lateral shift may be fixed is by testing the system using triplets instead of two single prisms [3]. If this were successful it could remove a significant amount of the difficulty involved in coupling the light into a SMF.

**References:**

- [1] Crepp, J.R., “Improving Planet-Finding Spectrometers”. *Science*. **346**. 809-810 (2014)
- [2] Phillips, A.C. *et al.*, “The Keck-I Cassegrain Atmospheric Dispersion Corrector”. *SPIE*. **6269**. (2006)
- [3] Kopon, D. *et al.*, “Design, implementation, and on-sky performance of an advanced apochromatic triplet atmospheric dispersion corrector for the Magellan adaptive optics system and VisAO camera”. *PASP*. (2013)

# COSY Simulations to Guide Commissioning of the St. George Recoil Mass Separator

J. M. Schmitt

2015 NSF/REU Program

Department of Physics, University of Notre Dame

Advisor: Dr. Manoel Couder

## Abstract

The St. George Recoil Separator will use inverse kinematics to measure cross sections of  $(\alpha, \gamma)$  reactions relevant to stellar helium burning. St. George is designed to accept reaction products, or recoils, with energy spreads up to  $\pm 7.5\%$  and angular deviations up to  $\pm 40$  mrad. Measurements are ongoing to confirm the energy acceptance. In the near future, measurements will begin to assess the angular acceptance and beam-rejection capabilities of St. George. In order to guide the commissioning measurements and the upgrades required to complete them, several simulations were performed with the beam dynamics simulation suite COSY Infinity. The beam profile at St. George's Faraday cups was calculated in order to determine energy and angular acceptance for  ${}^4\text{He}^+$ ,  ${}^{16}\text{O}^{2+}$ , and  ${}^1\text{H}^+$ . These calculations guided the design of the Faraday cup located after the Wien filter, and they also set expectations for transmission during commissioning. Additionally, the field variation within the St. George dipole magnets was analyzed.

## 1 Introduction

The goal of St. George (STrong Gradient Electromagnetic Online Recoil separator for capture Gamma ray Experiments) is to measure  $(\alpha, \gamma)$  cross sections relevant to stellar helium burning. These cross sections are typically below a nanobarn at the astrophysical energies of interest. These low cross sections are especially challenging for typical experimental techniques that rely on  $\gamma$ -ray detection since background rates are often much higher than the expected detection rate. Reaction studies with recoil mass separators, such as St. George, do not suffer from room background and are therefore able to push to lower energies, much closer to those experienced in stellar environments [1].

Rather than bombard heavy target nuclei with light projectile nuclei, as is often done, experiments performed in inverse kinematics accelerate the heavier nuclei toward the lighter

nuclei, which serve as the target. The heavy nuclei, i.e. “beam” nuclei, generally travel unaffected though the light nuclei, the “target.” Occasionally, a beam particle reacts with the target, often at a frequency as little as 1 nucleus in  $10^{15}$  beam nuclei. The role of a recoil mass separator, such as St. George, is to separate the unreacted beam from the products [1].

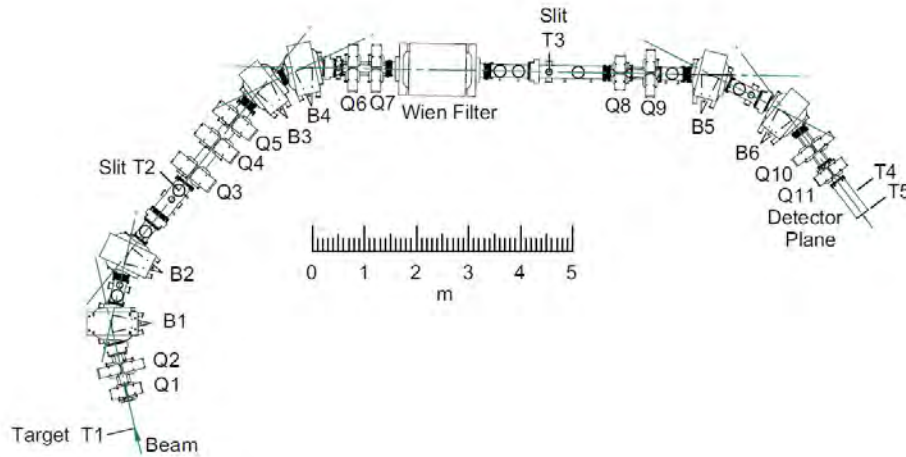


Figure 1: Schematic of St. George. Dipoles (“B”), quadrupoles (“Q”), and the Wien filter are used to separate the unreacted beam from the reaction products [1].

St. George, which is shown schematically in Figure 1, uses dipoles, quadrupoles, and a Wien filter to separate the unreacted beam and reaction products. Separation in magnetic rigidity is accomplished by the separator’s dipole magnets. The Wien filter creates a region of crossed electric and magnetic fields that only particles of a certain velocity can travel straight through. Since the dipole magnets select ions with a specific momentum over charge, this in combination with a velocity filter selects ions of a certain mass. The quadrupole magnets focus the recoil nuclei so that they stay within the confines of the separator [1].

The dipoles, quadrupoles, and Wien filter of St. George are tuned so that the recoil nuclei travel to the detector chamber at the end of the separator and the unreacted beam is rejected. Timing and energy loss detectors in the detector chamber of St. George provide particle identification information so that unreacted beam nuclei which are not rejected, so-called “leaky beam,” can be distinguished from recoils. St. George was designed to have a

beam-rejection greater than 1 part in  $10^{15}$ , with additional beam rejection provided by the detector chamber [1].

St. George was designed to accept recoils with energies in the range of  $\pm 7.5\%$  of the mean recoil energy and angular deviations in the range of  $\pm 40$  mrad from the beam axis [1]. The energy acceptance of St. George is currently being measured for  ${}^4\text{He}^+$ ,  ${}^{16}\text{O}^{2+}$ , and  ${}^1\text{H}^+$ , and the angular acceptance for these ions will be measured soon. For this REU project, several tasks were performed to help guide diagnostic upgrades to St. George and to provide calculated energy and angular acceptances that can be compared to measurements.

The following sections discuss the various tasks that were performed. Section 2 presents a new design for the Faraday cup located after the Wien filter that will intercept more of the beam at that location. Section 3 presents a complete set of energy and angular acceptance predictions based on COSY Infinity [2] simulations of St. George. Section 4 shows an analysis of the dipole magnetic fields which demonstrates a near constant profile of the field along the center horizontal axis of the magnet. Lastly, Section 5 summarizes the results of the projects and future plans for St. George.

## 2 Redesigning the Post-Wien Filter Faraday Cup

During diagnostic tests of St. George, it was found that the beam-interception capabilities of the Post-Wien filter Faraday cup, which is used to measure beam transmission after the Wien filter, were inadequate. The Faraday cup has a circular opening, but the actual beam is much taller than it is wide. The current opening is not tall enough to accept the entire beam, even for the main recoil energy and angle for which St. George is tuned.

COSY Infinity [2] simulations of St. George were used to determine the height and width of the recoils and beam at the location of the Post-Wien filter Faraday cup. For these simulations, a  ${}^4\text{He}^+$  beam was used. As shown in Figure 2, the Faraday cup is inserted

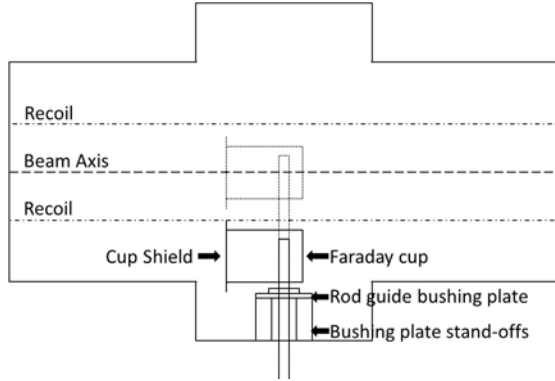


Figure 2: Faraday cup inside the beam pipe. No part of the Faraday cup can extend into the path of the recoils when it is retracted. In order to accommodate the increase in height of the Faraday cup, the height of the bushing plate stand-offs must be decreased by 0.500 in, from 2.063 in to 1.563 in.

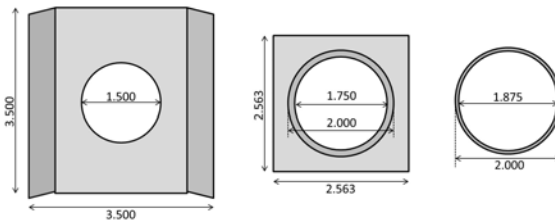


Figure 3: Original dimensions of the Faraday cup (inches). On the left is the tantalum shield that protects the suppressor and cup from the incoming beam. In the middle is the suppressor, which prevents secondary electrons from escaping and creating a false signal. On the right is the cup itself, which is made of copper.

into the beam path for transmission measurements, then retracted when measuring reaction recoils. When retracted, the cup must not block any recoils. The vertical extent of the recoils from the central axis was found to be 5.21 cm, so the top of the cup must be at least 5.21 cm below the central axis when it is retracted.

Simulations of the beam at the Post-Wien filter Faraday cup found a vertical extent of 2.28 cm from the beam axis and a horizontal extent of 0.79 cm from the beam axis; i.e. the full height and width of the beam were 4.56 cm and 1.58 cm, respectively. These dimensions determine the shape that the new Faraday cup must have to accept all of the beam.

As shown in Figure 3, the opening of the original Faraday cup, 1.500 in diameter, would not accept a beam with height 4.56 cm = 1.795 in. Thus only the height needs to be increased from 1.500 in to 2.000 in in order to accommodate the predicted beam size.

A limiting factor in this design is that the cup must be made of copper in order to provide adequate thermal dissipation since the cup is substantially heated by the incident beam nuclei. In order to minimize the cost of the new Faraday cup, a piece of rectangular

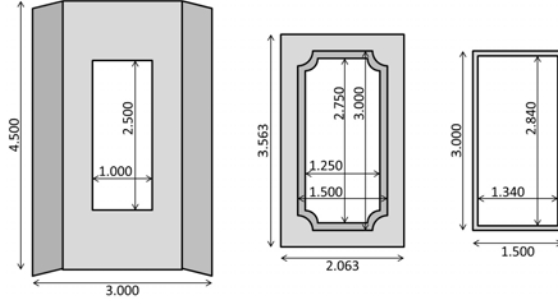


Figure 4: Dimensions (inches) of new Faraday cup using  $3.000 \times 1.500$  in waveguide. The heights are increased by 1.000 in and the widths are decreased by 0.500 in from the original design.

waveguide [3] will be used rather than custom ordering or cutting the ideal dimensions of copper. Since waveguides are typically sold in standardized sizes, the design had to be adjusted to the closest available dimensions:  $3.000 \times 1.500$  in. This results in a cup with the shape shown in Figure 4. Since the beam is expected to be 1.795 in tall and 0.622 in wide, it will still fit within the  $2.500 \times 1.000$  in opening in the shield.

However, since the Faraday cup's height would be increased by 1.000 in, its shield would then extend 0.500 in into the region of the recoil. To counteract this increase in height, the height of the bushing plate stand-offs has to be decreased by 0.500 in from 2.063 to 1.563 in, as shown in Figure 2. The thicknesses (lengths along the beam's direction) of all the pieces do not need to be changed from the original design.

### 3 Angular Acceptance Analysis

A comprehensive analysis of the energy and angular acceptance of St. George was performed using COSY simulations [2]. Building off an existing St. George simulation [1], two procedures were defined for creating beam ray traces, which are ion-optical trajectories of beam particles through the separator. Each procedure creates a series of rays in the horizontal x-direction or vertical y-direction that represents the beam shape for certain energy and angular deviations. The beam was assumed to have a diameter of 3 mm and an intrinsic spread of  $\pm 3$  mrad at the target location. Then the rays were traced through the beamline, and the extent of the beam was calculated at eight locations, shown in Figure 5.

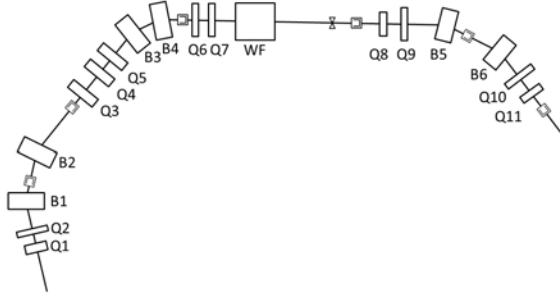


Figure 5: The eight locations at which the beam shape was calculated were at the Post-B1, Pre-Q3, Pre-Q6, Post-Wien filter, Post-B5, and target cups, and the target cup aperture and mass-slits [1].

The beam extent at the specified locations was calculated for energies between  $\pm 8\%$  of the mean ion-energy and angles between  $\pm 40$  mrad of the central axis in both directions in the plane that is perpendicular to the beam axis. Additionally, the simulation was carried out for three types of beams:  ${}^4\text{He}^+$  at 1 MeV,  ${}^{16}\text{O}^{2+}$  at 2 MeV, and  ${}^1\text{H}^+$  at 1 MeV.

The results were recorded in a spreadsheet and formatted such that the user can choose the position, energy deviation, and angular deviations, and the spreadsheet returns the horizontal and vertical beam extents at the specified location. This tool will provide a basis for comparison to the beam when performing the angular acceptance measurements.

## 4 Dipole Field Analysis

An analysis of the dipole fields was performed in order to determine if the measured dipole field at the location of the Hall probe differed significantly from the field at the beam location. The magnetic field values within the dipole magnet were provided for a grid of points defined by the axes shown in Figure 6 [4]. The axes were defined such that the “starting point” is the origin.

Python 3.3.3 [5] was used to read the magnetic field data and perform a two dimensional interpolation to find the profile of the field along the center-line of the magnet, represented by the dashed line in Figure 6. Dipoles 1-5 were analyzed at 30%, 70%, 85%, and 100% of their maximum field strength, and dipole 6 was analyzed at 70%, 85%, and 100% of its maximum field strength.

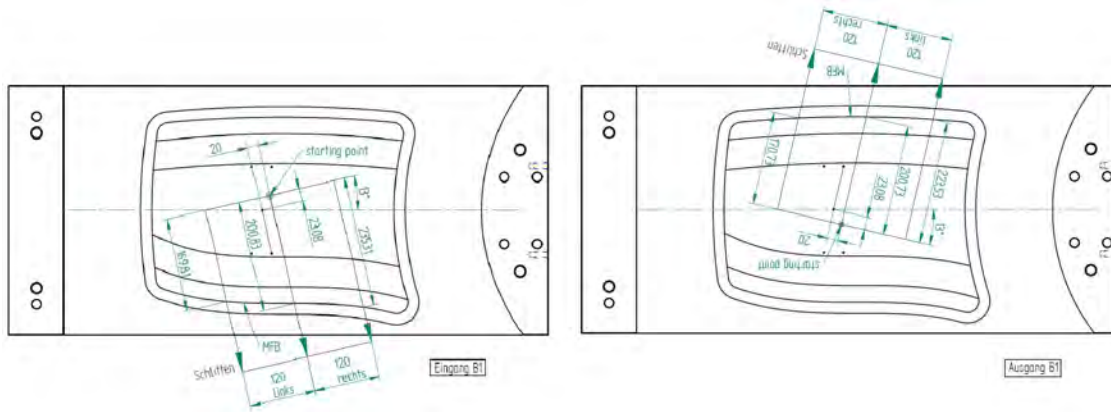


Figure 6: The left image shows the entrance, or “eingang,” field, and the right image shows the exit, or “ausgang,” field. An interpolation was performed along the dashed line through the center of the magnet to see the profile of the field along this line.

Several features of the dipole magnets were examined. The field strengths were compared at the entrance and exit of the dipole magnets. The shapes of the entrance and exit field profiles were the same, but differed by a constant amount. This is shown in Figure 7 for dipole B1 at 30% of maximum strength.

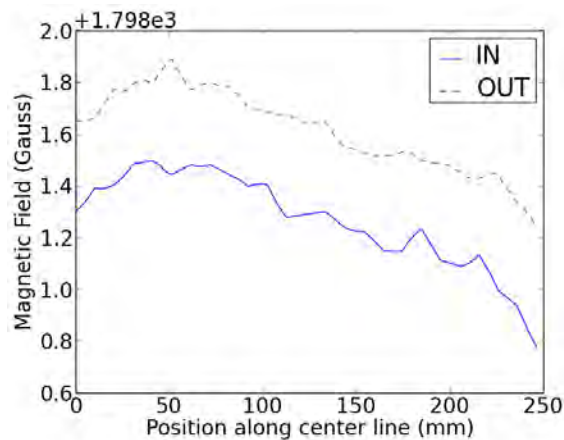


Figure 7: Comparison of the entrance and exit fields for dipole B1 at 30% of maximum strength. The profiles only differ by a constant offset.

Since the horizontal profile shapes of the entrance and exit fields were similar but differed by a constant amount, only the entrance field was used to find the profile of the field along the center-line of the magnet. This interpolation was fit with a fourth order polynomial, as

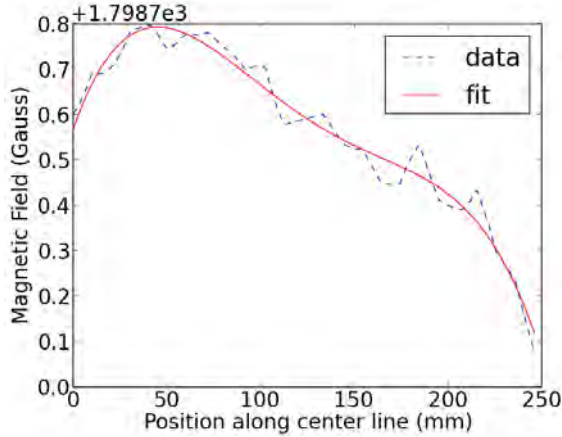


Figure 8: Entry field with a fourth order fit for dipole B1 at 30% of maximum strength.

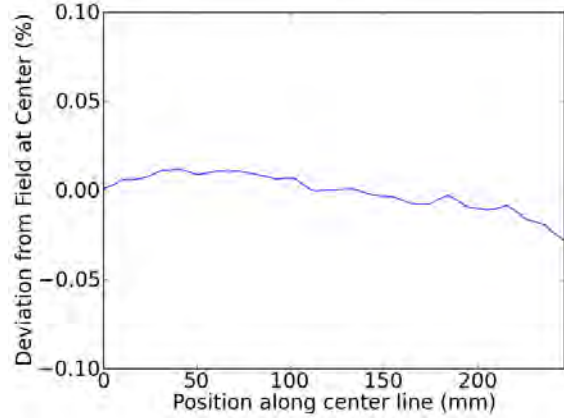


Figure 9: Deviation from the field at the reference particle center along the center-line of the dipole for dipole B1 at 30% of maximum strength.

shown in Figure 8.

Additionally, the deviation from the field at the reference particle center, the intersection of the beam path and the center-line, was examined. The deviation for dipole B1 at 30% of maximum strength is shown in Figure 9. This confirmed that the fields did not deviate more than 0.05% (1 Gauss at 30% or 3 Gauss at 100% of maximum field strength) between the reference particle center and the edge of the magnet, where the Hall probe is.

## 5 Conclusion

St. George is currently in the stage of being tested for energy acceptance at different locations throughout the beamline, where various primary beams are used to simulate reaction recoils. Several COSY simulations were performed to guide diagnostic upgrades to St. George and to provide a basis for comparison during energy and angular acceptance measurements. In order to facilitate acceptance measurements, the Post-Wien filter Faraday cup was modified to better fit the simulated shape of that beam at that location. Construction

and installation of the new Faraday cup are planned for the near future.

In addition to energy acceptance measurements, angular acceptance measurements will soon be run on St. George. An analysis of the horizontal and vertical beam extents was performed with COSY simulations for  $^4\text{He}^+$ ,  $^{16}\text{O}^{2+}$ , and  $^1\text{H}^+$  beams at eight locations for deviations from the central ion-energy of  $\pm 8\%$  and angles between  $\pm 40$  mrad in both the horizontal and vertical directions. The results were compiled in a spreadsheet-based tool that can be used to set expectations during acceptance measurements. The angular acceptance measurements will begin in the near future once the energy acceptance measurements have been completed and the additional diagnostic equipment required to simulate the angular spread of the beam has been installed.

The dipoles' magnetic fields were analyzed to determine how accurately the measurement by the Hall probe, located at the edge of the field, reflects the value of the magnetic field at the center of the magnet. It was found that the field did not vary more than 0.05% from the reference particle center to the location of the Hall probe.

## References

- [1] M. Couder *et al.*, Nucl. Instr. and Meth. A 587 , 35 (2008).
- [2] M. Berz, COSY Infinity, ([http://www.bt.pa.msu.edu/index\\_cosy.htm](http://www.bt.pa.msu.edu/index_cosy.htm)).
- [3] Penn Engineering Components, (<http://www.pennengineering.com/>).
- [4] Bruker, 2015, (<https://www.bruker.com/>).
- [5] Python Software Foundation, *Python v3.3.3 documentation*, 2013.

Numerical Simulations of the Electronic Properties of a  
Penrose Tiling Quasicrystal

Rochelle Silverman

Advisor: Professor Kenjiro Gomes

Department of Physics, University of Notre Dame

July 2015

## Abstract

Quasicrystals provide a uniquely organized aperiodic structure that contrasts those of both crystalline lattices and glassy structures and cannot be well described by band structure or other conventional solid state theories. To investigate this class of materials we plan to use atomic manipulation to create a nanoscale quasicrystal and measure its electronic properties. In preparation for this experiment, we used a tight binding model to describe a simulated, quasicrystal-inspired Penrose rhombus-patterned atomic lattice and computed the wave function of the electronic states and their energies. We used a nearest-neighbor hopping approximation, which resulted in an energy band width of  $8t$ , where  $t$  is the hopping constant, and an unanticipated highly degenerate zero-energy state. The averaged wave functions of zero-energy states are not localized to the edges or any defect, and their momentum are ill-defined. The states at low and high energy, near the edges of the band, have well-defined dispersion relations and exhibit a unique ten-fold symmetry, impossible to be obtained in crystalline materials. This information will be used for comparison with Scanning Tunneling Microscope (STM) data recorded for a similarly-structured physical lattice constructed via STM atomic manipulation.

## Introduction

Quasiperiodic crystals, or quasicrystals, were first observed in 1982 and display rotational and long-range symmetry but lack the translational symmetry required to be defined as periodic crystals. In traditional mono-atomic periodic crystals all atomic sites are strictly equivalent, meaning that unbound electrons can travel freely throughout the material. In randomly organized materials, atomic sites are not necessarily equivalent, and so electrons are mostly bound and localized. As quasicrystals lack translational symmetry, their atomic lattice sites are not strictly equivalent. The sites do however, form four, five, or six-fold rotationally symmetric probability densities creating isolated islands of high probability that

free electrons must "hop" or tunnel between to move large distances within the structure, which gives quasicrystals unique physical properties. [2, 3]

Five-fold symmetric, or pentagonal, quasicrystals are of particular interest because they are the simplest and most symmetrical quasi-crystal structures. [4] Some three-dimensional pentagonal quasicrystals are composed of two right-angle prisms with a five-fold symmetric lattice structure as the bases creating a stack of semi-periodic base structures. These compounds can be considered crystals in the stacking direction where the layered bases form columns of periodic sites, and two-dimensional quasicrystals in the base plane. This structure allows us to apply studies of the two-dimensional base to the three dimensional structure. [1] A common pentagonal quasicrystal base structure was discovered by Roger Penrose, and so is termed Penrose tiling. This structure fills two-dimensional space using two different rhombus tiles: one with vertex angles of 36 and 144 and one with vertex angles of 72 and 108. [5]

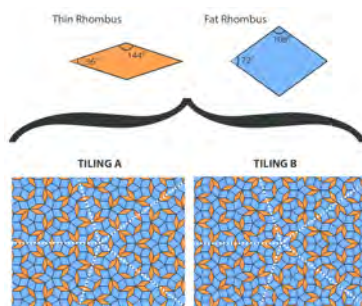


Figure 1: The thin rhombus and fat rhombus tiles fill 2D space using deflation to create two unique Penrose tiling patterns, Tiling A and Tiling B. The dotted white lines are lines of symmetry.

To create a Penrose-inspired physical lattice carbon monoxide molecules will be deposited on a smooth copper surface in a low temperature and pressure environment and then dragged across the surface to form a tiling pattern. A current is applied to the atomically fine STM probe tip to create a voltage difference between the tip and target carbon monoxide molecule. As the probe tip approaches the carbon monoxide molecule, it interacts with the molecule to create a tunneling junction that acts as a synthetic bond by which the probe tip can drag

the carbon monoxide molecule to the desired location. The current through the probe tip is turned off to release the carbon monoxide molecule.

The STM will image the arrangement of carbon monoxide molecules by measuring small current changes in the probe tip created by quantum tunneling between the tip and the surface as the tip scans over a sample. The probability density of a target site is proportional to the amount of current measured and is displayed as a point on a three dimensional surface with peaks of high-density and troughs of low-density describing the electron configuration of the sample area.

## Project Description

A tight binding model was used to describe a simulated, quasicrystal-inspired, and Penrose rhombus-patterned atomic lattice and compute some of the quantities measured by STM such as the local electronic density of states.

I first mapped the Penrose lattice using deflation of half-Penrose-rhombus triangles. Deflation describes the systematic decomposition of a polygon into smaller polygons, whose summed area is equal to that of the original shape. Penrose tiling utilizes two different rhombus tiles, one thin rhombus with angles of 36 and 144 and one fat rhombus with angles of 72 and 108. [5] Each rhombus tile can be broken into two triangles that can be treated independently with the same deflation algorithm to produce a tiling pattern of rhombuses, composed of similar triangles. The two different triangle shapes, one with a vertex angle of 36 and one with a vertex angle of 108, were distinguished and labeled by a color code of 0 or 1, respectively.

I wrote a MATLAB code to produce the coordinates of and plot a Penrose tiling pattern and compute the energy state density and momentum wave vectors of the configuration. A wheel of ten thin triangles was arranged about the origin. Each triangle was identified by three vertex points and a color code. In every second triangle, the coordinates of the two

non-36 angle vertex points were switched, so that decomposition of the triangles based on the order of vertex points would result in rhombuses across triangle edges.

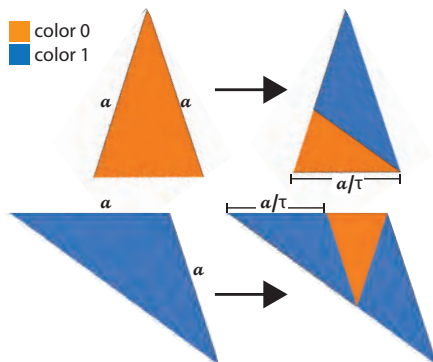


Figure 2: The two triangle shapes used to create the Penrose tiling pattern are decomposed into smaller, similar triangles. All triangles of one color are similar.

Then the decomposition rules for each type of triangle were defined. One deflation iteration decomposed each 0-colored triangle into two new triangles: one 0-colored and one 1-colored triangle, and each 1-colored triangle into three new triangles: one 0-colored and two 1-colored triangles. With each deflation iteration, the rhombuses side length decreases by a factor of the golden ratio  $\tau = \frac{1+\sqrt{5}}{2}$ .

Each odd number of deflation iterations of the original triangle wheel produces tiling pattern A and each even number of iterations produces tiling pattern B. I restricted the considered atomic sites to those within a specified radius so that I could compare analyses of the two tiling patterns. The radius was chosen so that the resulting patterns would each contain approximately 1,000 atomic sites, a sufficient sample size to minimize edge effects without being too large to create with atomic manipulation.

The corresponding physical lattice to this simulation has a carbon monoxide molecule located at the center of each rhombus tile. Because electrons in the physical lattice could not jump through the positive nucleus of a molecule, or between opposite vertices of a rhombus, I restricted the movement of free particles in the simulation between sites connected by a rhombus side.

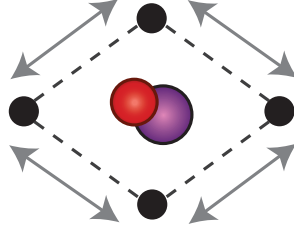


Figure 3: Illustration of a carbon monoxide molecule at the center of a rhombus tile. Hopping of free electrons is allowed only between sites along a side of the rhombus.

The Hamiltonian of the system was created according to the tight-binding model. The motion between each atomic site is described by a kinetic energy that accounts for the hopping only between sites connected by the sides of the rhombus.

The hopping constant  $t$  depends on the specifics of the material, but in broad terms it describes how easily electrons move between sites. A high  $t$  value corresponds to a large probability of hopping between sites, and a low  $t$  value corresponds to a small probability of hopping between sites. For convenience, we set the hopping constant to unit, so our energies are scaled to units of  $t$ .

This Hamiltonian results in a diagonally symmetric matrix with off diagonal term  $t$  in corresponding neighboring site. The diagonal of the matrix can be used to describe the potential energy of each atomic site. In this experiment, all atomic sites were occupied by the same type of molecule, so all energy magnitudes on the diagonal of the neighbor matrix were equal. In this case  $E_0$  scales the Hamiltonian and does not change the relative values of calculated quantities. All other matrix elements describing non-neighboring sites were defined as zero, denoting no hopping between the sites.

The Hamiltonian was numerically diagonalized and the eigenvalues and eigenvectors of the matrix were calculated. The set of eigenvalues  $E_n$  denote the magnitudes of possible energy states occupied by unbound electrons in the lattice, and the set of eigenvectors  $\Psi_n$  describe the structure's set of wave functions, one for each energy state. Together these quantities give a good description of the expected unbound electron behavior for the atomic lattice.

We can also obtain the wave function in momentum space with a simple Fourier transform as:

$$\Phi_n(k) = \int \Psi_n(r) e^{ikr} dr$$

The momentum wave functions describe the dispersion relation between energy and momentum.

## Discussion

The possible energy states  $E_n$  of the atomic structure were plotted as a histogram in fig. 4(a) for both tiling pattern A and tiling pattern B. The tiling coordinates were restricted to approximately 1,000 sites so the number of possible energies for both patterns are comparable. The histogram of both tiling patterns show an unexpected highly degenerate state at zero energy. The energy band width is approximately  $8t$ , from  $-4t$  to  $4t$ , which is the range of energies for a square lattice. However, a square lattice does not exhibit highly degenerate energies.

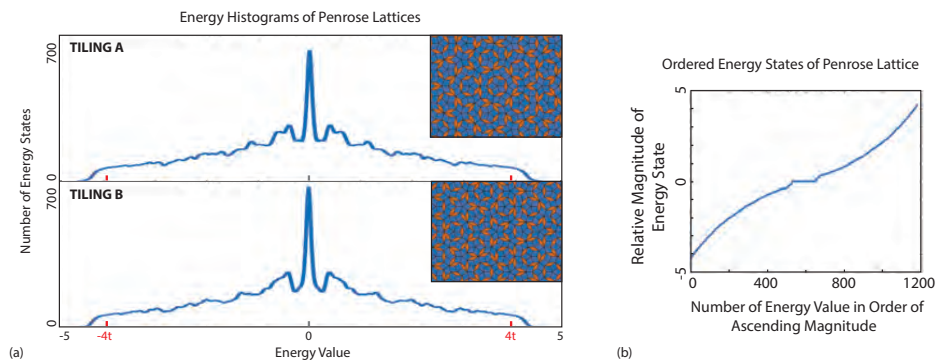


Figure 4: (a) The energy state histograms of atomic Penrose configurations are very similar for tiling pattern A and tiling pattern B. The energy band boundaries of a square lattice is marked in red on the energy value axis. (b) An alternate perspective of the histograms in 4(a) plots possible energy states from lowest to highest energy. The wide plateau at zero energy describes a highly degenerate state in both tilings.

The energy state histograms of both tiling A and B are very similar, which allows us to conclude that the findings of this simulation describe universal properties of the Penrose tiling system, and are not unique to either pattern. Figure 4(b) shows another perspective of the histograms in fig. 4(a) by plotting possible energy states in increasing order. This chart shows a relatively smooth curve with a plateau at zero energy that corresponds to the highly degenerate zero-energy state. Additionally, there are few states just above and just below this energy, which indicates a gap in possible energy states of the system.

To visualize the probability density of the zero energy states, all wave functions of these states were squared, averaged, and graphed as probability versus location in two-dimensional space. The specific patterns of the density of states for Tiling A and Tiling B are different but both exhibit similar properties. The high and low density areas plotted in fig. 5 exhibit five-fold rotational symmetry about the central low point and no periodicity. It is significant to note that highly degenerate states are usually associated with edge-state or defect localization. However, the probability density patterns of this structure are not localized; they spread over the entire real-space area of the structure suggesting that there is not a well-defined dispersion relation and therefore momentum at this energy. These zero-energy states have no kinetic energy and these probability density plots do not change with time.

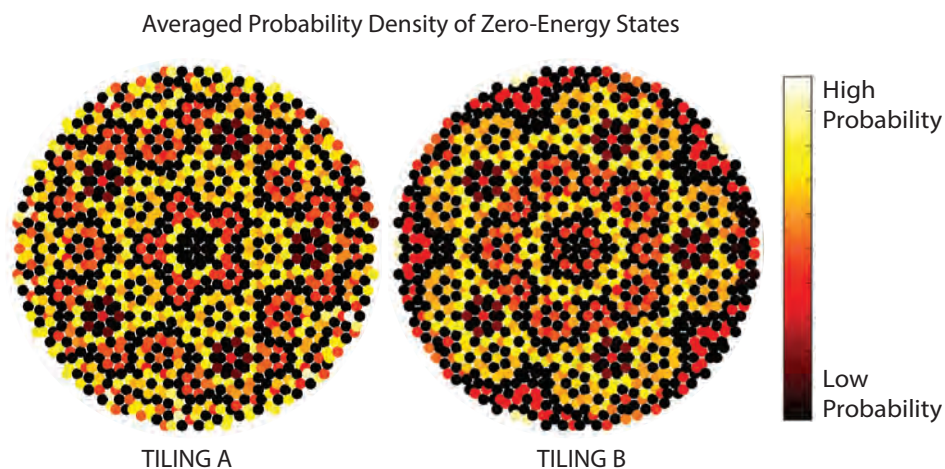


Figure 5: The averaged probability density of all zero-energy states for Penrose tiling pattern A and B both exhibit five-fold rotational symmetry and no periodicity. The color of each site indicates the probability of an electron to be located at that position.

Three examples of momentum wave vectors are shown in fig.6. At low energies, fig. 6(a), the momentum wave vectors show one well-defined ring of possible momentums. The averaged momentum wave vectors of middle energies, those near zero and shown in fig. 6(b), do not show a defined pattern. At high energies, shown in fig. 6(c), the momentum wave vectors show ten small circles of possible momentums symmetrically spaced about the origin. These high energy states have well-defined dispersion relations and exhibit a unique ten-fold symmetry, impossible to be obtained in crystalline materials.

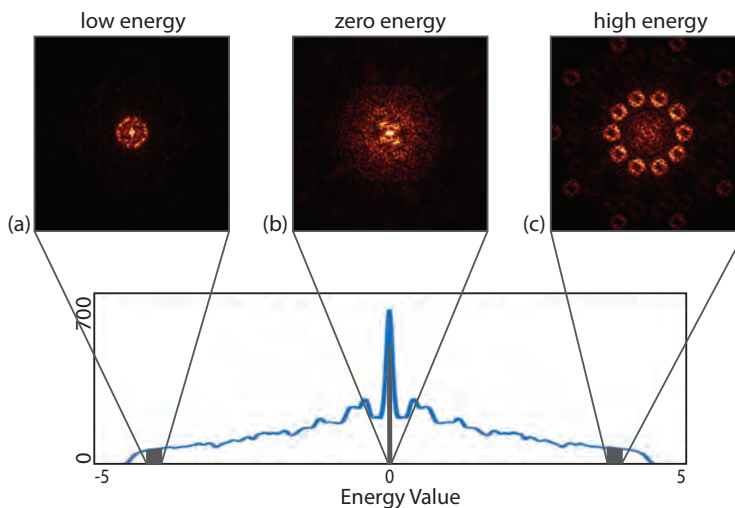


Figure 6: Three examples of momentum wave vectors averaged over twenty consecutive low energy states (left), zero-energy states (center), and high energy states (right). The plotted states are separated by location in the energy states histogram.

This simulation provides a good approximation of electronic properties of a nanoscale Penrose tiling pattern based on the tight-binding model and nearest-neighbor hopping and will help guide our studies of a similarly-structured physical lattice constructed via STM atomic manipulation. The highly degenerate zero-energy state provides an unanticipated and unexplained phenomenon to investigate.

## References

- [1] S.E. Burkov. Ground states of two-dimensional quasicrystals. *Journal of Statistical Physics*, 52(1-2):453–461, 1988.
- [2] Simon Jazbec. The properties and applications of quasicrystals. *University of Ljubljana*, 2009.
- [3] Jason Lee, Wen-Chuan Tian, Wei-Liang Wang, and Dao-Xin Yao. Two-dimensional pnictogen honeycomb lattice: Structure, on-site spin-orbit coupling and spin polarization. *Scientific Reports*, 5(11512), 2015.
- [4] Dov Levine and Paul J. Steinhardt. Quasicrystals. i. definition and structure. *Physics Review B*, 34(2), 1986.
- [5] Z. Valy Vardeny, Ajay Nahata, and Amit Agrawal. Optics of photonic quasicrystals. *Nature Photonics*, 34(2):177–187, 2013.

**Spectroscopic factors and partial proton widths of  $^{18}\text{Ne}$  levels from  
a  $^{17}\text{F}(\text{d},\text{n})^{18}\text{Ne}$  reaction study**

Yingchao Zhang<sup>1,2</sup>

2015 NSF/REU Program

Physics Department, University of Notre Dame

Advisor: Daniel W. Bardayan<sup>2\*</sup>

Contributor: Patrick O'Malley<sup>1</sup>

<sup>1</sup> *University of Notre Dame, IN, USA*

<sup>2</sup> *Xi'an Jiaotong University, Xi'an, Shaanxi, China*

## Abstract

Spectroscopic factors and single proton width of  $^{18}\text{Ne}$  for  $^{17}\text{F}$  (d,n)  $^{18}\text{Ne}$  reaction are calculated simultaneously by the computer code DWUCK4 based on distorted-wave Born approximation (DWBA) model. As reported by many authors, both spectroscopic factors and single particle width of proton vary with the selection of the optical models. However, we find that the product of them which is partial proton width remains invariant with different optical models for transfer wave input in the DWBA calculation of  $^{17}\text{F}$  (d,n)  $^{18}\text{Ne}$  reaction.

## Background

The  $^{17}\text{F}$  (p, $\gamma$ )  $^{18}\text{Ne}$  reaction plays a significant role during the novae explosion. The rate of  $^{17}\text{F}$  (p, $\gamma$ )  $^{18}\text{Ne}$  reaction is crucial to understand some very important phenomena like observed overabundance of  $^{15}\text{N}$  in novae ejecta.[1] However, the relatively low amplitude of cross section makes it very hard to realize  $^{17}\text{F}$  (p, $\gamma$ )  $^{18}\text{Ne}$  reaction in the laboratory. The cross section of  $^{17}\text{F}$  (d,n)  $^{18}\text{Ne}$  reaction is several orders of magnitude higher than  $^{17}\text{F}$  (p, $\gamma$ )  $^{18}\text{Ne}$ . Therefore, we can study the proton transfer reaction instead to extract the partial proton width of  $^{18}\text{Ne}$ . The partial proton width of  $^{18}\text{Ne}$  can be used to determine the burning rate of  $^{17}\text{F}$  (p, $\gamma$ )  $^{18}\text{Ne}$  reaction during novae explosion.

DWUCK4 is the computer code that we use to calculate the scattering and reaction observables for  $^{17}\text{F}$  (d,n)  $^{18}\text{Ne}$  reaction. For the reaction  $A(a,b)B$ , where  $a=b+x$  and  $x$  is

the transferred particle, the transition amplitude for the reaction  $A(a,b)B$  can be calculated by the following formula:

$$T = J \int d^3 r_b \int d^3 r_a \chi^{(-)}(\vec{r}_b) \langle bB | V | aA \rangle \chi^{(+)}(\vec{r}_a) \quad (1)$$

where the  $\chi^{(-)}$  and  $\chi^{(+)}$  are the incoming and outgoing distorted waves respectively.

To obtain distorted wave, radial wave equation need to be solved. The optical potential of the radial wave equation is defined as follows:

$$U(r) = Vf(x_0) + \left(\frac{\hbar}{mc}\right)^2 V_{so}(\sigma \cdot \mathbf{r}) \frac{1}{r} \frac{d}{dr} f(x_{so}) + i4W_D \frac{d}{dx_D} f(x_D) \quad (2)$$

$$f(x_i) = (1 + e^{x_i})^{-1}, \quad x_i = (r - r_i A^{1/3}) / a_i$$

The optical potentials for both initial and final distorted wave are required to input. We call them distorted wave input. However, There are several sets of parameters which are reported to fit the data well for the certain nucleus mass region. Here we use two typical deuteron optical models as shown in Table 1 for the initial distorted wave, while using two typical neutron optical models for final distorted wave.[2] Therefore, there are four different combinations for the distorted waves input. In Table 1, the optical models from i to iv are called Lohr Haeberli model (deuteron model), Perey-Perey model (deuteron model), Becchetti-Greenlees model (neutron model) and Wilmore-Hodgson model (neutron model) respectively.[2] For the initial distorted wave, deuteron models are applicable, while neutron models are applied to final distorted wave. We name the

combinations of i – iii, i – iv, ii – iii and ii – iv as model 1, 2, 3 and 4 respectively.

In formula (1),  $\langle bB|V|aA\rangle$  is the form factor. For stripping reactions, the form factor can be further expressed as follows:

$$\langle bB|V|aA\rangle = \sum_{jl} S_{jl}^{1/2} R_{jl}(r_{xA}) \langle lsm\mu - m | j\mu \rangle \langle s_b s m_b m_a - m_b | s_a m_a \rangle \times \langle J_A j M_A M_B - M_a | J_B M_B \rangle D_0 \delta(\vec{r}_x - \vec{r}_b) Y_l^{m*}(\vec{r}_{xA}) \quad (3)$$

For  $^{17}\text{F}$  (d,n)  $^{18}\text{Ne}$  reaction, proton is striped from the deuteron and transferred to  $^{17}\text{F}$  to form  $^{18}\text{Ne}$ . Formula (3) involves in the physical quantities such as coordinate of transferred proton. Therefore, the optical model for the proton transfer wave is also required to input to calculate the form factor. We call this as transfer wave input.

## Results

In our simulation, the initial beam is  $^{17}\text{F}$  which is on ground state ( $\frac{5}{2}^+$ ). The target is made out of deuteron. We study the outgoing  $^{18}\text{Ne}$  on  $1^-$  excited state. The level scheme of  $^{18}\text{Ne}$  is shown in fig.1. Since the energy of  $1^-$  state of  $^{18}\text{Ne}$  is higher than that of single particle state  $^{17}\text{F}+p$ . The generated  $^{18}\text{Ne}$  on  $1^-$ -excited state can than decay and emit proton again, which is related to partial proton width. The beam energy is 7.05 MeV in the center mass frame. At that low energy, the interactions between nuclei show dominant resonance characteristics. Using a simple model of resonant reactions, the cross-section can be described as follows:

$$\sigma \propto \frac{\Gamma_p \Gamma}{(E - E_r)^2 + (\frac{1}{2}\Gamma)^2} \quad (4)$$

Where  $\Gamma_p$  is the partial proton width of  $^{18}\text{Ne}$ , while  $\Gamma$  is the total width of  $^{18}\text{Ne}$ . The value of  $\Gamma$  of  $^{18}\text{Ne}$  is easy to be determined by measuring the half life time. However, for the  $^{17}\text{F} (p,\gamma) ^{18}\text{Ne}$  reaction  $\Gamma_p$  is very hard to measure due to the very low amplitude of the cross-section. The partial proton width is determined by the structure of  $^{18}\text{Ne}$ . The channel to form  $^{18}\text{Ne}$  does not impact the partial proton width. Therefore, we go over to measure the  $^{17}\text{F} (d,n) ^{18}\text{Ne}$  reaction in order to get partial proton width. However, partial proton width cannot be measured directly. To obtain the partial proton width, spectroscopic factor is required according to the following relation:

$$\Gamma_p = C^2 S \Gamma_{s.p.} \quad (5)$$

Where  $C^2 S$  is the spectroscopic factor, while  $\Gamma_{s.p.}$  is the width for single particle state  $^{17}\text{F}+p$ .  $\Gamma_{s.p.}$  can be calculated by DWUCK4, whose value depend on the selection of optical models. The spectroscopic factor can be extracted from the differential cross section data according to following relation:

$$\frac{d\sigma_{ex.}}{d\Omega} = C^2 S \sigma_{DWBA} \quad (6)$$

$\frac{d\sigma_{ex.}}{d\Omega}$  is the experimental differential cross section data.  $\sigma_{DWBA}$  is the differential cross section obtained through DWBA method calculation. Since the ambiguities of optical parameters, the amplitude of calculated differential cross section can vary at a large range, which gives quite arbitrary spectroscopic factor. DWUCK4 can calculate single particle width and spectroscopic factor simultaneously. The values of both of them will be influenced by the parameters ambiguities. However, as the partial width is the product of

spectroscopic factor and single particle width, there is the possibility that the effects of ambiguities can be counteracted after multiplying them. We figure out a method below to explore the possibility based on optical models shown in Table 1.

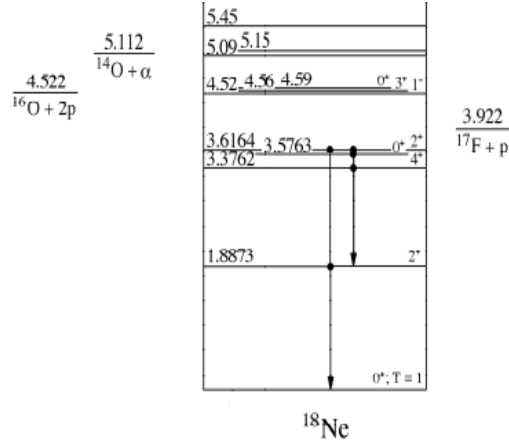


**Figure 1.** The energy level scheme of  $^{18}\text{Ne}$ : We assume that the  $^{18}\text{Ne}$  formed by  $^{17}\text{F}$  ( $d,n$ )  $^{18}\text{Ne}$  reaction populate on  $1^-$  excited state, which is the unbound state due its higher energy than single particle state  $^{17}\text{F}+p$ .

**Table 1. Optical models used in the calculation.**

	$V$	$r_0$	$a_0$	$W_D$	$r_D$	$a_D$	$V_{SO}$
i	98.83	1.05	0.86	32.97	1.43	0.586	7
ii	86.45	1.15	0.81	16.1	1.34	0.68	
iii	56.71	1.17	0.75	12.57	1.26	0.58	6.2
iv	45.04	1.31	0.66	9.15	1.26	0.48	

Since we have not got the data of  $^{17}\text{F}$  ( $d,n$ )  $^{18}\text{Ne}$  reaction yet, we fabricate the “experiment data” based on the simulation result from DWUCK4 using model 1. First, we assume that the partial proton width of  $^{18}\text{Ne}$  is 1 KeV. Then we employ model 1 to the

distorted wave input and keep the transfer wave input fixed. The dashed line in fig. 2a shows the simulation result. The obtained single particle width is 3.0315 KeV. According to formula (5), the spectroscopic factor is 0.3300. According to formula (6), the “experiment data” could be obtained by multiplying the simulation results by the spectroscopic factor, which is represented by solid line in fig. 2a. Now we have got the experiment data. The next step is to switch other models to fit the “experiment data”. Fig. 2b presents the fitting results by using model 2, 3 and 4 as the distorted wave input. Table 2 shows the extracted spectroscopic factors and the values of  $\chi^2$ . Model 2 gives the best fitting because of the lowest  $\chi^2$  value. The DWUCK4 code would calculate the single particle widths at the same time which are also shown in Table 2. To our surprise, the calculated single particle widths using all three different optical models are exactly same. In the former simulations, we keep the transfer wave input fixed. Now we also change the optical models for transfer wave input by modifying the radius for potential and thereby get more combinations. We fit the “experiment data” using the simulation results of all the combinations and extract the spectroscopic factors. Then according to formula (5), the partial proton widths can be obtained by multiplying spectroscopic factors and single particle width. Fig. 3a shows the obtained partial widths. The scattered points with same color and shape have same optical model for distorted wave input and different optical model for transfer wave input. At the very beginning, we assume that the partial width is 1 KeV. If the partial widths obtained by using different optical models are still 1 KeV, we can draw the conclusion that the ambiguities can be counteracted by multiplying

spectroscopic factor and single particle width. It is true for the ambiguities of the optical model for transfer wave input. With fixed distorted wave input, the partial widths obtained from calculations using different optical for transfer wave input are basically identical. Fig. 3b shows the plotting of total cross section versus single particle width. They can be fitted by the direct portion function. Hence, the product of single particle width and the reciprocal of total cross section are constant. Since the total cross section of experiment data is fixed, the total cross section of simulation results are inversely proportional to the corresponding spectroscopic factor. Therefore, the product of the spectroscopic factor and single particle width which is partial proton width keeps constant. We can draw the conclusion that the ambiguities of the optical model for transfer wave input would not impact the partial proton width of  $^{18}\text{Ne}$  in the  $^{17}\text{F}$  (d,n)  $^{18}\text{Ne}$  reaction.

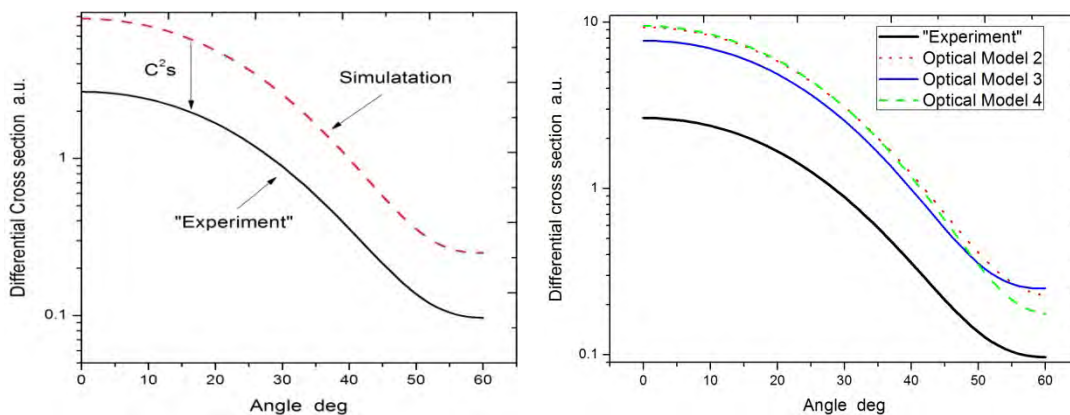


**Figure 2. (a)** The red dashed line is the simulation results using optical model 1. The black solid line is the fabricated “experiment data”. **(b)** The black solid line with larger font is the fabricated “experiment data”. Three colored lines are the simulation results

using three different models for distorted waves. Notice that optical model 3 gives the best fitting to the “experiment data”

**Table 2. The fitting parameters in fig. 2b**

	Optical model 2	Optical model 3	Optical model 4
$C^2S$	<b>0.29011</b>	<b>0.36207</b>	<b>0.30269</b>
$\chi^2$	<b>0.0113</b>	<b>0.0027</b>	<b>0.0293</b>
Single particle width KeV	<b>2.9327</b>	<b>2.9327</b>	<b>2.9327</b>

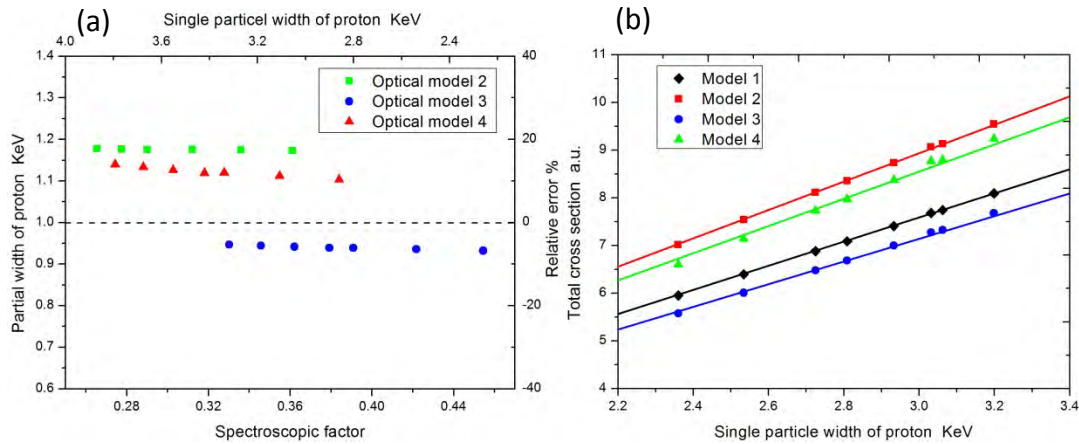


**Figure 3. (a)** The scatted points with same color have same optical model for distorted wave and different models for transfer wave. The dashed line in the middle denotes the assumed partial width of 1 KeV. **(b)** The scatted points with same color have same optical model for distorted wave and different models for transfer wave. The straight lines are the fitting curve with the form of direct portion function. The fitting parameters are shown in Table 3.

**Table 3. The fitting parameters in fig. 3b**

	Optical model 1	Optical model 2	Optical model 3	Optical model 4
Slope	<b>2.53</b>	<b>2.98</b>	<b>2.38</b>	<b>2.85</b>

## Discussion

Fig. 2b shows that the calculated differential cross sections using different optical models are basically same. Fig. 3a shows that the partial widths calculated with different optical models are very close to the assumed value of 1 KeV. All the relative errors are within 20%. The consistency indicates that the universal deuteron and neutron optical models are applicative to the  $^{17}\text{F}(\text{d},\text{n})^{18}\text{Ne}$  reaction.

As discussed above, for stripping reaction the input of transfer wave also impacts the simulation results. For  $^{17}\text{F}(\text{d},\text{n})^{18}\text{Ne}$  reaction, since the single particle width is only determined by single particle state  $^{17}\text{F}+\text{p}$  in  $^{18}\text{Ne}$ . The optical model for transfer wave input would give enough information of the  $^{17}\text{F}+\text{p}$ . The channel of forming  $^{18}\text{Ne}$  does not matter for the calculation of partial width of proton. Therefore, the optical models for distorted wave input would not impact the calculation of single particle width. Only the selection of optical model for transfer wave input would give rise to the variation of single particle width, which explains why we get exactly same value of single particle widths in Table 2.

Fig. 3a shows that the partial width of proton is insensitive to the optical model for transfer wave input. For  $^{17}\text{F}(\text{d},\text{n})^{18}\text{Ne}$  reaction, the optical model for transfer wave is related to  $^{17}\text{F}+\text{p}$  which is hard to verified by fitting experiment due to the rather low probability of proton capture reaction for the proton-rich  $^{17}\text{F}$ . Therefore, it is difficult to select a proper optical model for  $^{17}\text{F}+\text{p}$ . However, our finding shows that if the goal of the

experiment is to obtain the partial proton width of  $^{18}\text{Ne}$ , the ambiguities of optical models for the transfer wave input do not impact the final results.

In conclusion, we simulate the  $^{17}\text{F} (d,n)^{18}\text{Ne}$  reaction by the computer code DWUCK4 based on distorted wave Born approximation (DWBA) method. We try several typical neutron and deuteron optical models for the distorted wave input. All of them give similar partial proton width of  $^{18}\text{Ne}$ , which show the universality of these models. Most importantly, we find the partial width of proton would not be impacted too much by the ambiguities of optical models for transfer wave.

#### 4. Reference

1. Bardayan, D., et al., *Observation of the Astrophysically Important  $3+$  State in  $N 18 e$  via Elastic Scattering of a Radioactive  $F 17$  Beam from  $H 1$* . Physical review letters, 1999. **83**(1): p. 45.
2. Perey, C. and F. Perey, *Compilation of phenomenological optical-model parameters 1954–1975*. Atomic data and nuclear data tables, 1976. **17**(1): p. 1-101.